

AD-A180 450

ARL-TR-86-30

Copy No. 9

MAGNETOHYDRONAMIC UNDERWATER ACOUSTIC TRANSDUCER

Stephen C. Shreppler

APPLIED RESEARCH LABORATORIES
THE UNIVERSITY OF TEXAS AT AUSTIN
POST OFFICE BOX 8029, AUSTIN, TEXAS 78713-8029

1 December 1986

Technical Report

Approved for public release;
distribution unlimited.



Prepared for:

OFFICE OF NAVAL RESEARCH
DEPARTMENT OF THE NAVY
ARLINGTON, VA 22217



UNCLASSIFIED

SECURITY CLASSIFICATION OF THIS PAGE (

REPORT DOCUMENT**AD-A180 450****INSTRUCTIONS
COMPLETING FORM
CATALOG NUMBER****1. REPORT NUMBER****4. TITLE (and Subtitle)****MAGNETOHYDRODYNAMIC UNDERWATER ACOUSTIC
TRANSDUCER****5. TYPE OF REPORT & PERIOD COVERED**
technical report**6. PERFORMING ORG. REPORT NUMBER**
ARL-TR-86-30**7. AUTHOR(s)**

Stephen C. Schreppler

8. CONTRACT OR GRANT NUMBER(s)

N00014-80-C-0490

9. PERFORMING ORGANIZATION NAME AND ADDRESSApplied Research Laboratories
The University of Texas at Austin
Austin, Texas 78713-8029**10. PROGRAM ELEMENT, PROJECT, TASK
AREA & WORK UNIT NUMBERS**

Task 27

11. CONTROLLING OFFICE NAME AND ADDRESSOffice of Naval Research
Department of the Navy
Arlington, VA 22217**12. REPORT DATE**

1 December 1986

13. NUMBER OF PAGES

154

14. MONITORING AGENCY NAME & ADDRESS (if different from Controlling Office)**15. SECURITY CLASS. (of this report)**

UNCLASSIFIED

**15a. DECLASSIFICATION/DOWNGRADING
SCHEDULE****16. DISTRIBUTION STATEMENT (of this Report)**

Approved for public release; distribution unlimited.

17. DISTRIBUTION STATEMENT (of the abstract entered in Block 20, if different from Report)**18. SUPPLEMENTARY NOTES****19. KEY WORDS (Continue on reverse side if necessary and identify by block number)**

magnetohydrodynamic	monopole source	source volume
dipole source	diffusion impedance	electrolyte
underwater transducer	double layer impedance	transmitting sensitivity
thermoacoustic	mutual impedance	efficiency

20. ABSTRACT (Continue on reverse side if necessary and identify by block number)

The magnetohydrodynamic (MHD) and thermoacoustic sound generation mechanisms were investigated analytically and experimentally for a source volume region generated by a time harmonic electric current distribution interacting in a static magnetic field using sodium chloride and water as an electrolyte.

The MHD sound source is the result of the Lorentz force on a conducting medium generated by the interaction of electrical current and a magnetic field. The thermoacoustic source is the result of fluid density changes produced by Joule

DD FORM 1473

1 JAN 73

EDITION OF 1 NOV 65 IS OBSOLETE

UNCLASSIFIED

SECURITY CLASSIFICATION OF THIS PAGE(When Data Entered)

UNCLASSIFIED

SECURITY CLASSIFICATION OF THIS PAGE(When Data Entered)

20. (cont'd)

heating when electrical power is dissipated in a resistive medium. MHD and thermoacoustic source mechanisms were found to produce two distinct acoustic radiation moments: a dipole field and monopole field, respectively.

The source volume region is contained in a rigid walled waveguide where sound from the source volume region radiates into the free medium through apertures at either end of the waveguide. Transmitting sensitivities for both mechanisms were derived analytically for the waveguide geometry and compared to experimental data where good agreement was found in a frequency band of 500 to 4000 Hz. The source directivity for the dipole moment radiation was measured and found to be in good agreement with the classic cosine radiation pattern at low frequencies.

Expressions for the transduction process efficiency and input electrical impedance were also derived and compared to measurements.

Accession For	
NTIS CRA&I	<input checked="checked" type="checkbox"/>
DTIC TAB	<input type="checkbox"/>
Unannounced	<input type="checkbox"/>
Justification	
By	
Distribution/	
Availability Codes	
Dist	Avail and/or Special
A-1	



UNCLASSIFIED

SECURITY CLASSIFICATION OF THIS PAGE(When Data Entered)

TABLE OF CONTENTS

	<u>Page</u>
LIST OF FIGURES	v
LIST OF IMPORTANT SYMBOLS	ix
Chapter 1 INTRODUCTION	1
A. Past Research in the Area of MHD Transduction	3
B. Present Work	4
Chapter 2 THEORY: THE MAGNETOHYDRODYNAMIC- THERMOACOUSTIC WAVE EQUATION	·
A. Ohm's Law for an Electrolyte	7
B. Derivation of the Continuity Equation	9
C. Derivation of the Momentum Equation	15
D. Small Signal Acoustic Approximation	17
E. One-Dimensional Wave Equation	20
F. Dispersion of the Acoustic Field due to the Induced Current Density in a High Conductivity Fluid	20
Chapter 3 THEORY: SOLUTION OF THE WAVE EQUATION FOR THE ACOUSTIC FIELD WITHIN THE WAVEGUIDE	23
A. Boundary Conditions of the Transducer Waveguide	23
B. Justification of the Boundary Conditions	29
C. Acoustic Wavefield due to the Magnetohydrodynamic Source	35
D. Acoustic Wavefield due to the Thermoacoustic Source	47
Chapter 4 THEORY: ELECTROACOUSTIC RELATIONS	53
A. Polarization Impedance of the MHD Waveguide Electrodes	53
B. Electrical Impedance of the MHD Transduction Process	59
C. MHD Transduction Process Power Efficiency	64

	<u>Page</u>
D. MHD Transmitting Current Sensitivity	66
E. Electrical Impedance of the Thermoacoustic Transduction Process	73
F. Thermoacoustic Transduction Process Power Efficiency	78
G. Transmitting Sensitivity of the Thermoacoustic Process	83
Chapter 5 TRANSMITTING EXPERIMENT	87
A. Optimization of the MHD Transmitting Current Sensitivity	87
B. Acoustic Speed Measurement of the Waveguide	94
C. Measurement of the Electrical Impedance of the Transducer	97
D. Transmitting Circuit and Acoustic Signal Measurement System	101
E. Measurement of the MHD Transmitting Sensitivity and Directivity	107
F. Measurement of the Thermoacoustic Transmitting Sensitivity	114
Chapter 6 CONCLUSIONS	119
Appendix A.1 DERIVATION OF THE MAGNETIC DISPERSION RELATION	123
Appendix A.2 THERMOVISCOUS PROCESSES WITHIN THE WAVEGUIDE	126
Appendix B PRESSURE FIELD SPHERICAL HARMONIC FUNCTION EXPANSION, RADIATION IMPEDANCES, AND FARFIELD PRESSURE	130
Appendix C REFLECTION COEFFICIENT EQUATIONS	134
Appendix D COMPUTER PROGRAMS	136
REFERENCES	153

LIST OF FIGURES

<u>Figure</u>		<u>Page</u>
1.1	Dipole Radiation Pattern MHD Transducer	2
2.1	Integral Continuity Equation Control Volume	11
2.2	Integral Momentum Equation Control Volume	16
2.3	MHD Force and Thermoacoustic Volume Expansion Acting in a Spherical Volume	19
3.1	Fluid "Piston" Acoustic Aperture Model	25
3.2	MHD Source Geometry and Coordinate Systems	27
3.3	Self-Impedance of the MHD Waveguide Apertures	30
3.4	Mutual Impedance of the MHD Waveguide Apertures	31
3.5	Ratio of Mutual to Self-Impedance Magnitudes	33
3.6	Ratio of Real Components of the Self- and Mutual Impedance	34
3.7	Delta Function Source Representation for the Plane Wave Green's Function Solution	37
3.8	Magnitude of the Reflection Coefficient	42
3.9	Magnitude of the Modal Particle Velocity and Modal Pressure, 6% NaCl-H ₂ O Solution $\ell_s = 0.10 \text{ m}$, $\ell = 0.10 \text{ m}$, $c_o = 1536 \text{ m/s}$, $R = 0.09 \text{ m}$	44
3.10	Magnitude of the Modal Particle Velocity and Modal Pressure, 6% NaCl-H ₂ O Solution $\ell_s = 0.10 \text{ m}$, $\ell = 0.10 \text{ m}$, $c_o = 650 \text{ m/s}$, $R = 0.09 \text{ m}$	45

<u>Figure</u>		<u>Page</u>
3.11	Magnitude of Modal Particle Velocity and Modal Pressure, 6% NaCl-H ₂ O Solution $\ell_s = 0.05 \text{ m}$, $\ell = 0.10 \text{ m}$, $c_o = 650 \text{ m/s}$, $R = 0.09 \text{ m}$	46
4.1	Equivalent Circuit of the MHD Input Impedance	60
4.2	MHD Mechanism Impedance for 6% NaCl-H ₂ O Solution	63
4.3	MHD Transduction Process Power Efficiency	65
4.4	Transmitting Current Sensitivity Level as a Function of Sound Speed and Frequency	69
4.5	Transmitting Current Sensitivity Level as a Function of Baffle Radius and Frequency	70
4.6	Transmitting Current Sensitivity Level as a Function of Source Length and Frequency	71
4.7	Quadratic Current Transfer Function, Single Frequency Input for 6% NaCl Solution	77
4.8	Quadratic Current Transfer Function, Single Frequency Input for Mercury	79
4.9	Equivalent Circuit of the Combined MHD and Thermoacoustic Input Impedance	80
4.10	Thermoacoustic Transduction Process Efficiency	82
4.11	Quadratic Voltage Transmitting Sensitivity, Single Frequency Input (QVTS)	85
5.1	Magnetohydrodynamic Transducer, Aperture View	88

<u>Figure</u>		<u>Page</u>
5.2	Transmitting Current Sensitivity as a Function of Aperture Radius, for $c_0 = 1550$ m/s, $R = 0.05$ m, $B = 1$ T, $f = 1000$ Hz	90
5.3	Transmitting Current Sensitivity Level (TSCL) as a Function of Aperture Radius and Frequency, for $c_0 = 1550$ m/s, $R = 0.05$ m, $B = 1$ T	91
5.4	Magnetic Induction as a Function of the Transverse Waveguide Dimension, l_z (Field Gap)	93
5.5	Magnetohydrodynamic Transducer Waveguide Construction Details	95
5.6	Measured Magnetic Induction Levels (Gauss) in the MHD Transducer Waveguide	96
5.7	Phase Speed Measurement System	98
5.8	Block Diagram of Transducer Electrical Impedance Measurement System	99
5.9	Measured Input Electrical Impedance of the MHD Transducer Containing a 6% NaCl-H ₂ O Solution	100
5.10	Theoretical and Measured Electrical Input Impedance of the MHD Transducer	102
5.11	Block Diagram of MHD Acoustic Signal Measurement System	104
5.12	MHD Transducer Mounted on the Rotator Column with the H56 Hydrophone	106

<u>Figure</u>		<u>Page</u>
5.13	Constructive Interference of the MHD Pressure Signal on the Waveguide Axis, $\psi = 0^\circ$, at 6900 Hz	108
5.14	Magnetohydrodynamic Transmitting Sensitivity Experiment and Theory, 6% NaCl-H ₂ O Solution, Measurements Made on the Waveguide x Axis, $\psi = 0^\circ$	109
5.15	Magnetohydrodynamic Source Directivity, Farfield Theory and Experiment	111
5.16	Effective Baffle Radii of the MHD Transducer	113
5.17	Second Harmonic Thermoacoustic Pressure Signal	115
5.18	Thermoacoustic Quadratic Voltage Transmitting Sensitivity (QVTS), Theoretical and Experimental Data Comparison	116
A.2.1	Peak Modal Pressure in the MHD Waveguide as a Function of Frequency, Q Determination Plot, 6% NaCl-H ₂ O Solution	129
B.1	Aperture Geometry	131

LIST OF IMPORTANT SYMBOLS

Note that the **bold** symbols imply vector fields.

a, b	x location of the left and right MHD source volume boundaries
A	transducer electrical terminal admittance
\mathbf{B}	magnetic induction vector field
c_{fm}	adiabatic sound speed in the free medium
c_o	adiabatic sound speed in the waveguide
C_d	diffusional capacitance
C_D	electric double layer capacitance
C_p	specific heat at constant pressure
D	diffusion constant, $1.0 \times 10^{-9} \text{ m}^2/\text{s}$
ϵ, ϵ_o	relative permittivity and permittivity of free space, $8.85 \times 10^{-12} \text{ F/m}$
\mathbf{E}	electric intensity vector field
$\mathbf{f} = \mathbf{J} \times \mathbf{B}$	magnetohydrodynamic fluid volume force
F	Faraday constant, 96524 coulomb/mole
$G(x, x_o)$	plane wave Green's function for the waveguide for a Dirac source at x_o
$G_L(x, a), G_R(x, b)$	plane wave Green's function valid in the waveguide to the left and right of the MHD source volume, respectively

$G_{XL}(x,a), G_{XR}(x,b)$	derivatives of the plane wave Green's function with respect to the x coordinate
$h_n^{(1)}$	Hankel function of the first kind of order n
H	Heavyside's unit step function
I	terminal electric current magnitude
j	$\sqrt{-1}$
\mathbf{J}, J_0	current density vector field and the step function amplitude
$k_m = \omega/c_m$	wave number of the free medium
$k = \omega/c_0$	wave number of the medium in the waveguide
$-\ell, \ell$ or $\pm\ell$	notation for indicating the x location of the left and right aperture, respectively
ℓ_y, ℓ_z	the transverse y direction dimension and z direction dimension of the rectangular waveguide
\mathbf{l}	path integration vector
n	number of moles of electrons required per mole of reaction product
N	volumetric concentration, moles/m^3
p	waveguide acoustic pressure field
$p_{\pm\ell m}$	free space pressure field due to the aperture at $-\ell$ or ℓ
P	total pressure $P = P_0 + p$

P_n, P_{n-1}, P_{n+1}	ordinary Legendre polynomial of order $n, n-1, n+1$
P_o	ambient pressure
q	unit electronic charge, 1.602×10^{-19} C
QCTF	quadratic current transfer function of the thermoacoustic source
QVTS	quadratic voltage transmitting sensitivity of the thermoacoustic source
r	free medium radial coordinate
R	ideal gas constant 8.31 joules/(Kelvin mole)
$R_a = \sqrt{l_y l_z / \pi}$	effective aperture radius of the rectangular waveguide
R_d	real component of the diffusion impedance
$R_{\pm l}$	aperture reflection coefficient evaluated at aperture $-l$ or l
R_s	spherical baffle radius
s	unit area normal electrode surface vector
t	time
T	absolute temperature, Kelvin scale
TCS	MHD mechanism transmitting current sensitivity
u	waveguide small signal particle velocity
v	volume

V	terminal potential
W_A	radiated acoustic power
W_e	input electrical power to transducer
x	waveguide longitudinal coordinate
y, z	waveguide transverse coordinates
Z	MHD transducer electrolyte impedance
Z_d	electrical diffusion impedance
Z_m	aperture mutual radiation impedance
Z_p	polarization impedance of the electrodes
Z_s	aperture self-radiation impedance
Z_t	transducer electrical terminal impedance
β	coefficient of thermal expansion, $1/T$
δ	Dirac delta function
ϵ	small x coordinate increment
η	transducer power efficiency
$\Theta = \arcsin(R_a/R_s)$	aperture half angle
$\mu_{\pm l}$	phase of the aperture particle velocities
ν	number of moles of ions required per mole of reaction product

ξ	concentration spatial coordinate, direction normal to electrode surface
ρ	total fluid mass density $\rho = \rho_o + \delta\rho$
$\delta\rho$	acoustic fluid mass density perturbation
ρ_o	waveguide fluid mass density
ρ_{fm}	free medium fluid mass density
σ	ionic fluid conductivity
ϕ	waveguide acoustic potential wavefield
ψ	free medium angular coordinate
ω	angular frequency
Ω	angular frequency, 2ω

CHAPTER 1

INTRODUCTION

The subject matter of this thesis is an investigation of the underwater acoustic transmitting characteristics of a magnetohydrodynamic (MHD) transducer. The transduction mechanism of the MHD transducer is the Lorentz force generated on a conducting fluid conveying electrical charge in the presence of a magnetic field. The transducer consists of a sodium chloride-water solution (electrolyte) contained in a rigid wall rectangular waveguide, 10 cm long and 3.8 cm x 3.2 cm cross section, with acoustic apertures at either end. The waveguide is located between the poles of two large permanent magnets (see Fig 1.1).

A time harmonic electric current density, $\mathbf{J}e^{j\omega t}$, is applied to the electrolyte through electrodes on two facing walls which are parallel to the magnetic field, \mathbf{B} . The current density, which is orthogonal to the magnetic field and the waveguide axis, produces a force on the fluid, $\mathbf{f}=\mathbf{J}\times\mathbf{B}e^{j\omega t}$, in the longitudinal (axis) direction of the waveguide. Assuming the \mathbf{J} and \mathbf{B} fields to be uniform, the time harmonic force generates a plane wave acoustic pressure field within the waveguide which radiates into the free medium via the apertures.

The electromechanical analogy of this transducer is the moving coil transducer where the fluid of the MHD transducer is likened to the coil of the armature. But, unlike the moving coil device which radiates sound by the motion of a surface, the MHD transducer has no radiating surface. The acoustic wave is a result of the direct application of the electromagnetic

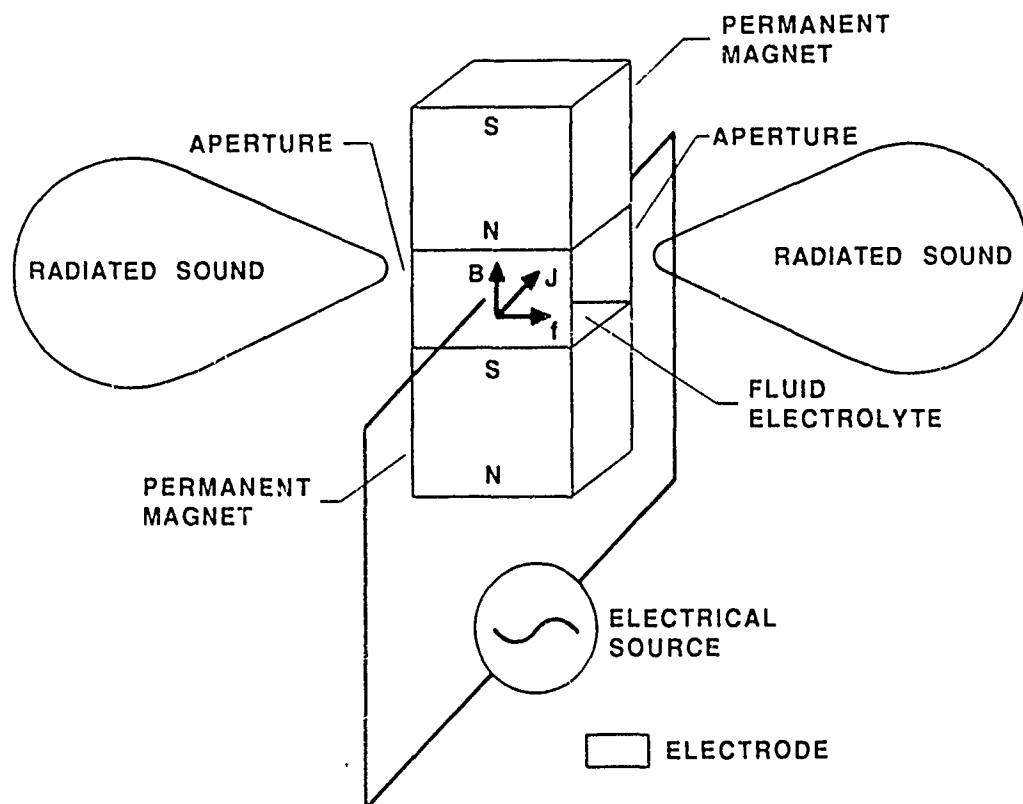


FIGURE 1.1
DIPOLE RADIATION PATTERN MHD TRANSDUCER

ARL:UT
AS-86-518
SCS - GA
9-10-86

energy to the medium (more appropriately, the radiating region of the transducer is termed the MHD source volume).

A. PAST RESEARCH IN THE AREA OF MHD TRANSDUCTION

The first attempts to use the MHD mechanism in fluids for transmitting or receiving acoustic signals are not readily identifiable. Various steady fluid flow rate measuring devices and electromagnetic pumps have been in existence since at least 1945.¹ Acoustic transmitting investigations, in the context that they will be discussed in this thesis, were first carried out by Campanella² in 1955, and later by Ajisaka and Hixson^{3,4} in 1975.

The investigations of Campanella and Ajisaka and Hixson primarily addressed both theoretically and experimentally the generation of plane wave signals by the MHD source radiating in a rigid walled waveguide of semi-infinite length with rigid and pressure release boundaries at the origin. The MHD source region extended from the boundary to a finite distance. Also the infinite length waveguide was investigated by both investigators.

Ajisaka and Hixson³ also considered the finite length waveguide radiating from both apertures into unbounded half spaces. They treated the apertures of the waveguide as pistons on an infinite baffle and derived a pressure transmitting sensitivity expression which is flat over a very broad frequency band. However the sensitivity expression which was derived was for the aperture pressure and not the pressure at the standard 1 m distance.

B. PRESENT WORK

This thesis is a continuation of the work begun by Ajisaka and Hixson, by suggestion of Dr. Elmer Hixson, with the intent to investigate in a more precise manner the radiating characteristics of the MHD source in an infinite free space. Since Ajisaka and Hixson did not experimentally investigate the free medium transmitting characteristics of the MHD source, this was to be a primary task of this investigation.

Chapter 2 of this study is the rigorous derivation of the inhomogeneous pressure wave equation governing the application of the MHD force to a fluid medium. It was realized from considerations of the first law of thermodynamics that when electrical current is passed through a medium of finite conductivity heat is generated. The generation of heat in the medium results in the thermal expansion of the fluid, which creates an additional source of sound. This thermal source mechanism is accounted for in the derivation of the inhomogeneous wave equation. The two source terms of the wave equation are recognized mathematically as being monopole and dipole source distributions, corresponding respectively to the thermal and MHD source mechanisms. The thermal source is shown to be a quadratically nonlinear source in the frequency domain; the spectral nature is discussed in Chapters 2 and 4.

The solution of the wave equation for the acoustic wavefield due to the MHD and thermal sources in the waveguide cannot be found by the

usual convolution of the free space Green's function with the source distribution due to the presence of the waveguide boundaries and magnets. Thus finding the appropriate Green's function for this complicated geometry was not attempted.

In Chapter 3 solutions for the acoustic fields of both source mechanisms are found by separating the acoustic fields into two regions: inside the waveguide and the exterior free medium fields. A plane wave solution for the acoustic field is proposed for the waveguide region assuming impedance boundary conditions at the apertures. To find the exterior acoustic field the waveguide and magnet assembly were assumed to comprise a rigid spherical surface with two radiating apertures. The spherical surface allows for the exterior pressure field to be solved analytically in terms of a Hankel function expansion of a spherical wavefield given the velocity distribution of the apertures. Using the Hankel function expansion of the exterior wavefield, self- and mutual impedance relations were found for the apertures, thus allowing the solution of the interior and therefore the exterior acoustic fields. Geometrical and wave number limitations are placed on the domain of the solutions due to the matching of a plane wavefield within the waveguide to the spherical field on the exterior.

In Chapter 4 derivations of the transmitting electrical impedance, efficiency, and sensitivity expressions are provided. The electrochemistry and the electrical impedance nature of an electrolyte in the vicinity of an electrode surface are discussed, and an equivalent circuit representation of these processes is presented. Included in an appendix is a computer

program which computes the wavefields and transducer characteristics discussed above.

Chapter 5 discusses the design of the transducer used in the experiment and the measurement procedures, and compares the theoretical predictions to experimental data. As will be shown, the analysis is in good agreement with experimental measurements up to frequencies at which differences in assumed and actual transducer geometries become important.

Chapter 6 presents a summary of the research and conclusions which may be drawn.

CHAPTER 2

THEORY: THE MAGNETOHYDRODYNAMIC-THERMOACOUSTIC WAVE EQUATION

In this chapter the small signal, inhomogeneous pressure wave equation governing the acoustic wavefield within a magnetohydrodynamic source volume is derived. The MHD acoustic field is found to have two source mechanisms: (1) the primary mechanism, the magnetohydrodynamic force and (2) a thermal expansion mechanism due to joule heating of the medium by the electric current. The second source is known as a thermoacoustic source.

A. OHM'S LAW FOR AN ELECTROLYTE

In the derivation of the continuity, momentum, and wave equations to be presented in this chapter it is assumed that Ohm's law is valid for the conduction of electrical charge in the electrolyte solution of the MHD transducer. The generalized Ohm's law is stated below under the additional assumption that the ohmic conductivity σ is a constant (not dependent on frequency or space).

$$\mathbf{J} = \sigma (\mathbf{E} + \mathbf{u} \times \mathbf{B}) + e e_0 \mathbf{E}_t \quad (2.1)$$

\mathbf{J} , \mathbf{E} , \mathbf{B} , and \mathbf{u} in Eq. (2.1) are defined as the current density vector field (A/m^2), the electric vector field (V/m), magnetic induction vector field, and the electrolyte fluid particle velocity field. e and e_0 are, respectively, the relative and free space permittivities.

In this thesis it is justifiable to neglect the effects of the induced current ($\sigma \mathbf{u} \times \mathbf{B}$) term and displacement current ($e e_0 \mathbf{E}_t$) term in Eq. (2.1). The

grounds on which these approximations are valid are as follows.

(1) The displacement current term can be rewritten in the form $-j\omega\epsilon_0\mathbf{E}$ for a time harmonic signal $e^{-j\omega t}$. The maximum frequency of interest in this investigation is approximately 15000 Hz, and the relative dielectric permittivity of water is 88. Therefore the coefficient of the displacement current, $\omega\epsilon_0$, could be as great as 7.34×10^{-5} 1/ohm m. The measured value of the ohmic conductivity of a 6% NaCl solution is 5.28 1/ohm m. Therefore, on the basis of the dielectric conductivity being very small relative to the ohmic conductivity, the displacement term is justifiably neglected.

(2) The small signal acoustic approximation will be made in the next section in the derivation of the acoustic wave equation. This implies that the particle velocity u must be much less in magnitude than the adiabatic sound speed c_0 . For the 6% sodium chloride solution investigated in the experiment the value of c_0 is 1550 m/s. The amplitude of the induction field \mathbf{B} considered is of the order of 1 tesla. If the maximum particle velocity is 150 m/s, then the induced current density, $\sigma\mathbf{u} \times \mathbf{B}$, will be 792 A/m². The typical current density used in the experiment is 15000 A/m², so the projected maximum induced current density is only 5% of the typical applied current density. Therefore induced current is justifiably neglected, but as a practical matter the particle velocities generated in the experiment were of the order 10^{-4} m/s so the approximation is very good.

With the above approximations applied to Eq. (2.1), Ohm's law is restated as

$$\mathbf{J} = \sigma\mathbf{E} . \quad (2.2)$$

More will be said concerning the electrolyte conductivity in Chapter 4 in connection with the input impedance of the transducer.

B. DERIVATION OF THE CONTINUITY EQUATION

Temperature rises associated with a time varying electrical current flowing in a resistive fluid produce a monopole acoustic source distribution due to thermal volume expansions of the fluid. The hydrodynamic equations for what is termed in this thesis an ohmic thermoacoustic source have not been derived explicitly in any of the popular literature on acoustics. Didenkulov⁵ treats the problem of current flowing in a cylindrical volume in a fluid but does not state the inhomogenous wave equation and essentially treats the acoustic source volume as a radiating cylindrical surface. Morse and Ingard⁶ treat the subject of a generic heat source but do not address the case of ohmic heating. Westervelt and Larson⁷ discuss optoacoustic laser generated sound in a fluid, which is an electromagnetic heating process at optical frequencies. The derivation to follow accounts for the ohmic thermoacoustic heat source through the continuity equation as an added mass term.

Assuming a constant pressure process, a change in density results from added energy when a fluid is heated. This change in density, $\Delta\rho$, can be related to a small temperature rise ΔT of the medium by the coefficient of thermal expansion β ,

$$\Delta\rho = \beta \rho \Delta T. \quad (2.3)$$

Here ρ is the total fluid mass density.

The derivation of the continuity equation follows from the following statement.

Time rate of change of mass in the control volume	=	Rate of mass flow into the control volume	-	Rate of mass flow out of the control	+	Time rate of change of mass production within the control volume
--	---	---	---	--	---	--

The incremental mass flow rate into a control volume V across its surface S is $-\rho \mathbf{u} \cdot d\mathbf{S}$, the minus sign resulting from the unit normal vector to the surface S pointing away from the control volume (see Fig. 2.1). Net mass flow into and out of the control volume is expressed as the integral of the incremental mass flow rate over the entire closed surface of the control volume.

$$\text{Net mass flow rate into control volume} = - \int_S \rho \mathbf{u} \cdot d\mathbf{S}.$$

The time rate of change of mass in the control volume due to heating is defined as (see Fig. 2.1)

$$\frac{\partial}{\partial t} \int_V \Delta p \, dv = \beta \frac{\partial}{\partial t} \int_V \rho \Delta T \, dv. \quad (2.4)$$

Thus the continuity equation takes the following form:

$$\frac{\partial}{\partial t} \int_V \rho \, dv = - \int_S \rho \mathbf{u} \cdot d\mathbf{S} + \beta \frac{\partial}{\partial t} \int_V \rho \Delta T \, dv. \quad (2.5)$$

Equation (2.5) is valid so long as β is independent of time and temperature. These assumptions imply small temperature changes. (In general β is a

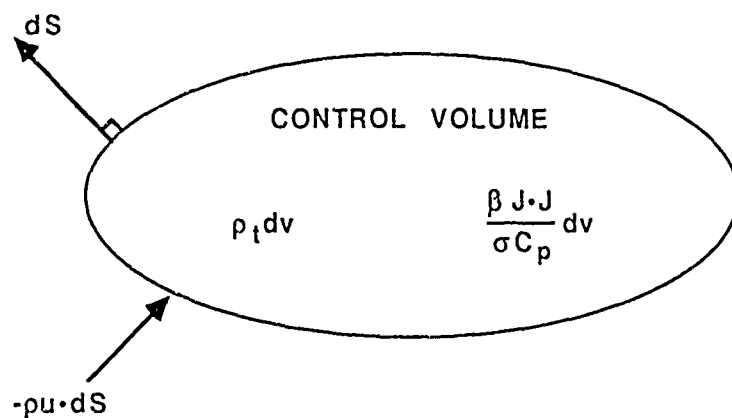


FIGURE 2.1
INTEGRAL CONTINUITY EQUATION CONTROL VOLUME

thermodynamic variable which is dependent on temperature and pressure.)

The temperature change can now be related to the Ohmic heating mechanism by the first law of thermodynamics. If the assumption is made that the heat energy added to the fluid is an isentropic process and occurs at constant pressure then the temperature rise in the fluid can be related to the electromagnetic field energy input by the coefficient of specific heat C_p (joules/(kg K)). On a per unit volume basis the relation is

$$\text{Energy Input}_{\text{emf}} = \int_{T_o}^{T_f} \rho C_p(T) dT . \quad (2.6)$$

For small changes in temperature, $\Delta T/T_o \ll 1$, C_p is approximately constant so Eq. (2.6) can be written as

$$\text{Energy Input}_{\text{emf}} = \rho C_p(T_o) (T_f - T_o) = \rho C_p(T_o) \Delta T . \quad (2.7)$$

From Jackson⁸ the rate of conversion of electromagnetic energy (power) per unit volume into thermal power is given as

$$\text{Power Input}_{\text{emf}} = \mathbf{J} \cdot \mathbf{E} . \quad (2.8)$$

Substituting for \mathbf{E} using Ohm's law, Eq. (2.2), in Eq. (2.8), then taking the time derivative of Eq. (2.7) and equating the result with Eq. (2.8) the relationship between the time rate of change of density and temperature and current density is

$$(\rho \Delta T)_t = \frac{\mathbf{J} \cdot \mathbf{J}}{\sigma C_p} . \quad (2.9)$$

Substituting Eq. (2.9) into Eq. (2.5) results in the integral form of the sonic heating continuity equation,

$$\frac{\partial}{\partial t} \int_V \rho \, dv = - \int_S \rho \mathbf{u} \cdot d\mathbf{S} + \frac{\beta}{\sigma C_p} \int_V \mathbf{J} \cdot \mathbf{J} \, dv. \quad (2.10)$$

The surface integral of Eq. (2.10) can be converted to a volume integral by use of Gauss's divergence theorem. This results in the differential form of the thermoacoustic continuity equation,

$$\rho_t + \nabla \cdot (\rho \mathbf{u}) = \frac{\beta}{\sigma C_p} \mathbf{J} \cdot \mathbf{J}. \quad (2.11)$$

Note that $\mathbf{J} \cdot \mathbf{J}$ in all the preceding equations is a notational form for the real component of the electrical power delivered to the medium since it is the real power which heats the medium and produces thermoacoustic radiation. $\mathbf{J} \cdot \mathbf{J}$ is meant to imply the following operation on \mathbf{J} , assuming a time harmonic dependence of $e^{-j\omega t}$.

$$\mathbf{J}(\mathbf{x}, t) = \text{Re}[\mathbf{J}(\mathbf{x}) e^{-j\omega t}] \equiv (1/2) [\mathbf{J}(\mathbf{x}) e^{-j\omega t} + \mathbf{J}(\mathbf{x})^* e^{j\omega t}] \quad (2.12)$$

Then,

$$\mathbf{J}(\mathbf{x}, t) \cdot \mathbf{J}(\mathbf{x}, t) = (1/4) [\mathbf{J}(\mathbf{x}) e^{-j\omega t} + \mathbf{J}(\mathbf{x})^* e^{j\omega t}] \cdot [\mathbf{J}(\mathbf{x}) e^{-j\omega t} + \mathbf{J}(\mathbf{x})^* e^{j\omega t}] \quad (2.13)$$

or,

$$\mathbf{J}(\mathbf{x}, t) \cdot \mathbf{J}(\mathbf{x}, t) = (1/2) \text{Re}[\mathbf{J}(\mathbf{x})^* \cdot \mathbf{J}(\mathbf{x}) + \mathbf{J}(\mathbf{x}) \cdot \mathbf{J}(\mathbf{x}) e^{-j2\omega t}]. \quad (2.14)$$

Equation (2.14) implies that the power dissipated in the medium has a time independent component plus an oscillating component. This corresponds to the average power plus the time harmonic fluctuation. For a

real valued source volume function ($\mathbf{J}(\mathbf{x})$ real) Eq. (2.14) reduces to

$$\mathbf{J}(\mathbf{x},t) \cdot \mathbf{J}(\mathbf{x},t) = (1/2) J^2(\mathbf{x}) \operatorname{Re}[1 + e^{-j2\omega t}] . \quad (2.15)$$

For the Cartesian system,

$$J^2(\mathbf{x}) \equiv J_x^2(\mathbf{x}) + J_y^2(\mathbf{x}) + J_z^2(\mathbf{x}) . \quad (2.16)$$

The physical implication of the constant term in Eq. (2.15) is that the power flow into the medium is always positive. Since the power input is related to p_t by the continuity equation, Eq. (2.11), the waves produced by ohmic heating will be compressional. Intuitively this is a reasonable result since the derivation assumed an isentropic process, which implies that the heat added to the medium is not dissipated but raises the temperature of the medium, and therefore causes a continuous thermal expansion of the medium.

Integrating Eq. (2.9) over a pulse time period, τ , the constraint on energy transport into the fluid such that the small temperature rise assumption is valid is

$$\frac{\Delta T}{T_0} = \frac{1}{\sigma \rho C_p T_0} \int_0^\tau \mathbf{J} \cdot \mathbf{J} \, dt \ll 1 . \quad (2.17)$$

The temperature change constraint of Eq. (2.17) can be evaluated using Eq. (2.15) if the change in density is assumed small. For an integer number of current cycles the constraint relation for the current density pulse length time, τ , becomes

$$J_o^2 \tau \ll 2 \sigma C_p T_o \rho_o . \quad (2.18)$$

The units of $J_o^2 \tau$ are joules/meter³ which is the volumetric internal energy density change of the electrolyte by the applied current density J_o applied by a sinusoidal signal for a period τ . The right side of Eq. (2.18) is computed to be, for a 5% NaCl-water solution at 20°C, 2.5×10^6 joules/meter³ or 2.5 joules/cm³. During experimental investigation, described in Chapter 5, the pulse time was 5 ms; therefore the constraint on the current density was $J_o \ll 1.62 \times 10^6$ A/m²; the experimental value was 15000 A/m².

C. DERIVATION OF THE MOMENTUM EQUATION

The momentum conservation law is basically a statement of Newton's second law:

$$\begin{array}{ccccc} \text{time rate of change of} & & \text{net momentum influx} & & \text{sum of the forces} \\ \text{momentum inside the} & \Rightarrow & \text{across the control} & + & \text{acting on the} \\ \text{control volume} & & \text{volume surfaces} & & \text{control volume} \end{array}$$

The integral form of the three-dimensional magnetohydrodynamic momentum equation follows directly from the verbal statement (see Fig. 2.2).

$$\frac{\partial}{\partial t} \int_V \rho \mathbf{u} dv = - \int_S (\rho \mathbf{u}) \mathbf{u} \cdot d\mathbf{S} - \int_S P d\mathbf{s} + \int_V \mathbf{J} \times \mathbf{B} dv . \quad (2.19)$$

Gauss's divergence theorem is once again applied to the surface integral and the differential form of Eq. (2.19) follows,¹⁰

$$\underline{\rho_t \mathbf{u}} + \rho \mathbf{u}_t + \underline{\nabla \cdot (\rho \mathbf{u}) \mathbf{u}} + (\rho \mathbf{u} \cdot \nabla) \mathbf{u} + \nabla P = \mathbf{J} \times \mathbf{B} . \quad (2.20)$$

The underlined terms of Eq. (2.20) are replaced using the continuity equation, Eq. (2.11). The result is the magnetohydrodynamic-thermoacoustic

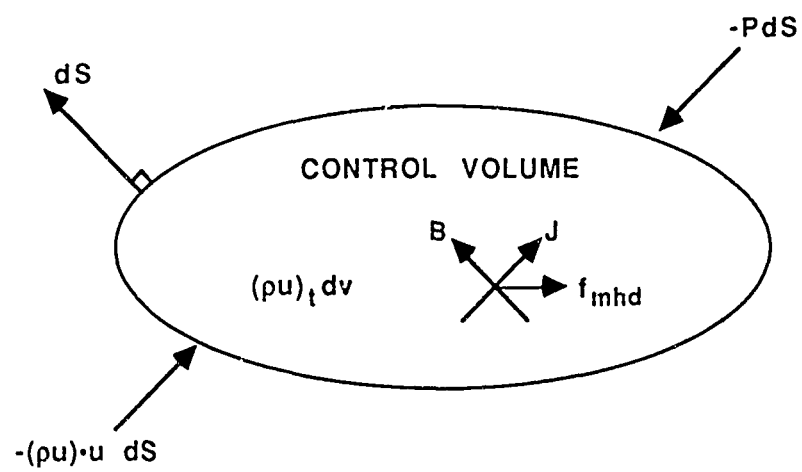


FIGURE 2.2
INTEGRAL MOMENTUM EQUATION CONTROL VOLUME

momentum equation,

$$\rho \mathbf{u}_t + (\rho \mathbf{u} \cdot \nabla) \mathbf{u} + \nabla P = \frac{-\beta}{\sigma C_p} (\mathbf{J} \cdot \mathbf{J}) \mathbf{u} + \mathbf{J} \times \mathbf{B} . \quad (2.21)$$

Morse and Ingard¹¹ discuss the existence of electromagnetic forces on a fluid but do not derive an explicit expression for the Lorentz force in connection with the momentum equation.

D. SMALL SIGNAL ACOUSTIC APPROXIMATION

The small signal acoustic approximation (Mach number $\ll 1$) is made in the wave equation and boundary condition derivations. The small signal acoustic perturbation variables of first order magnitude are the perturbed pressure and density,

$$p = P - P_o , \quad (2.22a)$$

and

$$\delta \rho = \rho - \rho_o , \quad (2.22b)$$

where P_o and ρ_o are the quiescent pressure and density respectively. The small signal approximation constrains the perturbation variables to the following limits,⁷

$$|p| \ll \rho_o c_o^2 , \quad (2.23a)$$

and,

$$|\delta \rho| \ll \rho_o . \quad (2.23b)$$

The equation of state is given as

$$c_o^2 = \left. \frac{\partial P}{\partial \rho} \right|_{\varepsilon = \text{constant}, P = P_o, \rho = \rho_o} \quad (2.23c)$$

where c_o is the isentropic sound speed, defined as a constant for the fluid at

constant entropy, ϵ , and for small perturbations in total pressure P and total fluid density ρ about the ambient values.

The linearized small signal equation of state can be stated in terms of the perturbation variables as

$$p = c_o^2 \delta \rho . \quad (2.24)$$

Linearized small signal versions of Eqs. (2.12) and (2.20) are, respectively,

$$\delta \rho_t + \rho_o \nabla \cdot \mathbf{u} = \frac{\beta}{\sigma C_p} (\mathbf{J} \cdot \mathbf{J}) \quad (2.25)$$

and

$$\rho_o \mathbf{u}_t + \nabla p = \mathbf{J} \times \mathbf{B} . \quad (2.26)$$

Performing the usual mathematical operations on Eqs. (2.24), (2.25), and (2.26) the MHD-thermoacoustic wave equation results,

$$\nabla^2 p - \frac{1}{c_o^2} p_{tt} = \frac{-\beta}{\sigma C_p} (\mathbf{J} \cdot \mathbf{J})_t + \nabla \cdot (\mathbf{J} \times \mathbf{B}) , \quad (2.27)$$

where the inhomogeneous source terms are the thermoacoustic source and the MHD source, respectively. Pierce identifies the first source term as a monopole source distribution function and the second source term as a dipole source distribution function where $\mathbf{J} \times \mathbf{B}$ is the dipole moment vector.¹²

The simplest control volume to view the qualitative nature of the two sources is that of a sphere, such as shown in Fig. 2.3. Thermal expansion of the control volume due to a uniform current density flowing across the volume will generate a uniform spherical wave. The MHD force

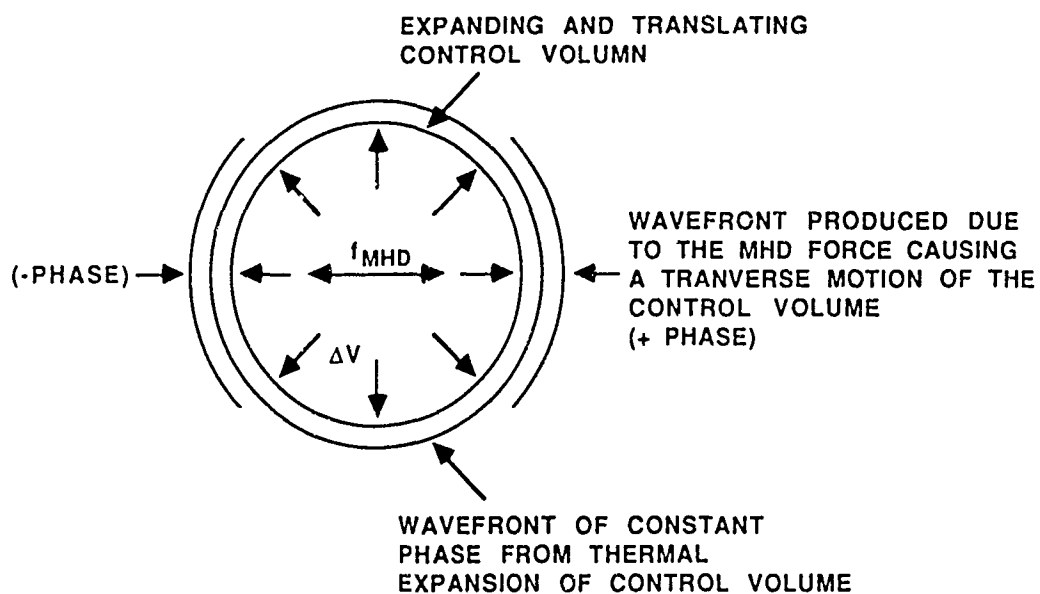


FIGURE 2.3
MHD FORCE AND THERMOACOUSTIC VOLUME EXPANSION
ACTING IN A SPHERICAL VOLUME

ARL:UT
 AS-86-422
 SCS - GA
 8 - 6 - 86

causes a translational oscillation of the control volume in the direction of the dipole moment, creating a dipole wavefield.

E. ONE-DIMENSIONAL WAVE EQUATION

In the one-dimensional development for the Cartesian system the vector field $\mathbf{J} \times \mathbf{B}$ is in the x axis direction. The bold face notation is thus suppressed below and the cross-product implies $\mathbf{J} \cdot \mathbf{B} \sin\Theta$, where Θ is the angle between the vector fields in the y-z plane.

$$p_{xx} - \frac{1}{c_o^2} p_{tt} = \frac{-\beta}{\sigma C_p} (\mathbf{J} \cdot \mathbf{J})_t + (\mathbf{J} \times \mathbf{B})_x. \quad (2.28)$$

The one-dimensional wave equation is the basis for the plane wave field assumed in the MHD transducer waveguide. Chapter 3 is devoted to the derivation of the boundary conditions and solution of the waveguide field.

F. DISPERSION OF THE ACOUSTIC FIELD DUE TO THE INDUCED CURRENT DENSITY IN A HIGH CONDUCTIVITY FLUID

In the above derivation of the wave equation, induced currents were ignored. When one considers a high conductivity fluid, such as mercury, which has a conductivity on the order of 10^6 1/ohm m such an assumption must be carefully examined. As in the NaCl-water case, the displacement term can be neglected, and Ohm's law can be written as

$$\mathbf{J} = \sigma (\mathbf{E} + \mathbf{u} \times \mathbf{B}). \quad (2.29)$$

However, the induced current density term cannot be eliminated. If again we assume that the current density, \mathbf{J} , is 15000 A/m² and the particle velocity is

150 m/s, E is then found to be 150.5 V/m for the mercury medium. The induced electric field, uXB , is 150 V/m for a magnetic field of 1 T. Therefore the induced term should not in general be neglected in the derivation of the acoustic wave equation.

When Eq. (2.29) is substituted into the inhomogeneous terms of the wave equation, Eq. (2.27), a frequency dependent dispersion relationship arises which depends on the magnetic field and fluid conductivity. The dispersion relation is derived in Appendix A.1 for plane waves propagating in a conducting medium in a direction normal to an applied static magnetic field. The dispersion relation is stated below.

$$k = \left(\left(\frac{\omega}{c_0} \right)^2 - \frac{j \omega \sigma B_0^2}{\rho_0 c_0^2} \right)^{1/2} \quad (2.30)$$

Physically the effect of the magnetic field is to dampen or attenuate the wave by converting the kinetic energy of the wave to electrical energy which is then dissipated by the resistivity of the medium. From Eq. (2.30) it can be seen that the dispersion effects of the magnetic field can be neglected when

$$\frac{\sigma B^2}{\omega \rho_0} \ll 1 \quad (2.31)$$

Consider the 6% NaCl-water solution used in the experiment, assuming a conductivity of 5.28 mho/m and a magnetic field of 1 T. The dispersion is negligible for frequencies much greater than 0.0007 Hz. Neglecting dispersion in NaCl-water solutions is thus justifiable. However, for mercury which has a conductivity of $\sim 10^6$ mho/m, the frequency must be

much greater than 74 Hz before dispersion may be neglected.

The significance of the dispersion relation arises in the derivation of the transducer impedance (Chapter 4), in that it indicates whether the induced electric field, and thus the acoustic coupling contribution to the impedance, will be important.

CHAPTER 3

THEORY: SOLUTION OF THE WAVE EQUATION FOR THE ACOUSTIC FIELD WITHIN THE WAVEGUIDE

The solution of Eq. (2.28) for the pressure wavefield excited in the waveguide by the magnetohydrodynamic and thermoacoustic sources is found by solving the two point boundary value problem for this equation and the related boundary conditions at the apertures.

The inhomogeneous terms are assumed to have a time harmonic dependence of the form

$$(J \times B)_x = (J(x) \times B)_x e^{-j\omega t} \quad (3.1)$$

and

$$\frac{-\beta (J \cdot J)_t}{\sigma C_p} = \frac{j \omega \beta J^2(x)}{\sigma C_p} e^{-j2\omega t} . \quad (3.2)$$

Notice that the thermoacoustic source responds at twice the drive frequency, ω , and is therefore twice the MHD source frequency.

Due to the linearity of the wave equation, Eq. (2.33), the solution of the wavefield can be found by considering the two source mechanisms independently. The acoustic fields due to the sources can then be added to find the total field.

A. BOUNDARY CONDITIONS OF THE TRANSDUCER WAVEGUIDE

The boundary conditions of the waveguide are a core problem of this thesis. By specifying the boundary conditions, the form of the field

solution is specified and thus the transduction nature of the waveguide system is determined. Hence it is essential that the boundary conditions of the waveguide be accurately stated.

The apertures of the waveguide are assumed to be radiating into an acoustic free medium. Since the power transmitted by the apertures radiates into the entire medium it is evident that some of the power radiated by one aperture will illuminate the other. Thus there is coupling of acoustic power between the waveguide apertures. The specification of the boundary conditions must therefore take the radiation coupling into account. The aperture acoustic radiation coupling is described by the mutual acoustic radiation impedance.

The acoustic pressure in the waveguide at an aperture is assumed to be related to the aperture particle velocities by attributing a self- and mutual radiation impedance to the aperture. In order to describe the aperture as an impedance boundary the aperture is modeled acoustically as a fluid "piston layer", to which an acoustic radiation impedance can be attributed. The piston layer is assumed to transmit only the acoustic particle velocity.

Two pressures are present on the free medium radiating surface of the piston. one pressure is due to the impedance Z_s of the free medium as seen by the piston (i.e., the inertia and radiation properties of the "piston") and the second is the pressure represented by the mutual radiation. See Fig. 3.1 for a qualitative view of the aperture piston layer forces.

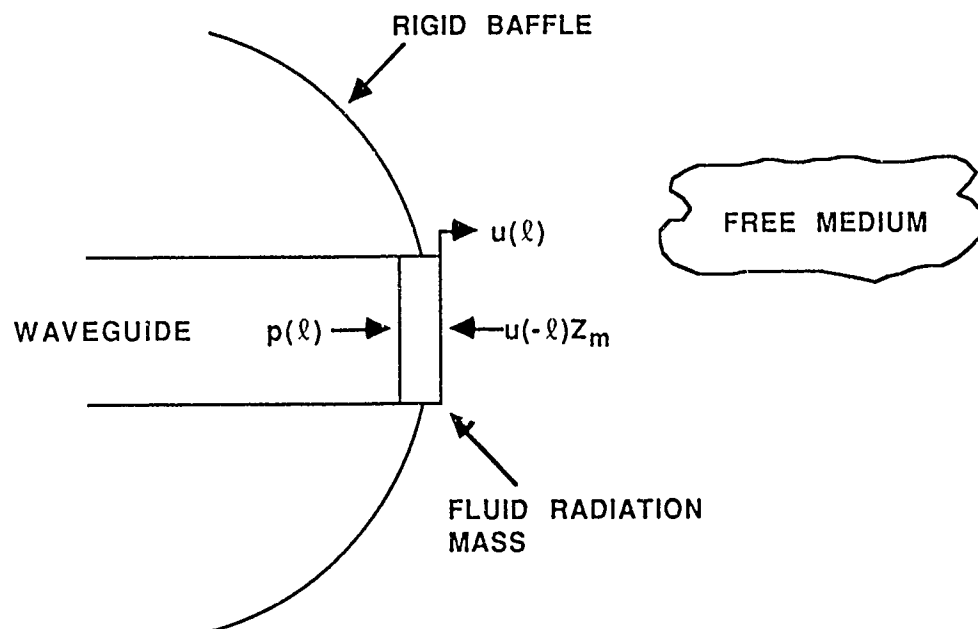


FIGURE 3.1
FLUID "PISTON" ACOUSTIC APERTURE MODEL

Given the model described above the boundary conditions can be symbolically stated as follows.

$$\text{and} \quad p(\ell) = u(\ell) Z_s - u(-\ell) Z_m \quad (3.3a)$$

$$p(-\ell) = -u(-\ell) Z_s + u(\ell) Z_m, \quad (3.3b)$$

where the self-impedance, Z_s , is defined as the ratio of the free medium piston surface pressure $p_{\pm \ell fm}$ to the aperture particle velocity $u(\pm \ell)$ in the absence of the radiation at the second aperture. The mutual radiation impedance, Z_m , between apertures is defined as the ratio of the pressure caused at one aperture due to the particle velocity at the other aperture. The minus signs appearing with $u(-\ell)$ arise from the convention of defining a positive velocity as being outwardly directed from the surface of the sphere. Relative to the origin in the center of the duct a positive velocity at the $-\ell$ end is negative (see Fig. 3.2).

An analytical solution for the free medium pressure field as a function of aperture velocity is possible if the apertures are represented as uniformly vibrating circular pistons on a rigid spherical baffle as shown in Fig. 3.1. Note that if the apertures are not circular an equivalent area circular piston may be defined and the circular piston analysis used provided the wavelength is not small relative to the equivalent circle radius, or when the product of the free medium wave number and the aperture radius is much less than one ($kR_a \ll 1$).

There is an analytical solution for free medium acoustic field generated by circular pistons on a rigid spherical baffle in terms of the

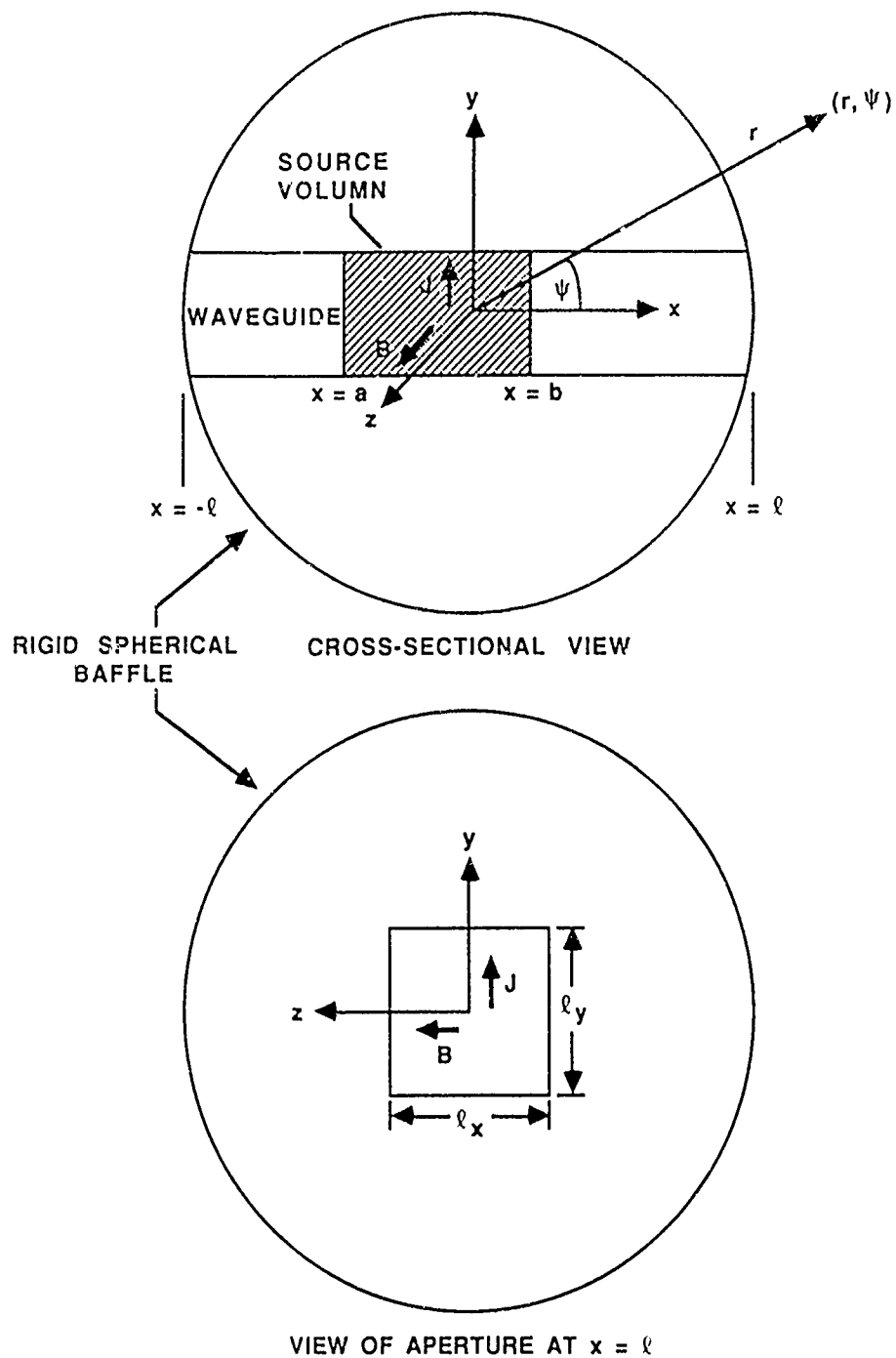


FIGURE 3.2
MHD SOURCE GEOMETRY AND COORDINATE SYSTEMS

spherical harmonic function expansion. Sherman^{13,14} has derived analytical results for the self- and mutual radiation impedances of an arbitrary number of circular sources with arbitrary locations on a spherical baffle using the spherical harmonic function expansion. His results are specialized here to the case of two sources (apertures) located 180° apart.

Two items should be mentioned at this point concerning the use of the spherical harmonic expansion as a boundary condition. (1) the expansion is in terms of spherical waves, e^{jkr}/r , and the conditions at the aperture are in terms of plane waves, e^{jkx} . The assumption concerning the matching of the fields is that the radius of curvature of the surface of the aperture (radius of the spherical baffle, R_s) is great compared to the radius of the aperture, i.e., that the aperture piston layer surface motion is approximately planar, and not radial. (2) The pressure at an aperture due to the mutual radiation is calculated as an average pressure of the spherical waves over the aperture surface area. The implication of (1) and (2) is that the model is valid for $R_a/R_s \ll 1$ and $kR_a \ll 1$.

The self-impedance, Z_s , and the mutual impedance, Z_m , which are in terms of the spherical harmonic function expansion of the free medium pressure field, $p_{\pm lfm}$, are defined as

$$Z_s(\pm l) = \frac{\int_{S(\pm l)} p_{\pm lfm}(r, \psi) dS}{u(\pm l) \int_{S(\pm l)} dS} \quad (3.4a)$$

$$Z_m(\pm \ell) = \frac{\int_{S(\pm \ell)} p_{\pm \ell fm}(r, \psi) dS}{u(\pm \ell) \int_{S(\pm \ell)} dS} \quad (3.4b)$$

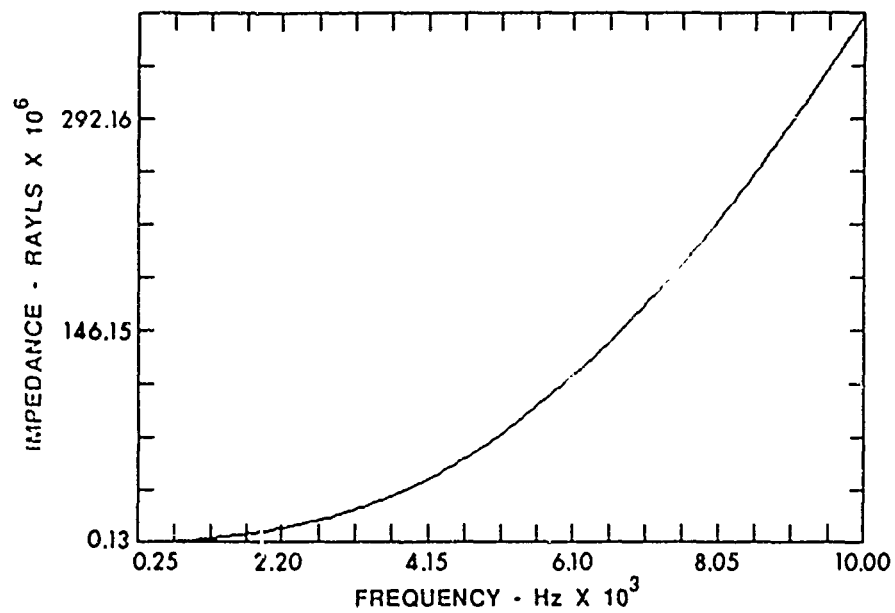
with similar definitions for the aperture at $-\ell$.

The free medium pressure $p_{\ell fm}(r, \psi)$ is a function of $u(\ell)$, $u(-\ell)$, spherical baffle radius R_s , aperture radius R_a , and the free medium acoustic impedance. Due to the symmetry of the sources the pressure is spatially a function of one angle, ψ , and the range, r . The source geometry is shown in Fig. 3.2. See Appendix B for the functional form of $p_{\ell fm}$.

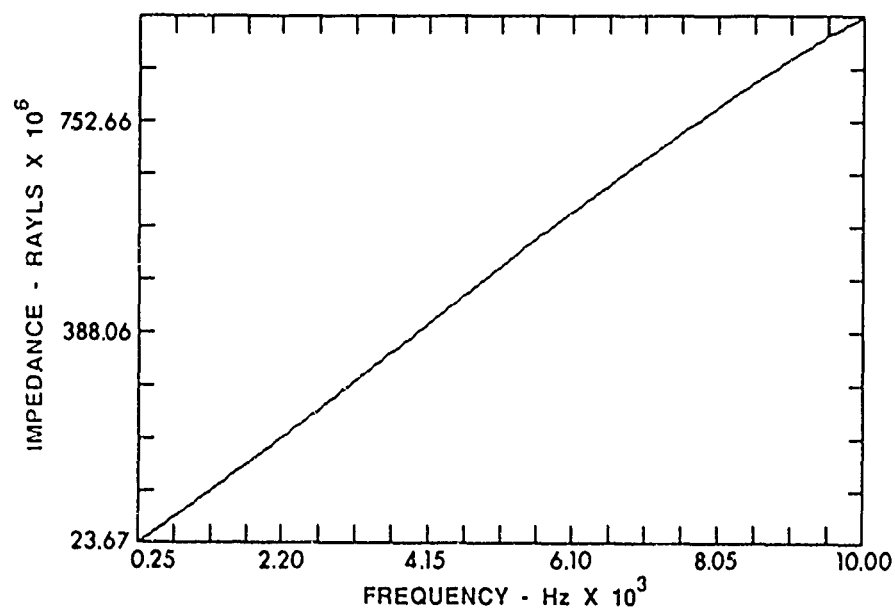
B. JUSTIFICATIONS OF THE BOUNDARY CONDITIONS

Before going on to the solution of the wavefield it is necessary to show that the mutual radiation pressure is a significant factor. An experimental investigation was carried out with a transducer having an effective spherical baffle radius of 0.05 m and an aperture radius of 0.0210 m. The actual apertures were square. The fluid medium in the waveguide was a 6% NaCl-water solution with $\rho_o = 1041 \text{ kg/m}^3$ and $c_o = 1600 \text{ m/s}$. The free medium was fresh water.

The self- and mutual impedances were computed numerically by the computer routine MISF, using Sherman's results, and the real and imaginary components graphed as a function of frequency in Figs. 3.3(a), (b) and 3.4(a), (b), respectively. The use of these impedances as boundary conditions for the above geometric dimensions is valid for frequencies less



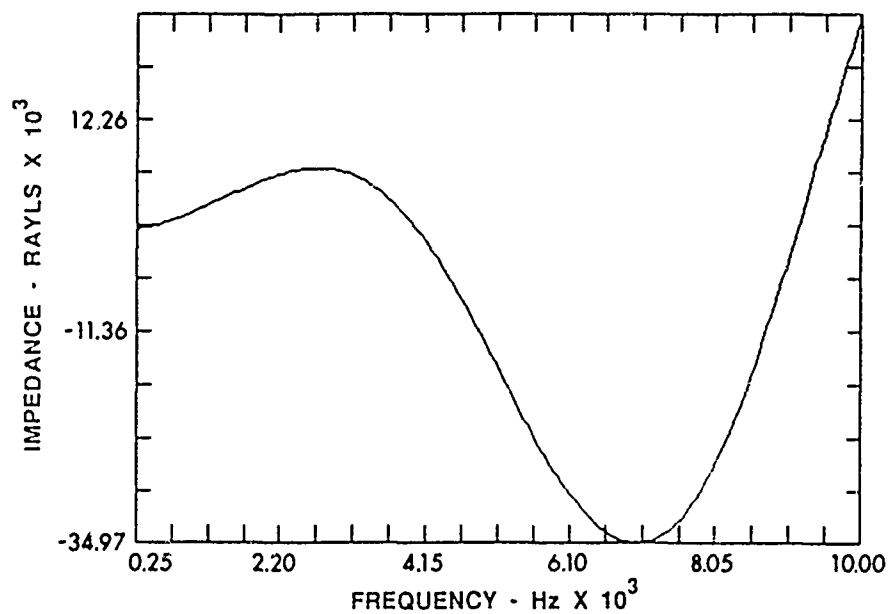
(a)
REAL SELF-IMPEDANCE



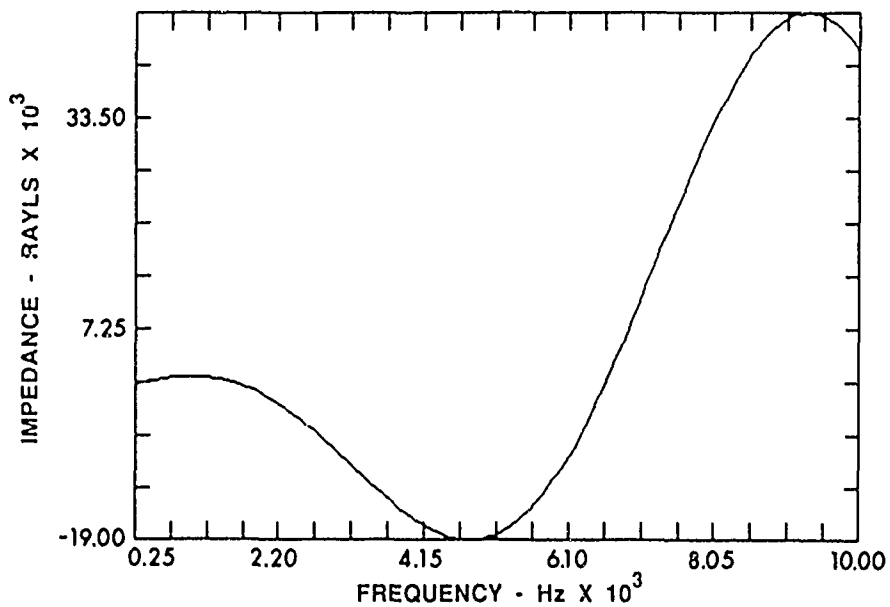
(b)
IMAGINARY SELF-IMPEDANCE

FIGURE 3.3
SELF-IMPEDANCE OF THE MHD WAVEGUIDE APERTURES
 $\ell = 0.10$ m, $\ell_s = 0.10$ m, $c_0 \approx 1550$ m/s, $R = 0.05$ m, $R_a = 0.02$ m

ARL:UT
AS-86-425
SCS - GA
8-6-86



(a)
REAL MUTUAL IMPEDANCE



(b)
IMAGINARY MUTUAL IMPEDANCE

FIGURE 3.4
MUTUAL IMPEDANCE OF THE MHD WAVEGUIDE APERTURES
 $\ell = 0.10$ m, $\ell_s = 0.10$ m, $c_0 = 1550$ m/s, $R = 0.05$ m, $R_a = 0.02$ m

ARL:UT
AS-86-426
SCS-GA
8-6-86

than 10,000 Hz.

The mutual impedance components (Fig. 3.4) display a characteristic oscillation which arises from constructive and destructive interference as the pressure wave length varies relative to the circumferential distance between apertures. For example, the first peak in the mutual impedance should be expected at the frequency at which a quarter wavelength is equal to half the sphere circumference; for $c_o = 1500$ m/s this occurs at approximately 2390 Hz. In Fig. 3.4 the first peak of the imaginary component is at 2700 Hz.

To show that the inclusion of the mutual impedance is important it is necessary to compare the magnitude of the mutual impedance components to the self-impedance components. Intuitively one would expect the mutual impedance to be most significant at low frequencies where the Rayleigh distances of the sources are very short and therefore radiation is omnidirectional. This observation explains the dropoff at high frequencies of the envelope of the mutual impedance plots.

Figure 3.5 shows the ratio of mutual to self-impedance magnitudes. The peak of this plot occurs at approximately 7500 Hz for the geometry described above, with a ratio of 0.05. One might conclude that the mutual impedance is small, however the radiation of sound is dependent on the real component of the acoustic self-impedance. Hence it is more relevant to consider a ratio of the real impedance parts. Figure 3.6 shows this ratio, assuming that the particle velocities of the duct are 180° out of phase and are of equal amplitude (first mode of the waveguide with a source

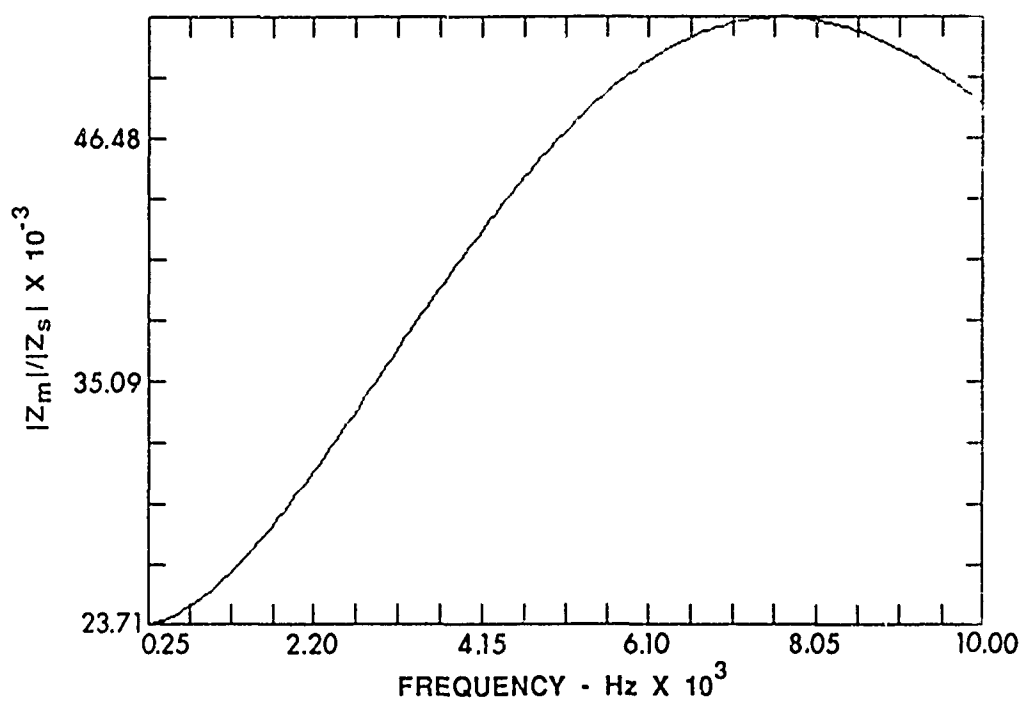


FIGURE 3.5
 RATIO OF MUTUAL TO SELF-IMPEDANCE MAGNITUDES
 $\ell = 0.10$ m, $\ell_s = 0.10$ m, $c_0 = 1550$ m/s, $R = 0.05$ m, $R_a = 0.02$ m

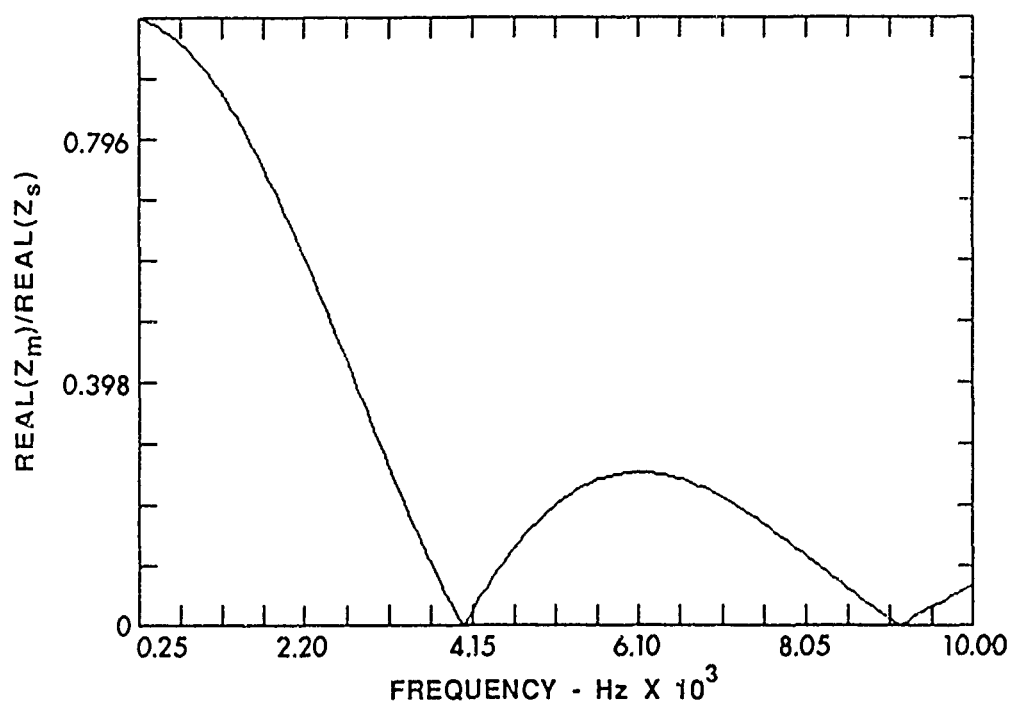


FIGURE 3.6
 RATIO OF REAL COMPONENTS OF THE SELF-
 AND MUTUAL IMPEDANCE
 $\ell = 0.10$ m, $\ell_s = 0.10$ m, $c_0 = 1550$ m/s, $R = 0.05$ m, $R_a = 0.02$ m

distribution symmetric about the x origin). Note that the ratio at 250 Hz is nearly one. Thus at low frequencies the real component of the mutual impedance is an important effect. The real component will have the effect of altering the amplitude of the resonance characteristics of the wavefield in the waveguide, and to a much lesser extent the imaginary component will modify the periodicity of the resonance response spectrum.

C. ACOUSTIC WAVEFIELD DUE TO THE MAGNETOHYDRODYNAMIC SOURCE

The Fourier transform with respect to time of the inhomogeneous pressure wave equation for the MHD source is given by

$$p_{xx} + k^2 p = (J(X) \times B)_x, \quad (3.5)$$

where $k = \omega/c_0$ is the wave number. The inhomogeneous wave equation with inhomogeneous boundary conditions, Eqs. (3.3a) and (3.3b), are in terms of two acoustic field variables p and u . To make the solution process more convenient a change of variables from pressure and particle velocity to velocity potential, ϕ , is made as follows.

$$u = \phi_x \quad (3.6a)$$

and

$$p = -\rho_0 \phi_t = i\omega\rho_0 \phi. \quad (3.6b)$$

Substitution of the above transform pair into Eqs. (3.5), (3.3a), and (3.3b) yields the two-point boundary value problem for the wavefield in the waveguide in terms of one dependent variable, ϕ . The inhomogeneous wave equation, Eq. (3.5), becomes

$$\phi_{xx} + k^2 \phi = \frac{-j}{\omega \rho_0} (J \times B)_x, \quad (3.7a)$$

subject to the boundary conditions,

$$-j \omega \rho_0 \phi(\ell) + \phi_x(\ell) Z_s - \phi_x(-\ell) Z_m = 0 \quad (3.7b)$$

and

$$-j \omega \rho_0 \phi(-\ell) - \phi_x(-\ell) Z_s + \phi_x(\ell) Z_m = 0. \quad (3.7c)$$

The solution of Eqs. (3.7) may be achieved by use of a Green's function. This approach was chosen because the Green's function is easy to determine and the solution lends itself to convenient numerical computation for arbitrary source functions. The inhomogeneous Green's wave equation for the above problem is

$$G_{xx}(x, x_0) + k^2 G(x, x_0) = -\delta(x - x_0), \quad (3.8)$$

where $G(x, x_0)$ is the Green's function for the wavefield as a function of x due to a Dirac delta function distributed source at x_0 . Shown in Fig. 3.7 is the delta function source relative to the coordinate frame and other geometric lengths.

A traveling plane wave solution in the following form is proposed.

$$G(x, x_0) = \begin{cases} A (e^{-jkx} + R_{-\ell} e^{jkx}) & -\ell < x < x_0 < \ell, \\ B (e^{jkx} + R_{\ell} e^{-jkx}) & -\ell < x_0 < x < \ell, \end{cases} \quad (3.9a)$$

$$(3.9b)$$

where $R_{-\ell}$ and R_{ℓ} are the reflection coefficients at the apertures.

The proposed solution represents plane waves propagating to the left, e^{jkx} , and to the right, e^{-jkx} . Equation (3.9a) is the wavefield to the left of the source discontinuity at x_0 , where the left traveling wave, e^{-jkx} , is incident on the $-\ell$ aperture and $R_{-\ell} e^{jkx}$ represents the reflected right

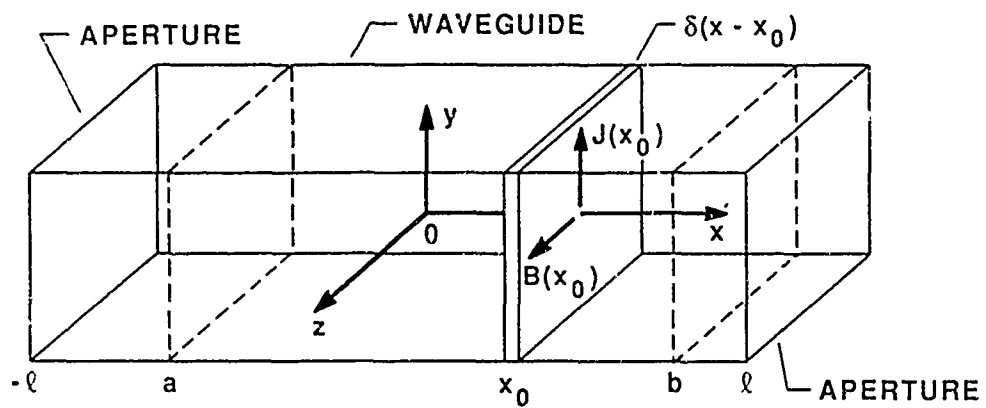


FIGURE 3.7
DELTA FUNCTION SOURCE REPRESENTATION
FOR THE PLANE WAVE GREEN'S FUNCTION SOLUTION

traveling wave. Equation (3.9b) is the wavefield to the right of the source, including a right traveling wave and a left traveling reflected wave. In general R is a complex quantity representing the phase shift and attenuation of the wave upon reflection from the aperture.

Equations (3.9a,b) must be compatible with the conditions at the source where the values of the two solutions must be equal (continuous) and the first derivatives must satisfy the slope discontinuity. The continuity condition is stated as follows.

$$G(x=x_0, x_0) \text{ for } -l < x < x_0 < l = G(x=x_0, x_0) \text{ for } -l < x_0 < x < l \quad (3.10)$$

The discontinuity condition is found by integrating Eq. (3.8) with respect to x and taking the limit as the integration bounds converge to the source at x_0 . This yields

$$\lim_{\epsilon \rightarrow 0} \{ G_x(x_0 + \epsilon, x_0) - G_x(x_0 - \epsilon, x_0) \} = -1. \quad (3.11)$$

The result of applying the source conditions stated in Eqs. (3.10) and (3.11) to the general solution, Eqs. (3.9a,b), is the Green's function for the waveguide field,

$$G(x, x_0) = \begin{cases} \frac{j (e^{jkx_0} + R_{-1} e^{-jkx_0}) (e^{-jkx} + R_{-1} e^{jkx})}{2k(1 - R_{-1} R_{-1})} & -l < x < x_0 < l, \quad (3.12a) \\ \frac{j (e^{-jkx_0} + R_{-1} e^{jkx_0}) (e^{jkx} + R_{-1} e^{-jkx})}{2k(1 - R_{-1} R_{-1})} & -l < x_0 < x < l. \quad (3.12b) \end{cases}$$

The solution of the wavefield in terms of the velocity potential can therefore

be stated in integral form as¹

$$\phi(x) = \frac{-j}{\omega \rho_o} \int_{-\ell}^{\ell} (J \times B)_x G(x, x_o) dx_o. \quad (3.13)$$

For any frequency ω , Eq. (3.13) can always be evaluated numerically because the reflection coefficients are constant multipliers and can be factored out of the integration. A particularly simple source distribution function to evaluate, and the one investigated experimentally, is that of a rectangular electromagnetic field source,

$$J \times B = J_o B_o (H(x - a) - H(x - b)), \quad (3.14)$$

where H is the Heaviside function. Note that a and b are the x coordinant limits of the rectangular distribution defined in Fig. 3.7 and also in Fig. 3.2 . With Eq.(3.14) as the source function Eq. (3.13) becomes

$$\phi(x) = \frac{-j J_o B_o}{\omega \rho_o} \int_{-\ell}^{\ell} (\delta(x_o - a) - \delta(x_o - b)) G(x, x_o) dx_o. \quad (3.15)$$

To evaluate Eq. (3.15) the integration interval may be broken into three pieces: to the left of the source, the source region, and to the right of the source. The result is the generation of three functions which are valid to the left of the source volume, within the source volume, and to the right of the source volume.

$$\phi(x) = \frac{-j J_o B_o}{\omega \rho_o} \left\{ \begin{array}{l} \int_{-\ell}^b (\delta(x_o - a) - \delta(x_o - b)) G(x, x_o) dx_o \\ \qquad \qquad \qquad -\ell < x < a < b < \ell, \end{array} \right. \quad (3.16a)$$

$$\left\{ \begin{array}{l} \int_a^x (\delta(x_o - a) - \delta(x_o - b)) G(x, x_o) dx_o + \\ \int_x^b (\delta(x_o - a) - \delta(x_o - b)) G(x, x_o) dx_o \\ \qquad \qquad \qquad -\ell < a < x < b < \ell, \end{array} \right. \quad (3.16b)$$

$$\left\{ \begin{array}{l} \int_a^\ell (\delta(x_o - a) - \delta(x_o - b)) G(x, x_o) dx_o \\ \qquad \qquad \qquad -\ell < a < b < x < \ell. \end{array} \right. \quad (3.16c)$$

The evaluation of the integrals, Eqs. (3.16a,b,c), are given below. In the notation used below, G_L denotes the Green's function given in Eq. (3.12a), the left volume solution, and G_R denotes that given in Eq. (3.12b), the right volume solution.

$$\phi(x) = \frac{-j J_o B_o}{\omega \rho_o} \left\{ \begin{array}{ll} (G_L(x, a) - G_L(x, b)) & -\ell < x < a < b < \ell \end{array} \right. \quad (3.17a)$$

$$\left\{ \begin{array}{ll} (G_L(x, b) - G_R(x, a)) & -\ell < a < x < b < \ell \end{array} \right. \quad (3.17b)$$

$$\left\{ \begin{array}{ll} (G_R(x, a) - G_R(x, b)) & -\ell < a < b < x < \ell \end{array} \right. \quad (3.17c)$$

Equations (3.17a,b,c) represent the wavefield to the left of the source volume, within the source volume, and to the right of the source volume, respectively.

At this point the general solution to the MHD wave equation is not complete since the reflection coefficients, R_{ℓ} and $R_{-\ell}$, have not been determined. However, these reflection coefficients may be found by substitution of Eqs. (3.17a,b) into the boundary conditions given by Eqs. (3.3a,c). The result of this substitution is the following quadratic equations in terms of the reflection coefficients.

$$C_1 + C_2 R_{-\ell} + C_3 R_{-\ell}^2 = 0 \quad (3.18a)$$

$$C_4 + C_5 R_{\ell} + C_6 R_{\ell}^2 = 0 \quad (3.18b)$$

where the C's are complex constants (see Appendix C for the explicit forms).

The computation of the roots of Eqs. (3.18a,b) was performed by the subprogram unit REFL using the IMSL routine ZQADC. The magnitude of the reflection coefficient must be, by definition, less than or equal to one so the proper root choice was unambiguous. A plot of the reflection coefficient is given in Fig 3.8 for the waveguide dimensions given previously. Notice that the reflection coefficient declines with increasing frequency. This is because the real component of the self-impedance is increasing with frequency and therefore allowing more acoustic power to be transmitted out of the waveguide into the free medium.

The solution for the wavefield in terms of the velocity potential is now completely described by Eqs. (3.17a,b,c) with the solutions of Eqs. (3.18a,b) for the reflection coefficients. The expressions for the pressure field and particle velocity field are recovered by the transform equations,

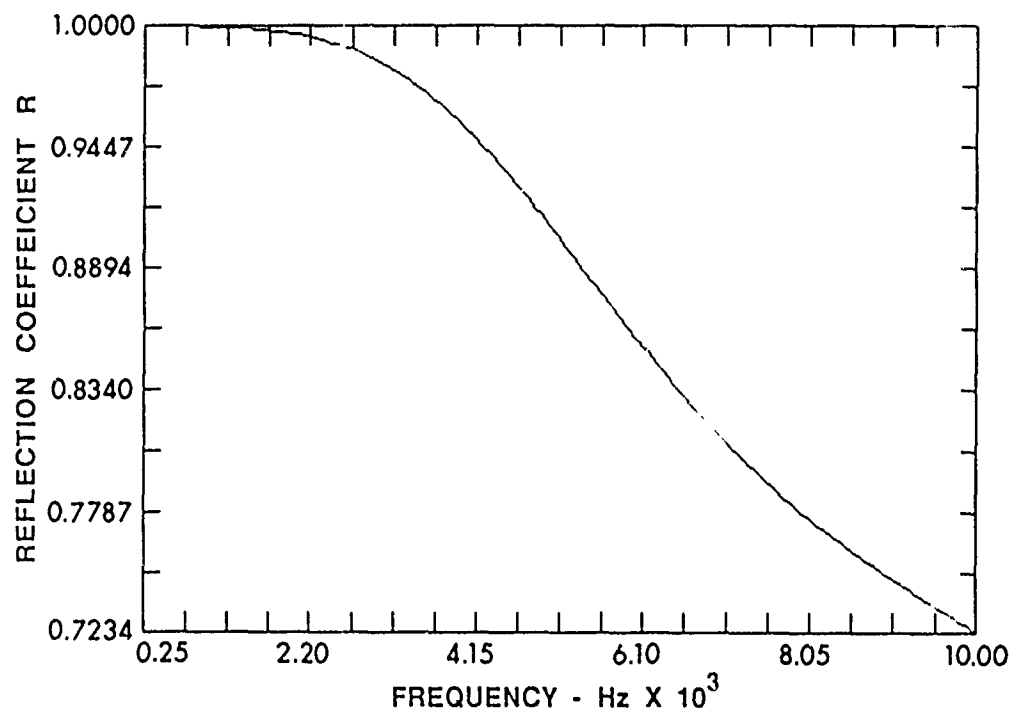


FIGURE 3.8
 MAGNITUDE OF THE REFLECTION COEFFICIENT
 $\ell = 0.10$ m, $\ell_s = 0.10$ m, $c_0 = 1550$ m/s, $R = 0.05$ m, $R_a = 0.02$ m

Eqs. (3.6a,b), and expressed below in terms of the Green's functions, Eqs. (3.12a,b), and the derivatives of the Green's functions.

$$G_x(x, x_0) = \begin{cases} \frac{(e^{jkx_0} + R_L e^{-jkx_0})(e^{-jkx} - R_L e^{jkx})}{2(1 - R_L R_{-L})} & -\ell < x < x_0 < \ell, \quad (3.19a) \\ \frac{-(e^{-jkx_0} + R_L e^{jkx_0})(e^{jkx} - R_L e^{-jkx})}{2(1 - R_L R_{-L})} & -\ell < x_0 < x < \ell, \quad (3.19b) \end{cases}$$

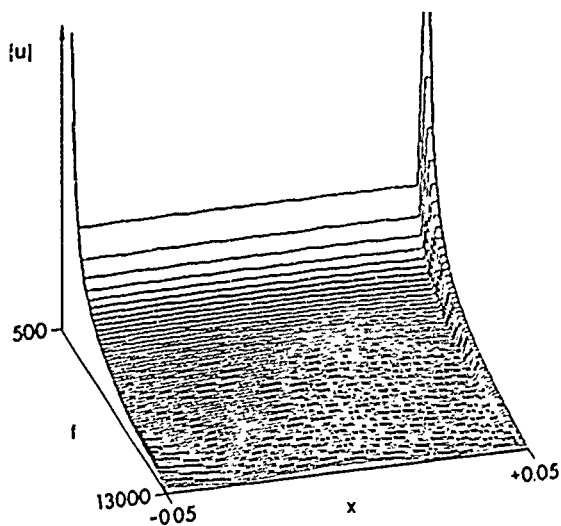
The complex pressure wavefield, $p(x)$, for the three regions of the transducer waveguide as a function of the axial coordinate x are as follows.

$$p(x) = \begin{cases} J_0 B_0 (G_L(x, a) - G_L(x, b)) & -\ell < x < a < b < \ell & (3.20a) \\ J_0 B_0 (G_L(x, b) - G_R(x, a)) & -\ell < a < x < b < \ell & (3.20b) \\ J_0 B_0 (G_R(x, a) - G_R(x, b)) & -\ell < a < b < x < \ell & (3.20c) \end{cases}$$

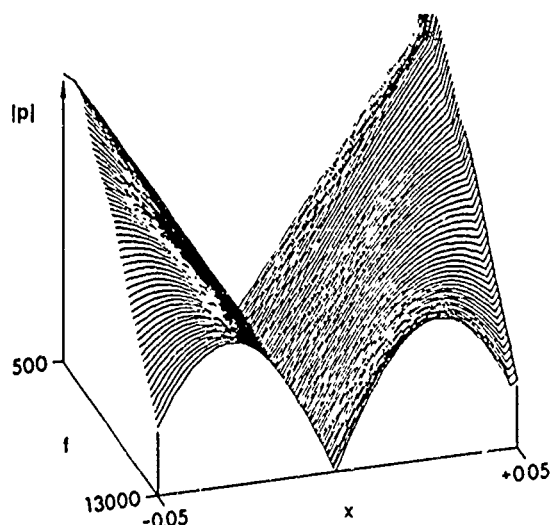
The complex particle velocity wavefield, $u(x)$, is as follows.

$$u(x) = \frac{-j J_0 B_0}{\omega \rho_0} \begin{cases} (G_{XL}(x, a) - G_{XL}(x, b)) & -\ell < x < a < b < \ell & (3.21a) \\ -(G_{XL}(x, b) - G_{XR}(x, a)) & -\ell < a < x < b < \ell & (3.21b) \\ (G_{XR}(x, a) - G_{XR}(x, b)) & -\ell < a < b < x < \ell & (3.21c) \end{cases}$$

Several plots of the modal particle velocity and pressure field amplitudes as a function of the waveguide x coordinate and frequency are shown in Figs. 3.9, 3.10, and 3.11. Figure 3.9 is for the case relevant to the experiment conducted. Shown in Fig. 3.9(a) is the modal particle velocity for a waveguide sound speed of 1536 m/s. It is important to note the step change in particle velocity at the aperture where there is a step change in acoustic impedance. Notice that as the frequency is increased the particle



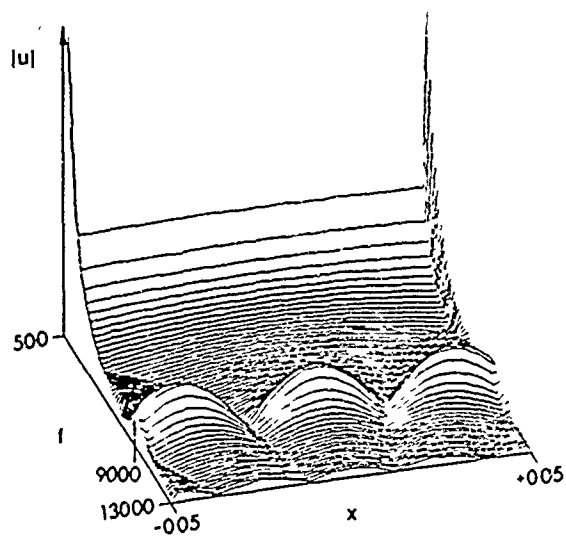
(a)
MAGNITUDE OF THE MODAL PARTICLE VELOCITY



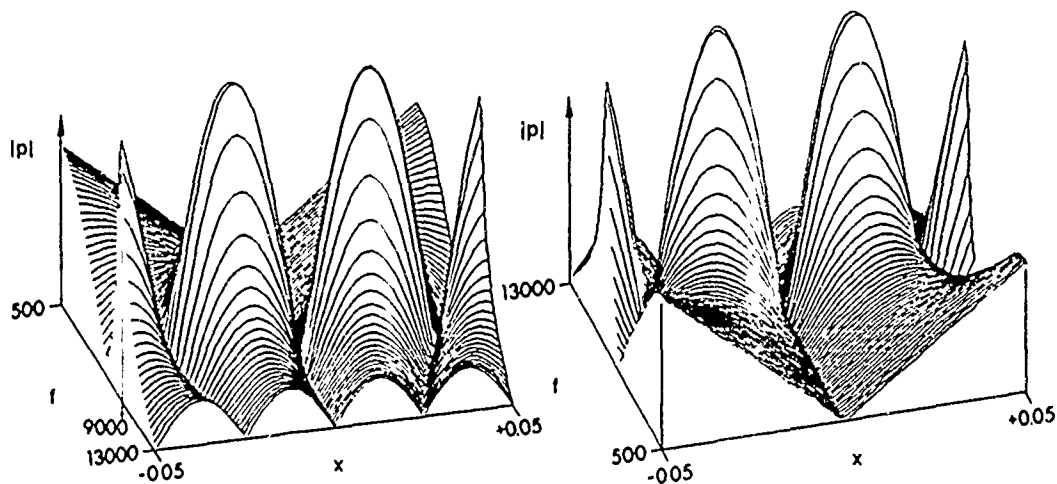
(b)
MAGNITUDE OF THE MODAL PRESSURE

FIGURE 3.9
MAGNITUDE OF THE MODAL PARTICLE VELOCITY
AND MODAL PRESSURE
6% NaCl-H₂O SOLUTION
 $\ell_s = 0.10$ m, $\ell = 0.10$ m, $c_0 = 1536$ m/s, $R = 0.09$ m

ARL UT
AS-CG-279
SCS-GA
6 2-86



(a)
MAGNITUDE OF THE MODAL PARTICLE VELOCITY



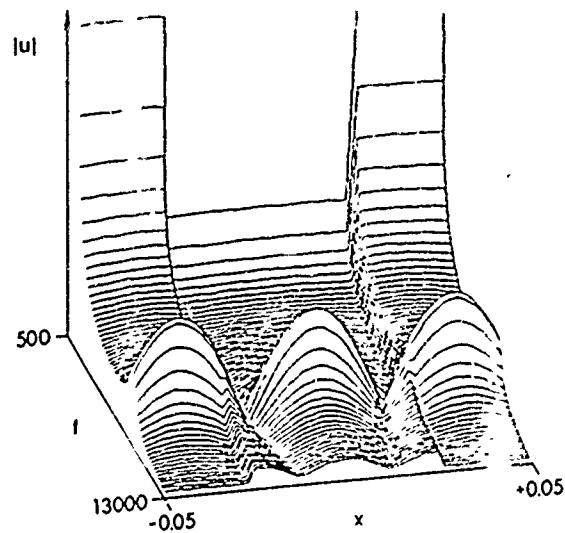
(b)
FORWARD VIEW

(c)
180° ROTATION OF (b)

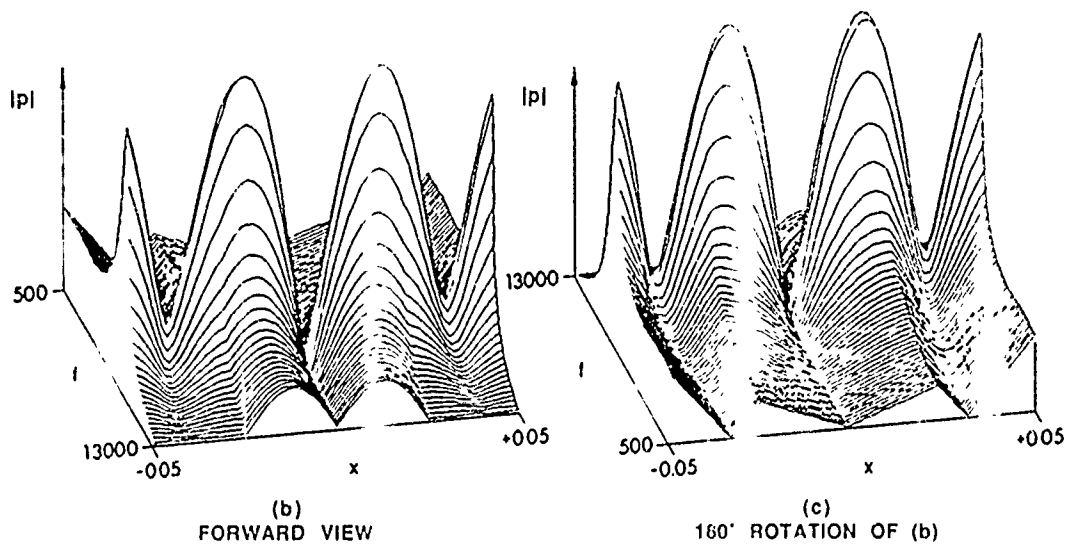
MAGNITUDE OF THE MODAL PRESSURE

FIGURE 3.10
MAGNITUDE OF THE MODAL PARTICLE VELOCITY
AND MODAL PRESSURE
6% NaCl-H₂O SOLUTION
 $\ell_s = 0.10$ m, $\ell = 0.10$ m, $c_0 = 650$ m/s, $R = 0.09$ m

ARL UT
AS-86-277
SCS - GA
6-2-86



(a)
MAGNITUDE OF THE MODAL PARTICLE VELOCITY



(b) FORWARD VIEW
(c) 160° ROTATION OF (b)
MAGNITUDE OF THE MODAL PRESSURE

FIGURE 3.11
MAGNITUDE OF MODAL PARTICLE VELOCITY
AND MODAL PRESSURE
6% NaCl-H₂O SOLUTION
 $t_s = 0.05$ m, $t = 0.10$ m, $c_0 = 650$ m/s, $R = 0.09$ m

ARL UT
AS 86.278
LCS GA
6 2 86

velocity in the waveguide and the step change in velocity at the aperture decrease. The decrease in waveguide particle velocity with increasing frequency is due to the inertia effect of the fluid. The decreasing step change at the aperture is due to the increasing aperture impedance with frequency (see Figs. 3.3(a) and (b)).

In Figs. 3.10(a) and (b) the sound speed in the waveguide was set at 650 m/s to demonstrate the resonance behavior of the waveguide at lower frequencies. At approximately 9000 Hz there is a resonant standing wave. This first resonance is approximately a $3/2$ wavelength mode and is the first mode because at this frequency the aperture impedance has become large enough to allow a "hard" reflective waveguide termination and thus support of a reduced aperture particle velocity.

Figure 3.11(a) and (b) show the modal behavior generated by an MHD source which is 0.05 m and centered in a 0.10 m waveguide. This plot is for a reduced sound speed of 650 m/s, but what is exemplified is the discontinuity of the wavefields due to the presence of the MHD volume force. The FORTRAN program MHD has the capability to calculate the acoustic response from any rectangular MHD source distribution anywhere in the region of the defined waveguide length.

D. ACOUSTIC WAVEFIELD DUE TO THE THERMOACOUSTIC SOURCE

Considered first was the pressure wavefield due to the MHD source mechanism. The pressure field contribution of the thermoacoustic mechanism is now derived. The Fourier transform with respect to time of the inhomogeneous wave equation for the thermoacoustic source is given by

$$p_{xx} + k^2 p = \frac{j \Omega \beta J^2(x)}{2 \sigma C_p} \quad (3.22)$$

where $k = \Omega/c_0$, and Ω is defined as 2ω . The solution procedure is the same as that performed for the MHD source. The thermoacoustic inhomogeneous wave equation, Eq. (3.22), has the same inhomogeneous boundary conditions as the MHD wave equation solved previously. Again a transformation to the velocity potential is made using Eqs. (3.6a,b). The two-point boundary value problem for the thermoacoustic source generated wavefield in the waveguide in terms of one dependent variable, ϕ , is thus

$$\phi_{xx} + k^2 \phi = \frac{\beta J^2(x)}{2 \sigma \rho_0 C_p} \quad (3.23a)$$

subject to the boundary conditions,

$$-j \Omega \rho_0 \phi(\ell) + \phi_x(\ell) Z_s - \phi_x(-\ell) Z_m = 0 \quad (3.23b)$$

and

$$-j \Omega \rho_0 \phi(-\ell) - \phi_x(-\ell) Z_s + \phi_x(\ell) Z_m = 0 \quad (3.23c)$$

The solution of Eqs. (3.23a,b,c) may be achieved by use of the Green's function derived in Section 3.3, and rewritten below.

$$G(x, x_0) = \begin{cases} \frac{j (e^{jkx_0} + R_\ell e^{-jkx_0}) (e^{-jkx} + R_\ell e^{jkx})}{2k(1 - R_\ell R_\ell)} & -\ell < x < x_0 < \ell, \quad (3.24a) \\ \frac{j (e^{-jkx_0} + R_\ell e^{jkx_0}) (e^{jkx} + R_\ell e^{-jkx})}{2k(1 - R_\ell R_\ell)} & -\ell < x_0 < x < \ell. \quad (3.24b) \end{cases}$$

The solution of the thermoacoustic pressure wavefield, in terms of the velocity potential and the above Green's function, is stated in integral form as

$$\phi(x) = \frac{\beta}{2 \sigma \rho_o C_p} \int_{-\ell}^{\ell} J^2(x_o) G(x, x_o) dx_o. \quad (3.25)$$

The source distribution function investigated in the experiment, is a rectangular electromagnetic field. Therefore the current density has the rectangular distribution

$$J(x) = J_o (H(x - a) - H(x - b)), \quad (3.26)$$

where J_o is the current density amplitude and H is the Heaviside function. With Eq.(3.26) as the source function Eq. (3.25) becomes

$$\phi(x) = \frac{\beta J_o}{2 \sigma \rho_o C_p} \int_{-\ell}^{\ell} (H(x_o - a) - H(x_o - b)) G(x, x_o) dx_o. \quad (3.27)$$

The iterated integration of Eq. (3.27) for the three regions of the waveguide are given on the next page.

$$\phi(x) = \frac{\beta J_o^2}{2 \sigma \rho_o C_p} \left\{ \begin{array}{l} \int_{-\ell}^b (H(x_o - a) - H(x_o - b)) G(x, x_o) dx_o \\ \qquad \qquad \qquad \ell < x < a < b < \ell, \quad (3.28a) \\ \\ \int_a^x (H(x_o - a) - H(x_o - b)) G(x, x_o) dx_o + \\ \int_x^b (H(x_o - a) - H(x_o - b)) G(x, x_o) dx_o \\ \qquad \qquad \qquad -\ell < a < x < b < \ell, \quad (3.28b) \end{array} \right.$$

$$\left\{ \begin{array}{l} \int_a^{\ell} (H(x_o - a) - H(x_o - b)) G(x, x_o) dx_o \\ -\ell < a < b < x < \ell. \end{array} \right. \quad (3.28c)$$

The results of evaluating the integrals for the velocity potential wavefield are as follows for the step function source.

$$\phi(x) = \frac{\beta J_o^2}{2 \sigma \rho_o C_p} \left\{ \begin{array}{l} \frac{(-(e^{jka} - e^{jkb}) + R_{\ell}(e^{-jka} - e^{-jkb}))(e^{-jkx} + R_{\ell}e^{jkx})}{2 k^2 (1 - R_{\ell}R_{\ell})} \\ -\ell < x < a < b < \ell, \end{array} \right. \quad (3.29a)$$

$$\left\{ \begin{array}{l} \frac{(e^{-jka} - R_{\ell}e^{jka})(e^{jkx} + R_{\ell}e^{-jkx})}{2 k^2 (1 - R_{\ell}R_{\ell})} + \\ \frac{(e^{jkb} - R_{\ell}e^{-jkb})(e^{-jkx} + R_{\ell}e^{jkx})}{2 k^2 (1 - R_{\ell}R_{\ell})} - \frac{1}{k^2} \\ -\ell < a < x < b < \ell, \end{array} \right. \quad (3.29b)$$

$$\left\{ \begin{array}{l} \frac{((e^{-jka} - e^{-jkb}) - R_{\ell}(e^{jka} - e^{jkb}))(e^{jkx} + R_{\ell}e^{-jkx})}{2 k^2 (1 - R_{\ell}R_{\ell})} \\ -\ell < a < b < x < \ell. \end{array} \right. \quad (3.29c)$$

Equations (3.29a,b,c) represent the velocity potential wavefield to the left, within, and to the right of the source volume, respectively.

The reflection coefficients are found by substitution of Eqs. (3.29a,c) into the boundary conditions given by Eqs. (3.3a,b). The result of this substitution is the following quadratic equations in terms of the reflection coefficients,

$$C_1 + C_2 R_{\ell} + C_3 R_{\ell}^2 = 0, \quad (3.30a)$$

$$C_4 + C_5 R_{\ell} + C_6 R_{\ell}^2 = 0, \quad (3.30b)$$

where the C's are complex constants (see Appendix C for the explicit forms). The computation of the roots of Eqs. (3.30a,b) was performed by the subprogram unit REFL of program THERMO using the IMSL routine ZQADC. A plot of the reflection coefficient magnitude is given in Fig. 3.8 for the waveguide dimensions given previously. Note that Fig. 3.8 was computed using the MHD solution; however the magnitude of the reflection coefficient is the same for both cases; the difference occurs in the phase.

The solution for the thermoacoustic wavefield in terms of the velocity potential is now completely described by Eqs. (3.29a,b,c) with the solutions of Eqs. (3.30a,b) for the reflection coefficients. The expressions for the pressure field and particle velocity field were recovered by the transform equations, Eqs. (3.6a,b), applied to Eqs. (3.29a,b,c) and these are stated below.

$$p(x) = \frac{j \beta c_o J_o^2}{2 \sigma \rho_o C_p} \left\{ \begin{array}{l} \frac{(-e^{jka} - e^{jkb}) + R_\ell(e^{jka} - e^{jkb}))}{2k(1 - R_\ell R_\ell)} (e^{-jkx} + R_\ell e^{jkx}) \\ \qquad \qquad \qquad \ell < x < a < b < \ell, \quad (3.31a) \\ \frac{(e^{-jka} - R_\ell e^{jka})(e^{jkx} + R_\ell e^{-jkx})}{2k(1 - R_\ell R_\ell)} + \\ \frac{(e^{jkb} - R_\ell e^{-jkb})(e^{-jkx} + R_\ell e^{jkx})}{2k(1 - R_\ell R_\ell)} - \frac{1}{k} \\ \qquad \qquad \qquad \ell < a < x < b < \ell, \quad (3.31b) \\ \frac{((e^{-jka} - e^{jkb}) - R_\ell(e^{jka} - e^{jkb}))}{2k(1 - R_\ell R_\ell)} (e^{jkx} + R_\ell e^{-jkx}) \\ \qquad \qquad \qquad -\ell < a < b < x < \ell. \quad (3.31c) \end{array} \right.$$

$u(x)$ is the complex particle velocity field in the transducer waveguide.

$$u(x) = \frac{j \beta J_o^2}{2 \sigma \rho_o C_p} \left\{ \begin{array}{l} \frac{((e^{jka} - e^{jkb}) - R_\ell(e^{-jka} - e^{-jkb}))(e^{-jkx} - R_\ell e^{jkx})}{2k(1 - R_\ell R_\ell)} \quad -\ell < x < a < b < \ell, \quad (3.32a) \\ \frac{(e^{-jka} - R_\ell e^{jka})(e^{jkx} - R_\ell e^{-jkx})}{2k(1 - R_\ell R_\ell)} \\ - \frac{(e^{jkb} - R_\ell e^{-jkb})(e^{-jkx} - R_\ell e^{jkx})}{2k(1 - R_\ell R_\ell)} \quad -\ell < a < x < b < \ell, \quad (3.32b) \\ \frac{((e^{-jka} - e^{-jkb}) - R_\ell(e^{jka} - e^{jkb}))(e^{jkx} - R_\ell e^{-jkx})}{2k(1 - R_\ell R_\ell)} \quad -\ell < a < b < x < \ell. \quad (3.32c) \end{array} \right.$$

Unfortunately time did not permit the author to write the computer code necessary to generate the three-dimensional plots of the pressure and particle velocity modes, as was done for the MHD mechanism.

CHAPTER 4

THEORY: ELECTROACOUSTIC RELATIONS

This chapter is concerned with the determination of the transduction characteristics: input electrical impedance, real and reactive input electrical power, power efficiency, current and voltage transmitting sensitivity for the MHD acoustic source mechanism, and thermoacoustic source mechanism.

A. POLARIZATION IMPEDANCE OF THE MHD WAVEGUIDE ELECTRODES

In general when considering the impedance of an electrolyte fluid contained in a cell with metal electrodes two independent processes must be analyzed: the frequency dependent nature of the electrolyte and the electrical characteristics of the electrolyte interaction with the electrode surface.

The conductivity of an electrolyte not in the vicinity of an electrode surface is "classically" analyzed using the theories of Debye and Huckel¹⁵ and Debye and Falkenhagen.¹⁶ The conductivity for a 1,1 valent electrolyte, such as NaCl in water, is dependent on the applied electric field strength, concentration of NaCl, and frequency. However, for NaCl in water at 1 M concentration with electric fields less than 1×10^5 V/cm and frequencies less than 18 MHz, the conductivity is constant ($\sigma = 5.28 \text{ 1/(\ohm m)}$).

At an electrode-electrolyte interface a potential difference is present. The potential arises from the electrons on the metal surface and the ions in the electrolyte attracting each other according to Coulomb's law. This charge distribution at an interface is known as the electrical double layer in

the electrochemical literature.¹⁷ The important concept is that the mobile ions have a tremendous capacity for charge storage and thus a very significant capacitive impedance when a time harmonic signal is applied to the electrode.

For the case of planar electrodes, of interest in this investigation, the Gouy-Chapman¹⁸ model of the double layer capacitance is given as,¹⁹

$$C_D = \frac{e_o F^2 z N^{1/2} (b-a) \ell_y}{4 \pi R T} \quad (4.1)$$

where

- $C_D \equiv$ double layer capacitance, F,
- $e_o \equiv$ dielectric permittivity, 8.85×10^{-12} F/m
- $F \equiv$ Faraday constant, 96524 C/mole,
- $N \equiv$ concentration of electrolyte, moles/m³,
- $R \equiv$ ideal gas constant, 8.31 joules/°K mole,
- $T \equiv$ absolute temperature, 293 °K (20° C)
- $z \equiv$ charge valence of the ionized molecule, 1, and
- $(b - a) \ell_y \equiv$ electrode area.

For a 1 M NaCl electrolyte solution the Chapman model predicts the capacitance, on a per unit area basis, to be 52 mF/m². Measurements made by Vetter²⁰ indicate a range of values of 100-400 mF/m². This will be discussed more in Chapter 5 in regard to the value measured for the MHD transducer.

In addition to the double layer capacitance of the electrode interface there is an additional impedance effect observed due to an ion concentration gradient near the electrode. This is due to electrochemical

reaction processes. The transfer of charge at the interface causes electrochemical reactions which result in the depletion of the original electrolyte ions and the production of other ions and molecules. Since the ion concentration gradient represents a charge gradient one can expect an electric potential to result. The Nernst equation²¹ describes this potential, V_d ,

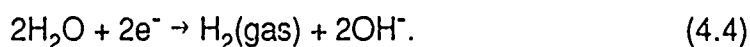
$$V_d = \frac{RT}{nF} \ln \left(\frac{N(o,t)}{N_o} \right) \quad (4.2)$$

in terms of $N(o,t)$, the ion concentration at the electrode surface ($\xi=0$) as a function of time, and N_o , the equilibrium ion concentration "far" from the electrode. n is the number of moles of electrons required to form one mole of reaction product.

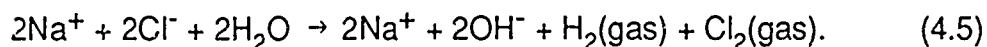
In order to apply Eq. (4.2) the electrochemical reactions at the electrodes must be determined. The kinetically acceptable electrode reactions for NaCl and water are



which is the anode or oxidation reaction. This reaction represents the conversion of the chloride ion to chlorine gas with the donation of electrons to the electrode. The other electrode reaction is the cathode or reduction reaction,

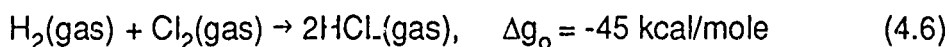


Note that dissociation of water in the cathode reaction is preferred over the reduction of sodium ion to solid sodium ($\text{Na}^+ + \text{e}^- \rightarrow \text{Na}(\text{solid})$). The overall chemical reaction can be stated as



It can be seen from the reaction equation, Eq. (4.5), that the chloride ion will experience a concentration gradient. Note that water does not contribute to the ion concentration gradient of the electrolyte since water is not ionized and is the solvent and is thus in great supply in the vicinity of the electrodes. Since the hydroxide ion is produced one might ask whether it is a more preferable oxidation reaction molecule than the chloride atom. Kinetically it is not.

One last item needs to be addressed with regard to the formation of hydrogen and chlorine gas. The reaction,



is a spontaneous, very exothermic reaction as evidenced by the large reduction in the Gibbs free energy, Δg_o . However, as a practical matter the gases do not always combine but can nucleate on the electrodes. The result of the gas formation and the effect on operation of the transducer is discussed later in this chapter and in Chapter 5.

The concentration distribution, $N(\xi, t)$, for the evaluation of the Nernst equation, Eq. (4.2), is based on the concentration of the chloride ion as a function of the rate at which it is oxidized. Since the boundary of the electrolyte is a plane electrode surface, which is the boundary of the waveguide of the same cross-section, the concentration will only vary in the y direction of the waveguide coordinate system. Therefore the distribution should only be a function of one spatial dimension, ξ . The diffusion equation

is stated as

$$\text{(Fick's second law)} \quad N(\xi, t)_t = D N(\xi, t)_{\xi\xi}, \quad (4.7a)$$

subject to the following boundary conditions.

$$\text{(Fick's first law)} \quad N(0, t) = \frac{J v}{n F D} e^{-j\omega t} \quad (4.7b)$$

and

$$\lim_{\xi \rightarrow \infty} N(\xi, t) = N_o, \quad (4.7c)$$

and the initial condition,

$$N(\xi, 0) = N_o. \quad (4.7d)$$

In the above equations, D is the diffusion constant, J is the current density amplitude defined previously, and v is the number of moles of ions needed to produce one mole of product ($v = 2$ for the chloride ion reaction). The solution of Eq. (4.7a) is given as²²

$$N(\xi, t) = N_o + \frac{J v}{n F \sqrt{D \omega}} e^{-\sqrt{\omega/2D} \xi} e^{-j(\omega t - \sqrt{\omega/2D} \xi - \pi/4)}. \quad (4.8)$$

Equation (4.8) represents an exponentially damped, dispersive, outgoing diffusion wave. However, one might not accept the boundary condition, Eq. (4.7c), and thus the solution, Eq. (4.8), as being a valid solution to the boundary value problem, which actually involves not an infinite positive domain, but a finite domain problem with another electrode at $\xi = \ell_y$. From the coefficient $e^{-\sqrt{\omega/2D} \xi}$ of Eq. (4.8) it is seen that the concentration distribution is spatially exponentially damped and that for $\sqrt{\omega/2D} \xi = 4$ the diffusion wave is 98% decayed. At 500 Hz and $D = 1.0 \times 10^{-9} \text{ m}^2/\text{s}$, the diffusion wave is damped 98% in 0.003 mm, which is a very small distance compared to 3.81 cm, the electrode separation used in the

experiment. Hence Eq. (4.8) is a good approximation for this investigation.

The Nernst equation, Eq. (4.2), can now be evaluated using Eq. (4.8). Note that in order to linearize $\ln(\)$ in terms of the current density so that a linear relation between current and voltage is obtained, it must be assumed that the change in concentration represented by the second term of Eq. (4.8) is small compared to N_o . This condition is met if

$$J \ll \frac{N_o F n \sqrt{D \omega}}{v} \quad (4.9)$$

At 500 Hz the right side of Eq. (4.9) equals $1.71 \times 10^5 \text{ A/m}^2$. The experiments were performed at a current density of $1.5 \times 10^4 \text{ A/m}^2$, which is a factor of 10 less than the constraint and represents approximately a 5% linearization error of $\ln(\)$. Substituting Eq. (4.8) into Eq. (4.2) and linearizing, the Nernst equation becomes

$$V_d = \frac{J R T v^2}{n^2 F^2 N_o \sqrt{D \omega}} e^{-j(\omega t - \pi/4)} \quad (4.10)$$

From Eq. (4.10) the diffusion impedance for the waveguide electrode can be defined as

$$Z_d = \frac{R T v^2 (1 - j)}{\ell_y (b - a) n^2 F^2 N_o \sqrt{2 D \omega}} \quad (4.11)$$

where the current is defined as $J \ell_y (b - a)$.

The electrical circuit interpretation of Eq. (4.11) is that of a resistor and capacitor in series, with the resistive and capacitive impedance having the equal magnitudes and creating a current lag of -45° . Notice that

the resistive component, R_d , is proportional to $1/\sqrt{\omega}$. The capacitive nature of Eq. (4.11) can be separated from the resistive by assuming the impedance form $1/j \omega C_d$, which yields the expression for C_d , the diffusion capacitance, that is also a function of $1/\sqrt{\omega}$,

$$C_d = \frac{\ell_y (b - a) \sqrt{2D} n^2 F^2 N_o}{R T v^2 \sqrt{\omega}} \quad (4.12)$$

Finally the complete electrolyte-electrode circuit topology²³ can be assembled, given the expressions, Eqs. (4.1) and (4.11), for the values of the elements, as shown in Fig. 4.1. The diffusion impedance in parallel with the double layer capacitance is termed the polarization impedance, Z_p , of the electrode. Note that in Fig. 4.1 the impedance of the electrolyte is represented by the complex impedance element Z . This is done so that the impedance due to the acoustic coupling can be included in a complete circuit model of the input electrical impedance. The analysis of Z is discussed in the next section of this chapter.

B. ELECTRICAL IMPEDANCE OF THE MHD TRANSDUCTION PROCESS

The electrical impedance of the transducer due to the interaction of the electrolyte with the acoustic field is defined as the voltage across divided by input current through the impedance element Z of Fig 4.1. The input current I is found by integrating the current density over a surface near the electrodes (four diffusion layers away, $4/\sqrt{\omega/2D}$).

$$I = \int_S \mathbf{J} \cdot d\mathbf{S} \quad (4.13)$$

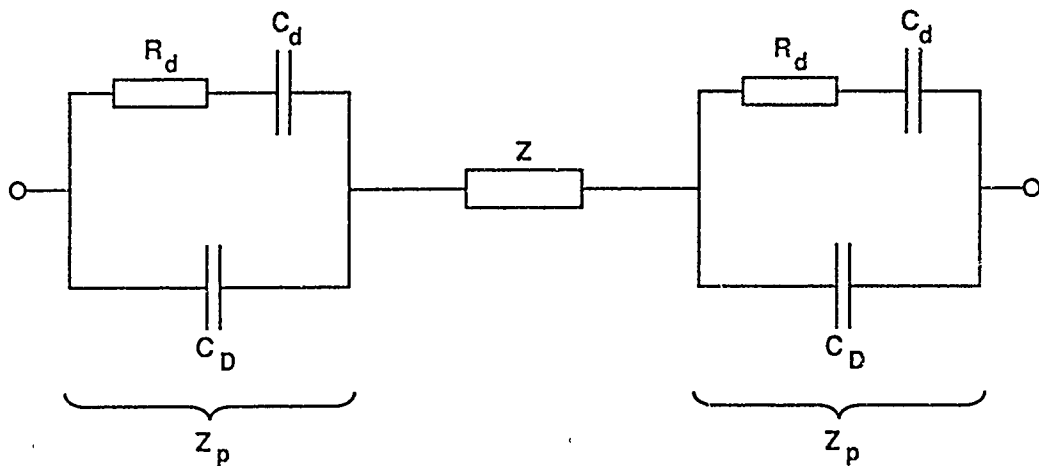


FIGURE 4.1
EQUIVALENT CIRCUIT OF THE MHD INPUT IMPEDANCE

The voltage is defined as the path integral of the electric field between the electrodes, but not near the surface,

$$V = \int_{\text{path between electrodes}} \mathbf{E} \cdot d\mathbf{l} . \quad (4.14)$$

Using the above integral definitions the electrolyte impedance is defined as follows.

$$Z = \frac{\int_{\text{path between electrodes}} \mathbf{E} \cdot d\mathbf{l} .}{\int_S \mathbf{J} \cdot d\mathbf{S}} \quad (4.15)$$

Evaluation of the numerator of Eq. (4.15) follows from assuming that the surface integration near the electrodes is at a constant electric field value.

Substituting Eq. (2.28) into Eq. (4.15), to take account of the induced electric field, and substituting Eq. (3.21c) for u , the impedance is

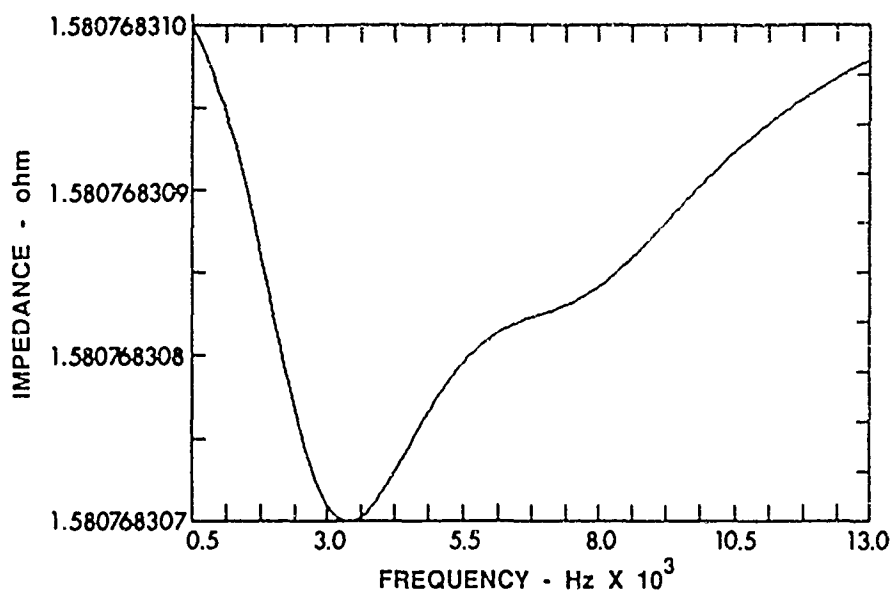
$$Z = \frac{\int_0^{l_y} dy}{\frac{\sigma}{\omega \rho_o} \int_0^{l_z} \int_a^b (1 + j \sigma B_o^2 (G_{XL}(x,b) - G_{XR}(x,a))) dx} . \quad (4.16)$$

Performing the integration,

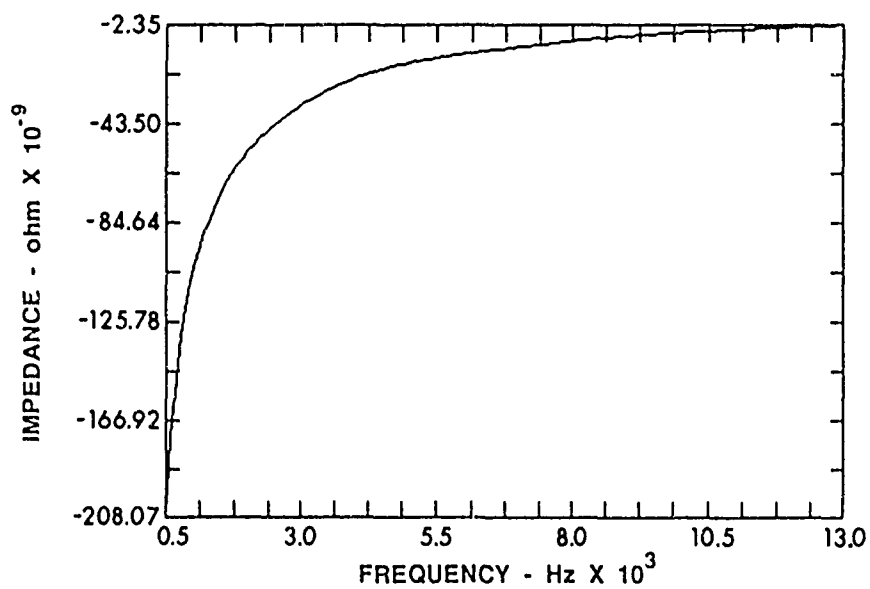
$$Z = \left(\frac{\sigma \ell_z (b-a)}{\ell_y} + \frac{j \sigma^2 B_o^2 \ell_z}{\omega \rho_o \ell_y} (G_L(b,b) - G_L(a,b) - G_R(b,a) + G_R(a,a)) \right)^{-1} \quad (4.17)$$

Shown in Figs. 4.2(a) and (b) are the real and imaginary components of the electrolyte impedance for the waveguide filled with a 6% NaCl-water solution. The transducer boundary conditions of the waveguide are those of the transducer used in the experiment discussed in Chapter 5. For the 6% NaCl solution at 500 Hz the impedance is $1.581 - j 0.2 \times 10^{-6}$. The important result is that the real component for 6% NaCl is relatively constant over the frequency band from 500 to 13000 Hz and the imaginary component is negligible.

From the preceding discussions it can be concluded that the electrolyte impedance can be assumed to be real and constant for NaCl-water, except at "low" frequencies and/or high magnetic fields ($B \gg 1T$) for a high conductivity fluid such as mercury. It is justifiable therefore to state Ohm's law as Eq. (2.2) for the electrolyte impedance.



(a)
REAL ADMITTANCE



(b)
IMAGINARY ADMITTANCE

FIGURE 4.2
MHD MECHANISM IMPEDANCE FOR
6% NaCl-H₂O SOLUTION
 $\ell_s = 0.10$ m, $\ell = 0.10$ m, $c_0 = 1550$ m/s, $R = 0.09$ m

ARL:UT
AS-86-429
SCS - GA
8 - 6 - 86

C. MHD TRANSDUCTION PROCESS POWER EFFICIENCY

The transduction power efficiency is defined as the real component of the radiated acoustic power divided by the real component of the input electrical power plus the real component of the radiated power. The complex input power expression is

$$W_e = I^2 Z_t, \quad (4.18)$$

where Z_t is the transducer terminal impedance defined as

$$Z_t = 2Z_p + Z_s. \quad (4.19)$$

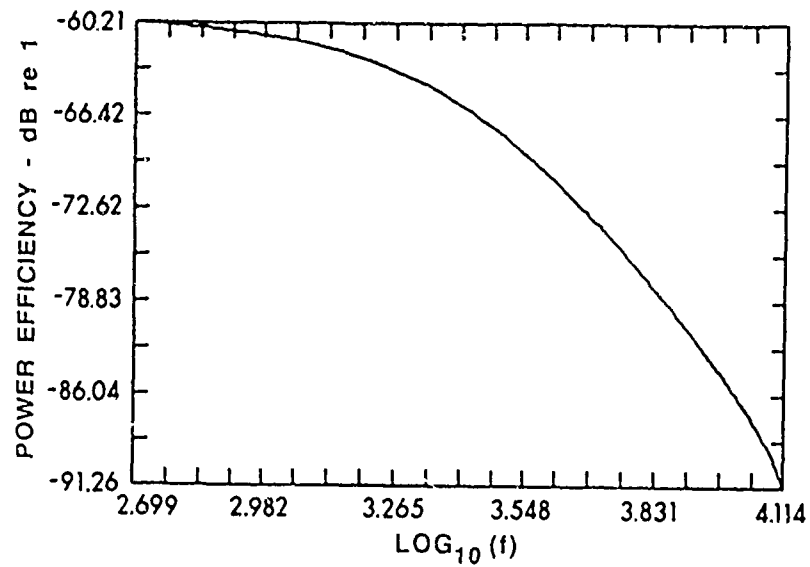
To calculate the total radiated acoustic power the real component of the acoustic self-impedance $\text{Re}(Z_s)$ and the acoustic particle velocity evaluated at the aperture are integrated over the surface of the aperture.

$$W_A = \int_{\text{aperture at } l} |u(l)|^2 \text{Re}(Z_s) ds + \int_{\text{aperture at } -l} |u(-l)|^2 \text{Re}(Z_s) ds \quad (4.20)$$

To calculate the power efficiency, the ratio of Eq. (4.20) to the real component of Eq. (4.18) is taken,

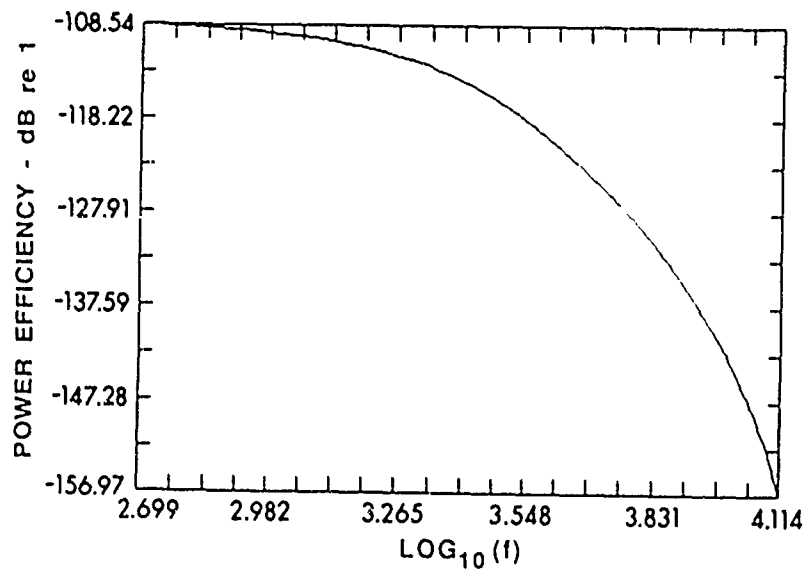
$$\eta = \frac{W_A}{\text{Re}(W_e)}. \quad (4.21)$$

Shown in Fig. 4.3(a) and (b) are plots for mercury and the 6% NaCl solution used in the experiment, respectively. At low frequencies the efficiency is higher because the particle velocity is higher since there is low acoustic aperture impedance at low frequencies. As the frequency increases, up to



(a)

MERCURY $\ell = 0.10$ m, $\ell_s = 0.10$ m
 $c_0 = 1450$ m/s, $R = 0.09$ m



(b)

6% NaCL-H₂O SOLUTION
 $\ell = 0.10$ m, $\ell_s = 0.10$ m, $c_0 = 1550$ m/s, $R = 0.09$ m

FIGURE 4.3
 MHD TRANSDUCTION PROCESS POWER EFFICIENCY

the first resonance, the particle velocity decreases faster than the real component of the radiation impedance increases, and thus there is a decreasing trend in the efficiency.

D. MHD TRANSMITTING CURRENT SENSITIVITY

The transmitting current sensitivity (TCS) is defined as the ratio of output acoustic pressure at 1 m at an angle ψ to 1 A electrical input current. The TCS is also defined for the special case of the transducer waveguide axis (x axis response, $\psi = 0^\circ$, and range of 1 m). The expression for the farfield pressure, Eq. (B.4), is analytically and computationally simpler than the full spherical harmonic function expansion used to express the mutual acoustic impedances. The farfield equation has the Hankel function components replaced by the large argument, $kr \gg 1$, asymptotic expression e^{ikr} . Although the farfield approximation, in general, is not always valid at a distance of 1 m, this treatment is standard for determining transmitting sensitivities. The advantage of this definition is that the pressure field may be extrapolated to the farfield region by assuming ordinary spherical spreading (which is generally the region of interest). The TCS expressions for the MHD source mechanism in the farfield are given as

$$TCS \equiv p_{ff}(r = 1 \text{ meter}, \psi)/I$$

where, from Eqs.(B.4) and (3.21), the TCS can be stated as

$$TCS = \frac{B_o \rho_{fm} c_{fm}}{2 \omega \rho_o k \ell_z (b-a)}$$

$$\left\{ - (G_{XL}(-\ell, a) - G_{XL}(-\ell, b)) \sum_{n=0}^{\infty} \frac{(P_{n-1}(\cos\Theta) - P_{n+1}(\cos\Theta)) P_n(-\cos\psi) e^{-j\pi(n+1)/2}}{\left. \frac{d}{dx} h_n^1(x) \right|_{x=kR}} \right. \\ \left. + (G_{XR}(\ell, a) - G_{XR}(\ell, b)) \sum_{n=0}^{\infty} \frac{(P_{n-1}(\cos\Theta) - P_{n+1}(\cos\Theta)) P_n(\cos\psi) e^{-j\pi(n+1)/2}}{\left. \frac{d}{dx} h_n^1(x) \right|_{x=kR}} \right\} \quad (4.22a)$$

The x axis transmitting sensitivity is given below as a special case of Eq. (4.22a).

$$TCS_o \equiv p_{if}(r = 1 \text{ meter}, \psi = 0^\circ)/l$$

$$TCS_o = \frac{B_o \rho_{fm} c_{fm}}{2 \omega \rho_o k \ell_z (b-a)}$$

$$\left\{ - (G_{XL}(-\ell, a) - G_{XL}(-\ell, b)) \sum_{n=0}^{\infty} \frac{(P_{n-1}(\cos\Theta) - P_{n+1}(\cos\Theta)) (-1)^n e^{-j\pi(n+1)/2}}{\left. \frac{d}{dx} h_n^1(x) \right|_{x=kR}} \right. \\ \left. + (G_{XR}(\ell, a) - G_{XR}(\ell, b)) \sum_{n=0}^{\infty} \frac{(P_{n-1}(\cos\Theta) - P_{n+1}(\cos\Theta)) e^{-j\pi(n+1)/2}}{\left. \frac{d}{dx} h_n^1(x) \right|_{x=kR}} \right\} \quad (4.22b)$$

In general the transmitting sensitivity is the most important frequency dependent relation for a transducer. The expressions stated above have many geometric parameters which affect the transmitting

sensitivity in very pronounced ways. It is not the intent of this thesis to probe into a detailed parametric investigation of the sensitivity functions but to point out a few important points. In Figs. 4.4(a), (b), 4.5(a), (b), and 4.6(a), (b) plotted in three dimensions is the current sensitivity on the waveguide axis (TCS_0) versus frequency versus a geometric parameter or fluid property for a specified set of constant parameters.

The variation of the sensitivity with waveguide sound speed proved to be of practical utility when analyzing the experimental data. When current is passed through the NaCl solution in the transducer it is inevitable that some hydrogen and chlorine gas bubbles will be generated. The effect of the gases is to lower the acoustic phase speed due to the large increase in the small signal compressibility of the medium.

The transmitting current sensitivity surface shown in Fig. 4.4(a) is for the case of a 0.03 m source centered in a 0.10 m long waveguide with a 0.09 m baffle radius (an aperture radius of 0.0196 m is used in all plots). Compared to Fig. 4.4(b), which is for a source of 0.10 m with the same baffle, the shorter source seems to excite a sharper resonance due to the source volume being spatially a better fit to the excited "3/2 wave length pressure mode". (See Figs. 3.8, 3.9, and 3.10 for diagrams of the particle velocity and pressure modes.)

At higher sound speeds a null forms in the sensitivity surface. The null corresponds to the destructive interference of the acoustic radiation in the farfield and is primarily dependent on the radius of the baffle. Notice that the null occurs at the same frequency, approximately 6400 Hz. in both

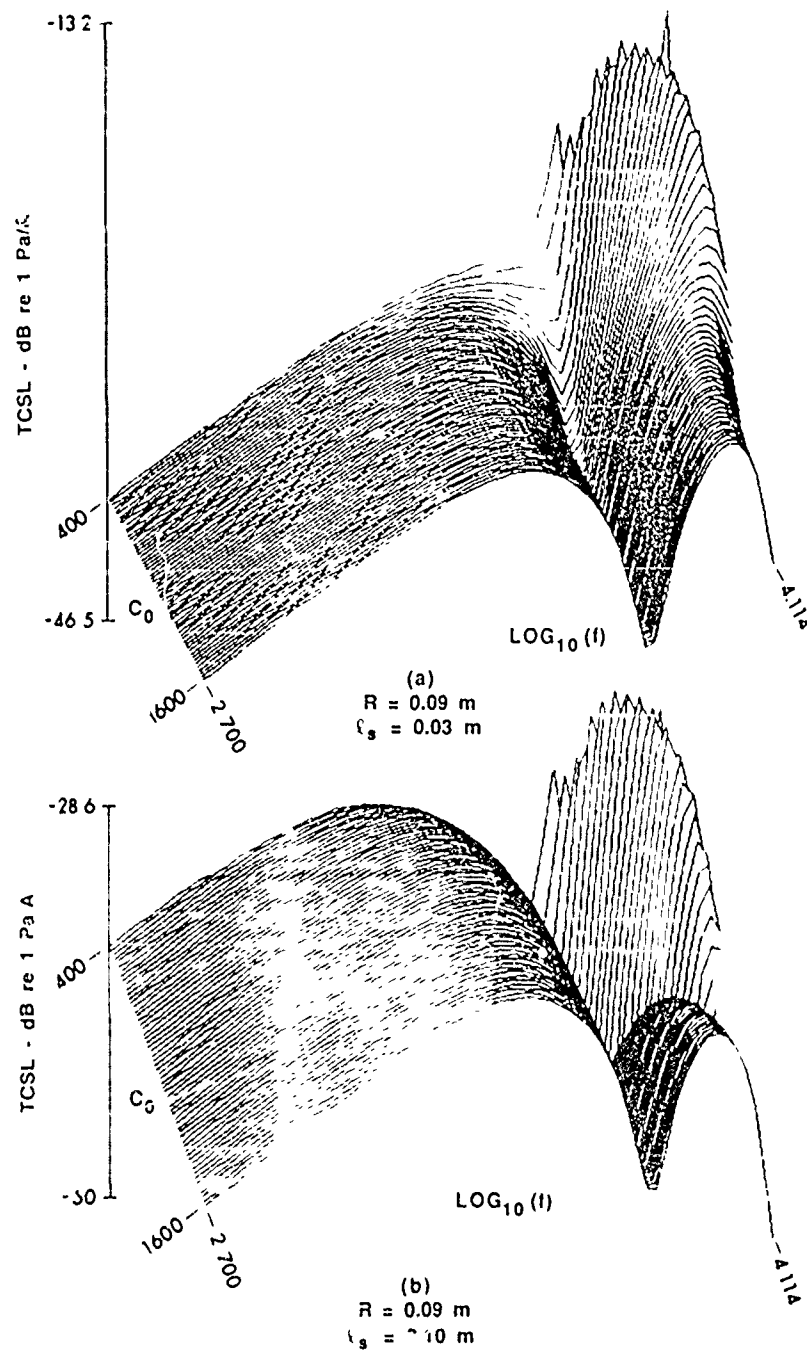


FIGURE 4.4
 TRANSMITTING CURRENT SENSITIVITY LEVEL
 AS A FUNCTION OF SOUND SPEED AND FREQUENCY

ARLUT
 AS 86 272
 SCS GA
 5 27 86

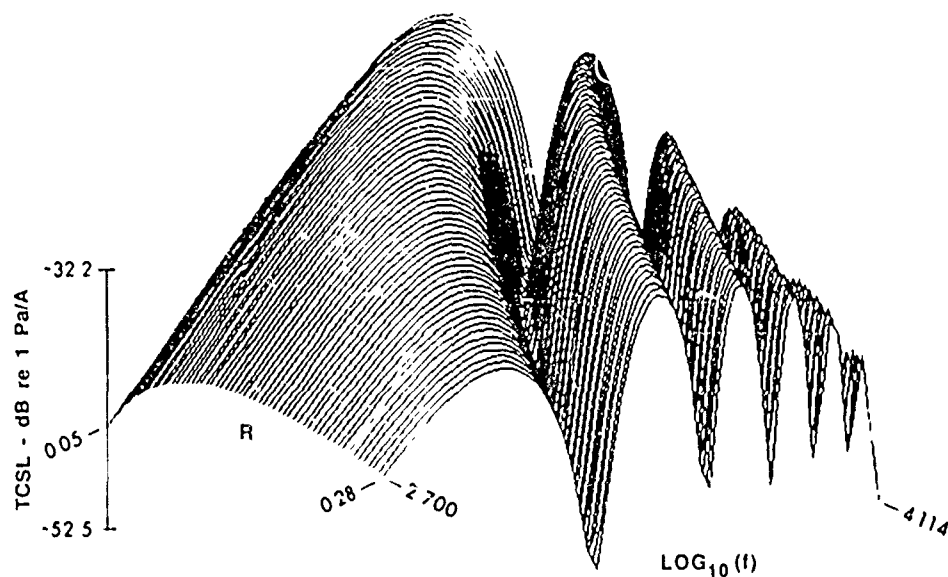
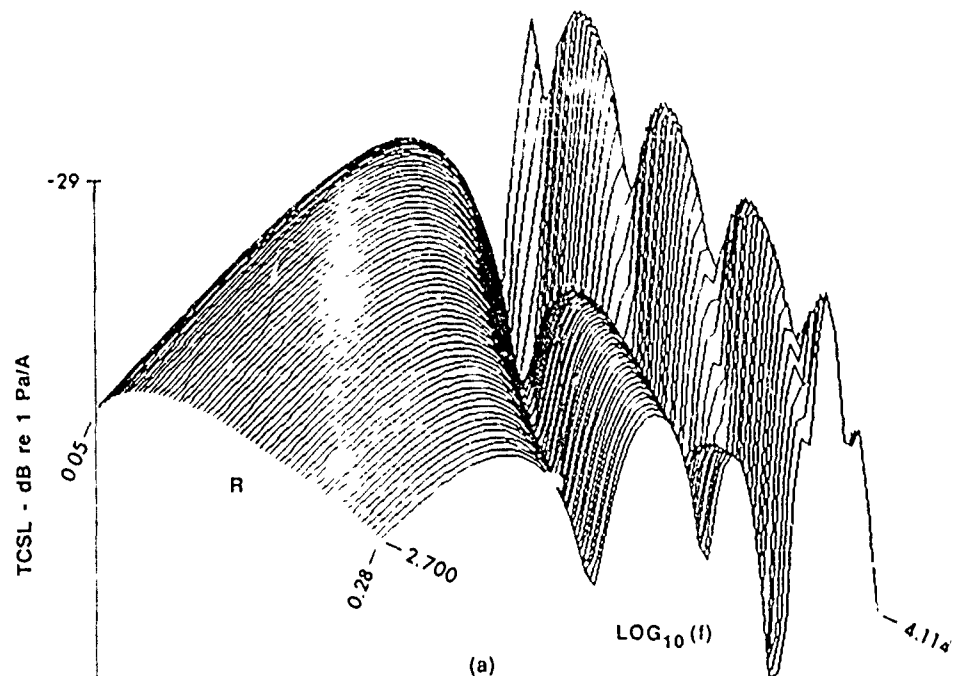
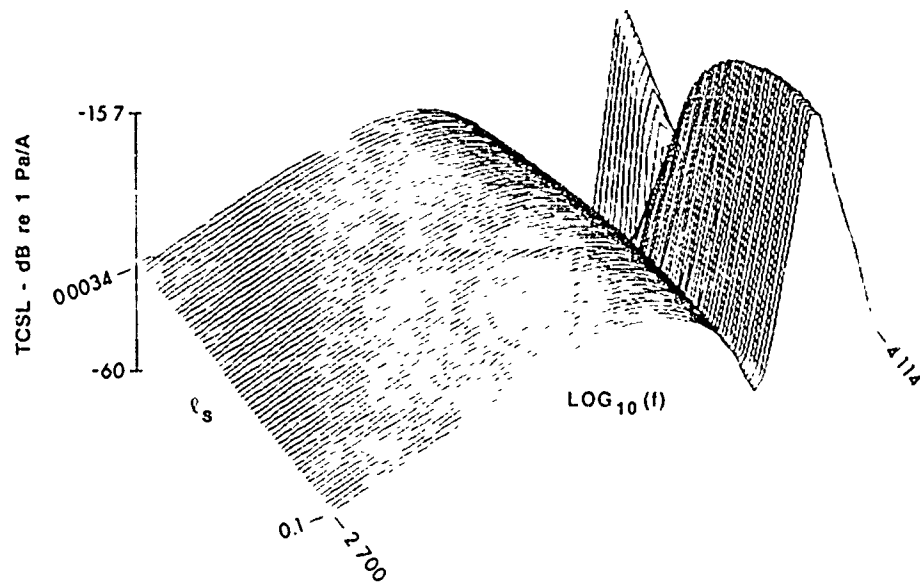
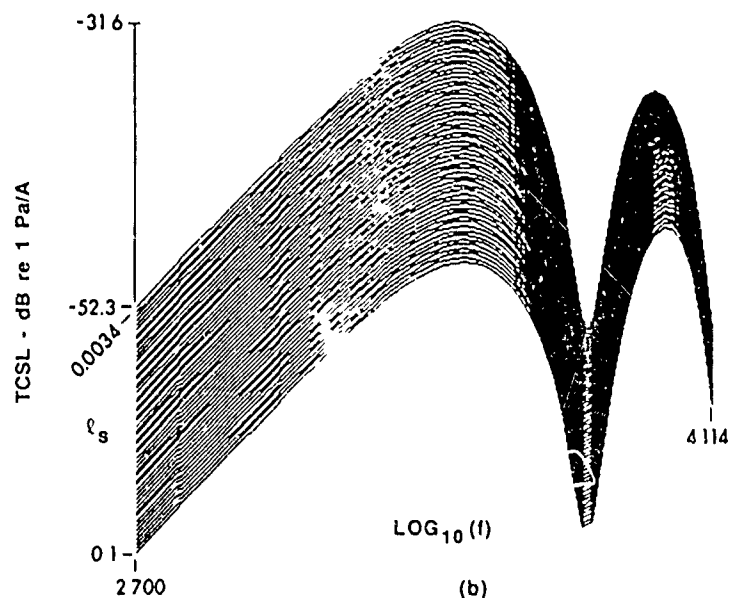


FIGURE 4.5
 TRANSMITTING CURRENT SENSITIVITY LEVEL
 AS A FUNCTION OF BAFFLE RADIUS AND FREQUENCY

ARL UT
 A3-86-273
 SCS GA
 5 27-86



(a)
 $C_0 = 650 \text{ m/s}$
 $R = 0.09 \text{ m}$



(b)
 $C_0 = 1536 \text{ m/s}$
 $R = 0.09 \text{ m}$

FIGURE 4.6
 TRANSMITTING CURRENT SENSITIVITY LEVEL
 AS A FUNCTION OF SOURCE LENGTH AND FREQUENCY

ARL UT
 AS-86-274
 SCS - GA
 5 - 27 - 85

figures, which indicates it is not a feature which is dependent on the sound speed in the waveguide. The half circumference of the baffle, which is the separation distance of the apertures, corresponds to $3/4$ of a wavelength at 6400 Hz with a free medium sound speed of 1500 m/s. Since the apertures radiate 180° out of phase for MHD sources centered symmetrically about the waveguide length, signal cancellation occurs at this wavelength.

The transmitting sensitivity as a function of baffle radius is shown in Figs. 4.5(a) and (b), where the periodicity of the nulls is seen to be a function of baffle radius for the reason given above.

Another important feature of the plots of Figs. 4.5(a) and (b) is that as the baffle radius decreases the overall sensitivity increases. The reason for this behavior is that the smaller baffle provides a smaller acoustic impedance, and thus a larger particle velocity at the aperture results. As the size of the baffle increases, the acoustic impedance increases and the particle velocity is diminished. Note that the increase in radiating efficiency resulting from increasing the baffle surface area does not increase the radiated pressure amplitude (sensitivity). When the baffle surface area is increased the aperture impedance increases and has the effect of decreasing the particle velocity faster than the improvement in the baffle reflecting property.

The higher peak amplitude in Fig. 4.4(a) relative to Fig. 4.4(b) is due to the achievement of the " $3/2$ wavelength" resonance at a lower frequency due to the slower sound speed in the waveguide.

Shown in Figs. 4.6(a) and (b) is the transmitting sensitivity as a function of the source length, $(b - a)$ or λ_s . Again it is lower sound speeds that cause the greater amplitudes at low frequencies. The effect of source length is not as strong for the higher sound speed plot in Fig. 4.5(b) since a resonance condition has not been reached. The primary effect in this case is the fixed radius of the baffle causing the resulting destructive interference null structure of the plot at the same frequency.

E. ELECTRICAL IMPEDANCE OF THE THERMOACOUSTIC TRANSDUCTION PROCESS

The electrolyte impedance characteristics and transmitting pressure sensitivity of the ohmic source are not linear relations, that is, the electrical current is not linearly related to the voltage and the transmitted pressure is not linearly related to the input voltage (or current). The nonlinearity of the ohmic mechanism is evident from the fact that an electrical input signal of a single frequency ω produces an acoustic output of frequency 2ω , as demonstrated in Chapter 3. The nonlinear behavior of the ohmic mechanism is evident in the source term of the inhomogeneous wave equation, $-\beta (\mathbf{J} \cdot \mathbf{J})_t / \sigma C_p$, where the dot product of the current density field with itself is a squaring or quadratic nonlinearity. One obvious consequence of this nonlinear behavior is that for multiple frequency inputs superposition of the single frequency Fourier transform solution does not hold. Therefore what was derived in Chapter 3 is valid for the single frequency input ω and not for linear combinations of this single frequency solution. It is important to note that the wave equation is linear, that is, the spectral content of the wave

fields produced by the nonlinear source do not undergo frequency domain corruption due to propagation. An acoustic signal at frequency ω generated by the MHD source mechanism will be propagated with frequency ω . Similarly a single frequency electrical input signal of frequency ω , through the ohmic mechanism, will generate a wavefield of 2ω , but the medium will transmit the signal uncorrupted at frequency 2ω . However, the boundary conditions are frequency dependent and therefore the wavefields are frequency "dependent", and thus the spectral content of the waves emitted by the source must be known in order to determine the wavefield.

Fortunately the source nonlinearity can be Fourier transformed by using convolution and thus the spectral output of the thermoacoustic source can be determined. If the current density has the functional form,

$$\mathbf{J}(\mathbf{x},t) = \mathbf{J}(\mathbf{x}) f(t) , \quad (4.23)$$

then the nonhomogeneous ohmic source term takes the form,

$$\frac{-\beta}{\sigma C_p} (\mathbf{J}(\mathbf{x}) \cdot \mathbf{J}(\mathbf{x})) f(t) f(t) , \quad (4.24)$$

where the dot product operation of the spatial component of \mathbf{J} was noted in Chapter 2. The Fourier transform can now be performed on $f(t) f(t)$ by convolution in the frequency domain as follows.

$$Q(\omega) = \mathcal{F}\{f(t) f(t)\} = \int_{-\infty}^{\infty} F(\omega') F(\omega - \omega') d\omega' , \quad (4.25)$$

where Q is the spectrum of the convolution, F is defined as

$$F(\omega) \equiv \mathcal{F}\{f(t)\} . \quad (4.26a)$$

and \mathcal{F} is the exponential Fourier transform operator defined as

$$\mathcal{F}\{f(t)\} \equiv \int_{-\infty}^{\infty} f(t) e^{j\omega t} dt. \quad (4.26b)$$

As a note, it should be kept in mind that when the multiplication of time harmonic functions is performed, $f(t) f(t)$, the $e^{j\omega t}$ "notation" must be replaced by the real-time functions such as $\cos(\omega t)$. The reason is simply that multiplication is a nonlinear operation and when it is performed on the complex time functions commonly used for notational ease incorrect or incomplete harmonic components are produced by the convolution operation. As an example of the convolution operation consider the following time dependence for J , assuming $\omega_1 > \omega_2$,

$$f(t) = A_1 \cos(\omega_1 t) + A_2 \cos(\omega_2 t). \quad (4.27)$$

The Fourier transform of Eq. (4.27) is

$$F(\omega) = A_1 (\delta(\omega + \omega_1) + \delta(\omega - \omega_1)) + A_2 (\delta(\omega + \omega_2) + \delta(\omega - \omega_2)). \quad (4.28)$$

The convolution results in the following source spectrum, Q ,

$$\begin{aligned} Q(\omega) = & A_1^2 (\delta(\omega + 2\omega_1) + \delta(\omega - 2\omega_1)) + A_2^2 (\delta(\omega + 2\omega_2) + \delta(\omega - 2\omega_2)) \\ & + 2A_1 A_2 (\delta(\omega + \omega_1 + \omega_2) + \delta(\omega - \omega_1 - \omega_2) + \delta(\omega + \omega_1 - \omega_2) + \delta(\omega - \omega_1 + \omega_2)), \end{aligned} \quad (4.29)$$

which indicates that the following wavefield harmonics are produced: $2\omega_1$, $\omega_1 + \omega_2$, $2\omega_2$, and $\omega_1 - \omega_2$.

Notice that the output of the simple two-frequency input is the generation of four different harmonics. For this two-frequency input the single

frequency solutions of Chapter 3 can now be written in terms of the above frequency components and the resultant pressure fields can be summed (since the acoustic equation is linear) to obtain the total acoustic field.

Due to the nonlinearity of the source mechanism, the linear impedance is not defined. What can be defined instead is the quadratic current transfer function (QCTF). The QCTF is defined as the ratio of the output current to the square of the input voltage for the input of two frequency components as follows.²⁴

$$\text{QCTF} \equiv \frac{i(\omega_A + \omega_B)}{V_A(\omega_A) V_B(\omega_B)} \quad (4.30)$$

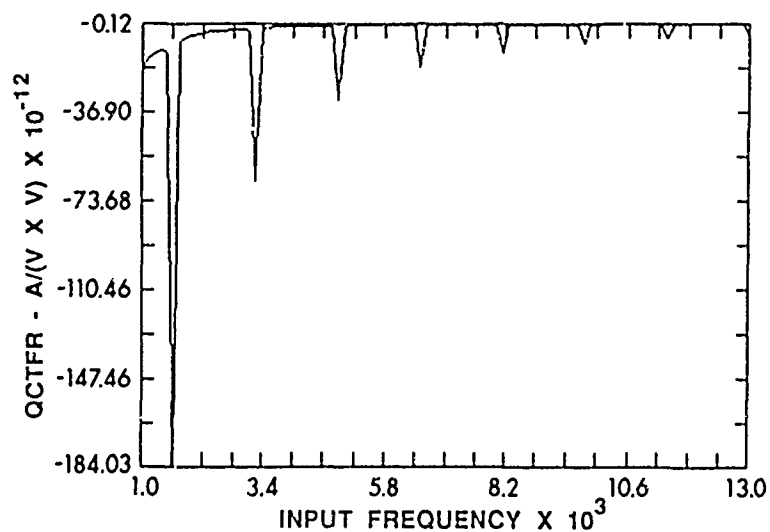
The expression for the ohmic source is as follows.

$$\text{QCTF} = \frac{\iint \sigma B_o u(\omega_A + \omega_B, x) dx dz}{\int E_A(\omega_A) dy \int E_B(\omega_B) dy} \quad (4.31)$$

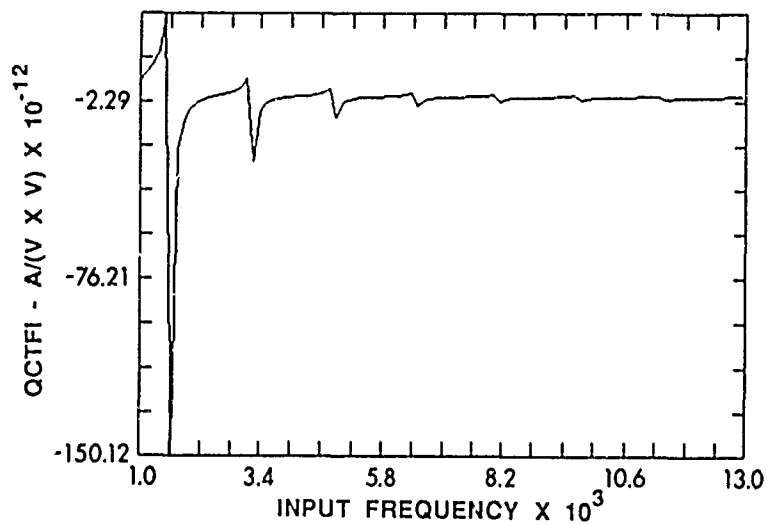
$$= \frac{-\beta B \sigma^2 \ell_z}{4 C_p \rho_o \ell_y^2} \frac{(R_{\ell}(e^{j2kb} + e^{j2ka} - 2e^{jk(a+b)}) + R_{\ell}(e^{-j2kb} - e^{-j2ka} + 2e^{-jk(a+b)}))}{k^2 (1 - R_{\ell} R_{\ell})} \quad (4.32)$$

where $k \equiv (\omega_A + \omega_B)/c_o$. As an example of the evaluation of Eq. (4.32), the QCTF for difference frequency, $\omega_1 - \omega_2$, would be found by substituting $\omega_A = \omega_1$ and $\omega_B = -\omega_2$ for the case of a single frequency input ω , $\omega_A = \omega$, and $\omega_B = \omega$.

The QCTF should be regarded as a term of second order for NaCl solutions, due to the combination of low thermal expansion, conductivity, and magnetic field. The QCTF for a 6% NaCl solution is shown in Fig. 4.7(a) and (b) for a single frequency input signal. The amplitudes of the plots are insignificant at any realistic voltage levels.



(a)
QUADRATIC CURRENT TRANSFER FUNCTION,
REAL COMPONENT (QCTFR)



(b)
QUADRATIC CURRENT TRANSFER FUNCTION,
IMAGINARY COMPONENT (QCTFI)

FIGURE 4.7
QUADRATIC CURRENT TRANSFER FUNCTION,
SINGLE FREQUENCY INPUT FOR 6% NaCl SOLUTION,
 $c_0 = 1500 \text{ m/s}$, $\ell = 0.10 \text{ m}$, $\ell_s = 0.10 \text{ m}$, $R = 0.09 \text{ m}$

ARL:UT
AS-86-431
SCS - GA
8 - 6 - 86

For liquids with a very high conductivity (such as mercury) the QCTF will not be of second order. Plots for mercury in the same waveguide configuration as the NaCl show much higher QCTF magnitudes (see Fig. 4.8(a) and (b)).

Since the QCTF is the current relationship the total complex current, i_T , (MHD and thermoacoustic effects) is

$$i_T = AV + \text{QCTF } V^2, \quad (4.33)$$

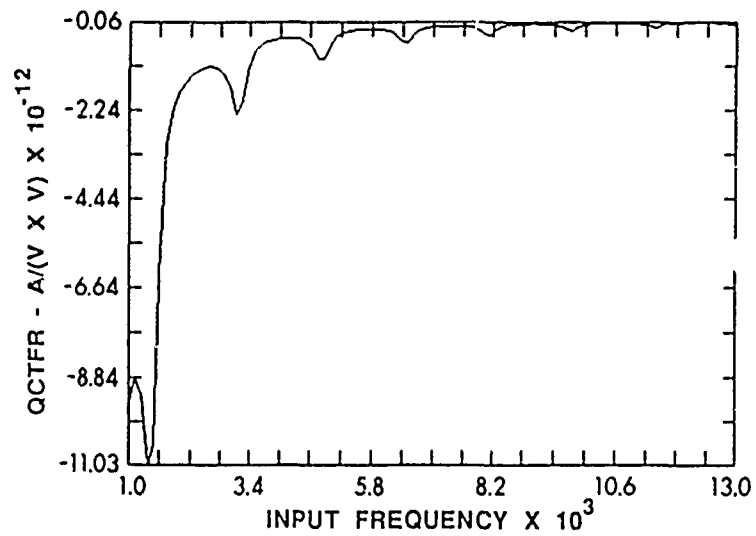
where A is the admittance due to the MHD mechanism and is equal to $1/Z$. The equivalent circuit of the combined MHD and thermoacoustic impedance including the polarization impedance is shown in Fig. 4.9.

F. THERMOACOUSTIC TRANSDUCTION PROCESS POWER EFFICIENCY

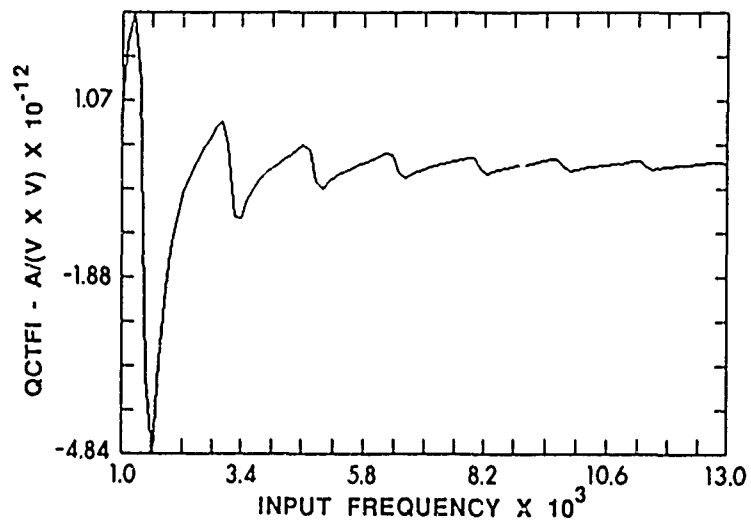
The thermoacoustic transduction power efficiency is defined as the radiated acoustic power due to the thermoacoustic mechanism divided by the real input electrical power to the MHD transducer. The complex input power is defined in Eq. (4.18), but if the QCTF is significant the effect needs to be accounted for in the electrical power expression. The total complex electrical power, W_{TH} , is then given by

$$W_{eTH} = V i_T. \quad (4.34)$$

The radiated acoustic power is defined using Eq. (4.20) with the particle velocity expressions of Eqs. (3.32a,c) being substituted, and the same expressions for the real component of the self-impedance being valid. With Eq. (4.20) and Eq. (4.34) the thermoacoustic process efficiency can be defined as



(a)
QUADRATIC CURRENT TRANSFER FUNCTION,
REAL COMPONENT (QCTFR)



(b)
QUADRATIC CURRENT TRANSFER FUNCTION,
IMAGINARY COMPONENT (QCTFI)

FIGURE 4.8
QUADRATIC CURRENT TRANSFER FUNCTION,
SINGLE FREQUENCY INPUT FOR MERCURY,
 $\ell = 0.10$ m, $\ell_s = 0.10$ m, $R = 0.09$ m

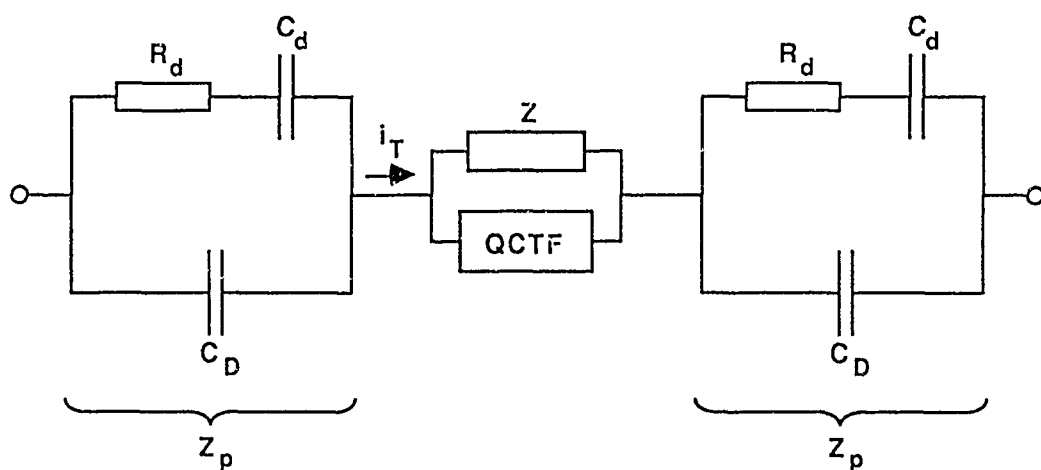


FIGURE 4.9
EQUIVALENT CIRCUIT OF THE COMBINED MHD
AND THERMOACOUSTIC INPUT IMPEDANCE

$$\eta_{TH} = \frac{W_A}{\text{Re}(W_{eTH})} \quad (4.35)$$

Plots of the thermoacoustic transduction process efficiency are given in Fig. 4.10(a) and (b) for a 6% NaCl-water solution and mercury, respectively. Comparing the MHD efficiencies given in Figs. 4.3(a) and (b) to the thermoacoustic efficiencies in Fig. 4.10(a) and (b) the MHD process is much more efficient for both fluids.

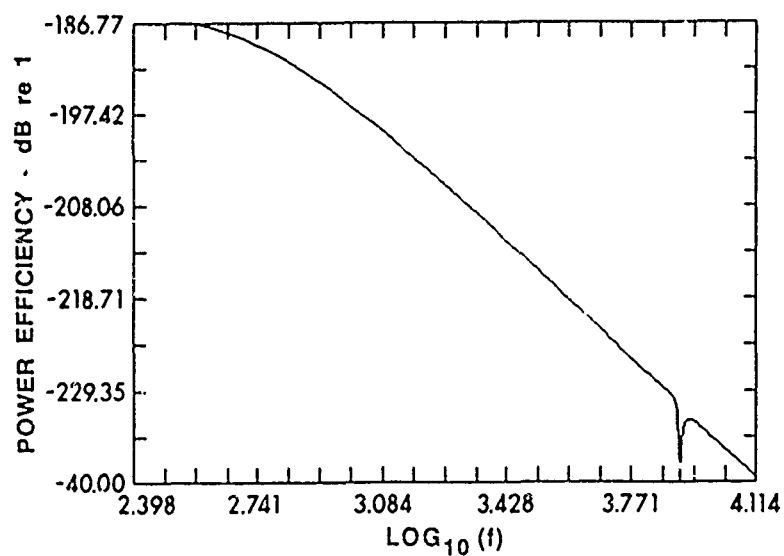
A rough relationship between the fluid properties of the medium and the thermoacoustic process efficiency is obtained from the leading coefficients of the ratio of acoustic power expression Eq. (4.20) to the expression for the real dc ohmic power dissipation (the primary mechanism of power dissipation in the experimental transducer),

$$\eta_{TH} \propto \left(\frac{J \sigma}{\omega C_p} \right)^2 \frac{c_o^3}{\sigma \rho \ell_s} \quad (4.36)$$

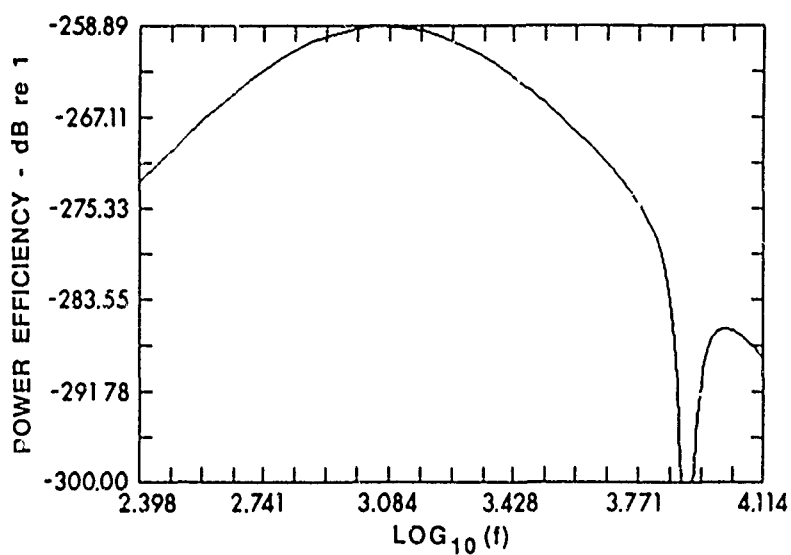
The same type of expression can be written for the MHD process and is stated as

$$\eta_{MHD} \equiv \left(\frac{B}{\omega} \right)^2 \frac{\sigma c_o}{\rho \ell_s} \quad (4.37)$$

Some interesting insights are gained by these two equations. First, the thermoacoustic efficiency is a function of the current density squared, or power, and thus makes comparison of efficiencies a matter of first stating the current density. Second a low conductivity, mass density, specific heat, and high coefficient of thermal expansion are desirable for an



(a)
6% NaCl WATER SOLUTION $c_0 = 1600$ m/s



(b)
MERCURY

FIGURE 4.10
THERMOACOUSTIC TRANSDUCTION
PROCESS EFFICIENCY
 $\ell = 0.10$ m, $\ell_s = 0.10$ m, $R = 0.09$ m

efficient thermoacoustic source. For the MHD source the opposite is true with regard to the conductivity; a high value is desired, so that little ohmic losses are generated. As the plots in Fig. 4.3(a) and (b) show, mercury is a more efficient fluid for the MHD process than the NaCl solution by a factor of 60 dB, due to mercury's 1.0×10^6 1/(ohm m) conductivity versus the 5.26 1/(ohm m) conductivity of the NaCl solution. The opposite is of course true for the thermoacoustic case where the NaCl solution is approximately 70 dB more efficient. However, mercury does have a value of C_p of 140 J/kg/C versus 4100 J/kg/C for the NaCl solution, but the mass density of mercury is 13600 kg/m³ versus 1041 for the NaCl water solution.

G. TRANSMITTING SENSITIVITY OF THE THERMOACOUSTIC PROCESS

The transmitting sensitivity of a transducer is a transfer function, like the admittance or impedance, and is generally defined in the frequency domain for a single input frequency assuming that the same output frequency is produced. The transmitting sensitivities of the thermoacoustic mechanism cannot be defined using the single frequency definition since the thermal source mechanism is nonlinear and produces spectral pressure signal components different from the input electrical signal. A quadratic transfer function will be defined for two input frequencies as the quadratic voltage transmitting sensitivity (QVTS),

$$QVTS \equiv \frac{p_{if}(\omega_A + \omega_B, r = 1 \text{ meter}, \psi = \text{main beam axis})}{V_A(\omega_A) V_B(\omega_B)}, \quad (4.38)$$

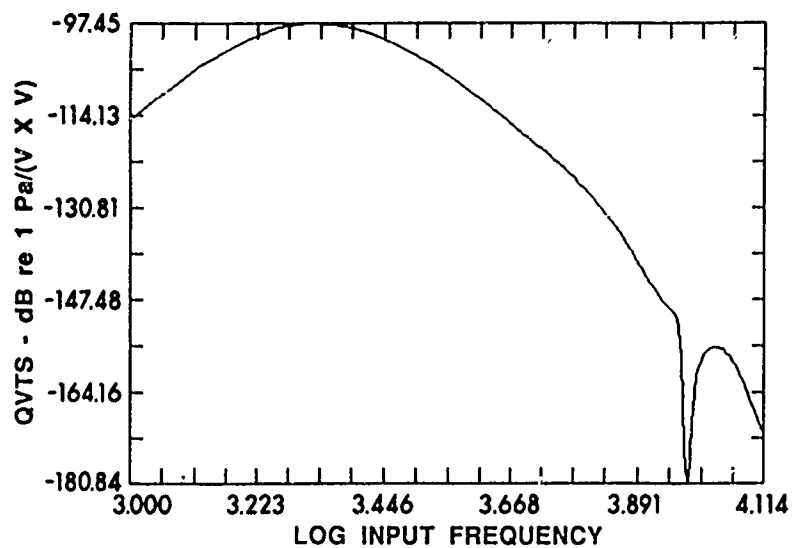
where $V_A(\omega_A)$ and $V_B(\omega_B)$ are the Fourier transformed expressions for the

voltage amplitudes at ω_A and ω_B . Substituting Eq. (B.4) for p_{ff} , Eq. (3.32b) for the particle velocity distribution, and Eq. (4.1) for the potential V into Eq. (4.38), the analytical expression for the QTVS results,

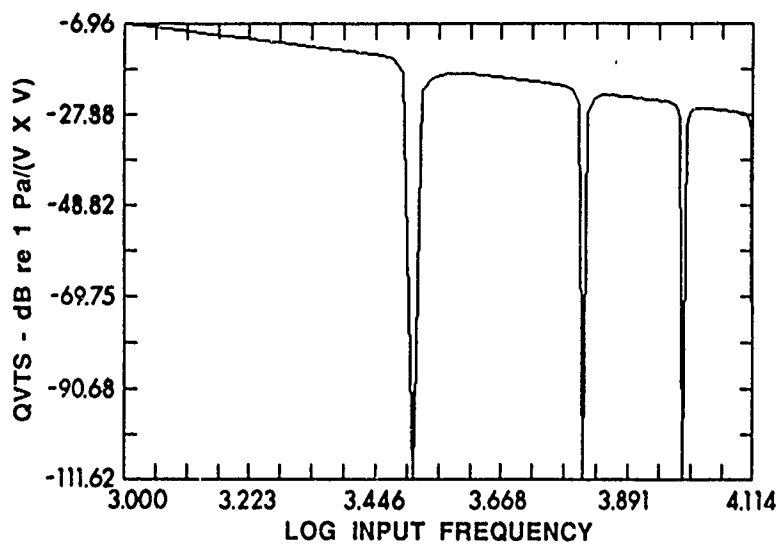
$$\begin{aligned}
 QVTS = & \frac{B_o \sigma \rho_{fm} c_{fm}}{4C_p \rho_o k_{fm} \ell_y^2} \\
 & \left\{ \frac{((e^{jka} - e^{jkb}) - R_{\ell} (e^{-jka} - e^{-jkb})) (e^{jk\ell} - R_{\ell} e^{-jk\ell})}{2k(1 - R_{\ell} R_{-\ell})} \right. \\
 & \sum_{n=0}^{\infty} \frac{(P_{n-1}(\cos\Theta) - P_{n+1}(\cos\Theta)) P_n(-\cos\psi) e^{-j\pi(n+1)/2}}{\left. \frac{d}{dx} h_n^1(x) \right|_{x=k_{fm} R}} \\
 & + \frac{((e^{-jka} - e^{-jkb}) - R_{\ell} (e^{jka} - e^{jkb})) (e^{jk\ell} - R_{\ell} e^{-jk\ell})}{2k(1 - R_{\ell} R_{-\ell})} \\
 & \left. \sum_{n=0}^{\infty} \frac{(P_{n-1}(\cos\Theta) - P_{n+1}(\cos\Theta)) P_n(\cos\psi) e^{-j\pi(n+1)/2}}{\left. \frac{d}{dx} h_n^1(x) \right|_{x=k_{fm} R}} \right\} \quad (4.39)
 \end{aligned}$$

where $k_{fm} = (\omega_A + \omega_B)/c_{fm}$ and $k = (\omega_A + \omega_B)/c_o$; for a single frequency input ω , $k_{fm} = 2\omega/c_{fm}$ and $k = 2\omega/c_o$.

Time did not permit a parameter investigation such as that performed for the the MHD sensitivity. However, two plots of the single frequency input thermoacoustic transmitting sensitivities (QVTS) for fixed parameters are given in Fig. 4.11(a) and (b) for the 6% NaCl solution and mercury. Notice that the mercury transducer shows a higher sensitivity than the NaCl solution. However, the sensitivity is in terms of the input voltage.



(a)
6% NaCl SOLUTION, $c_0 = 1600$ m/s,
 $\ell = 0.10$ m, $\ell_s = 0.10$ m, $R = 0.05$ m



(b)
MERCURY, $\ell = 0.10$ m,
 $\ell_s = 0.10$ m, $R = 0.09$ m, $c_0 = 1450$ m/s

FIGURE 4.11
QUADRATIC VOLTAGE TRANSMITTING
SENSITIVITY, SINGLE FREQUENCY INPUT (QVTS)

With mercury's very high conductivity a very small voltage is always going to result, at the terminals, and thus a low source level. This is because generating large voltages on a practical thermoacoustic mercury transducer is tantamount to huge electrical currents due to the low real input impedance.

More discussion of the QVTS is included in Chapter 5 with the experimental results.

CHAPTER 5

TRANSMITTING EXPERIMENT

To verify the theoretical predictions presented in Chapters 2, 3, and 4, an MHD transmitter was constructed and sensitivity and beam pattern measurements were taken. The transducer used in the experiments is depicted in the photograph of Fig. 5.1.

The planned operating regime of the the MHD transmitter with respect to the frequency bandwidth and output level was primarily dictated by the characteristics of the power amplifier that was available and the spatial extent of the magnetic field that could be generated. Fortunately a high power, relatively broadband power amplifier was available at ARL:UT. The magnetic field was generated using samarium-cobalt permanent magnets. Permanent magnets were employed primarily because of the convenience of not needing a power supply, but due to the expense of the magnets a limited volume of low permeable space could be energized uniformly. An important consideration was that the permanent magnet be relatively compact and of simple design since the size of the transducer has an important effect on the acoustic radiating characteristics.

A. OPTIMIZATION OF THE MHD TRANSMITTING CURRENT SENSITIVITY

The prime objective in designing the MHD transducer was to maximize the transmitting sensitivity across a broad frequency bandwidth. Tantamount to this objective is determining the waveguide dimensions, the permanent magnet spatial distribution, and the electrode surface distribution.

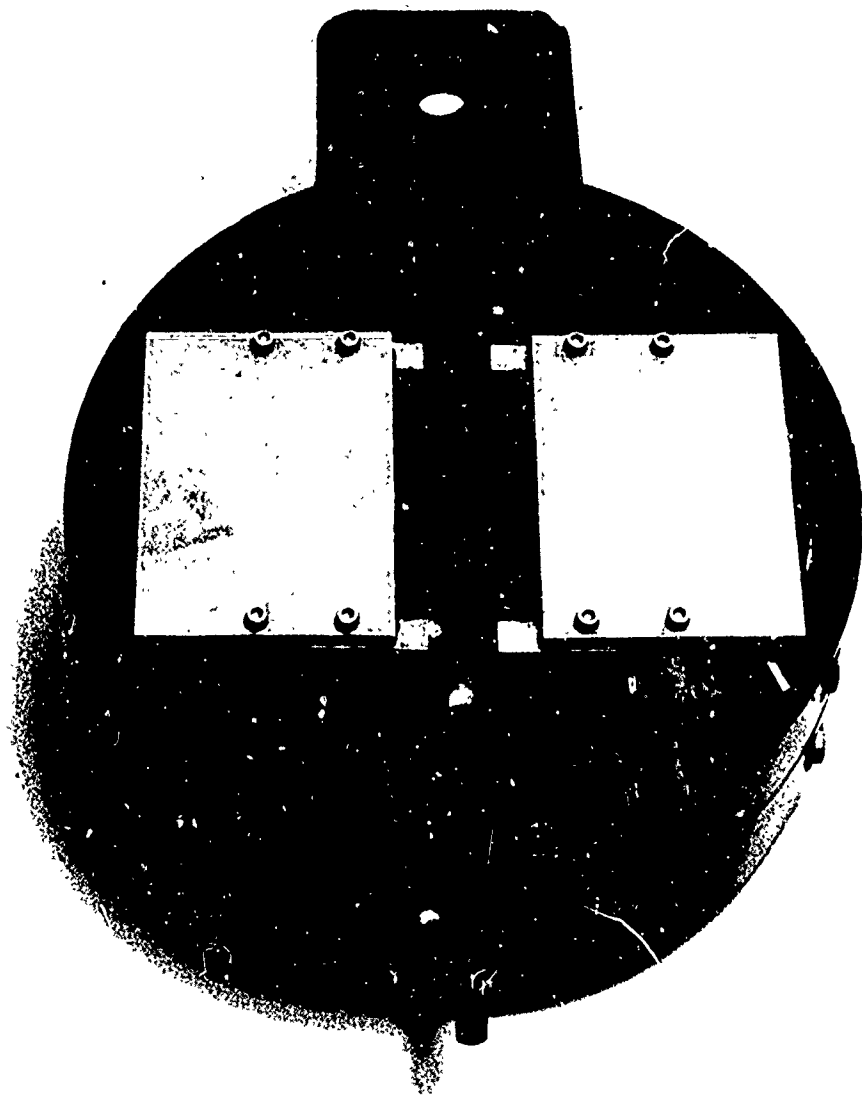


FIGURE 5.1
MAGNETOHYDRODYNAMIC TRANSDUCER
APERTURE VIEW

From the transmitting current sensitivity expression, Eq. (4.22b), it is obvious that a large magnetic induction is desirable, but maximizing the magnetic induction does not optimize the design goal using permanent magnets. Since the radiating aperture area is an important parameter, it would seem that a large aperture together with a high magnetic field would contribute to maximizing the sensitivity. However, the size of the aperture is directly related to the pole face separation of the magnets, and therefore increasing the aperture area increases the reluctance of the magnetic circuit. There is a definite optimization of the magnetic induction by the aperture size which will maximize the transmitting sensitivity for a given quantity and spatial arrangement of permanent magnets.

The functional dependence of the sensitivity on the aperture radius and baffle radius is not explicit in Eq. (4.14b); the dependence arises in the computation of the reflection coefficients. The relationship between sensitivity and aperture size is displayed in Fig. 5.2 for a spherical baffle radius of 0.05 m and frequency of 1000 Hz. The sensitivity function, for the purpose of the optimization, is well fit by a linear relation in the region from 0 to 29 mm (the general trend is for the sensitivity to increase over the entire frequency band as seen in Fig. 5.3). At 1000 Hz and for a baffle of radius 0.05 m the relation is

$$TCS \propto 727.3 R_a , \quad (5.1)$$

where R_a has the units of meters.

It is also necessary to relate the magnetic induction to the aperture radius by the appropriate magnetic circuit model. The analysis of

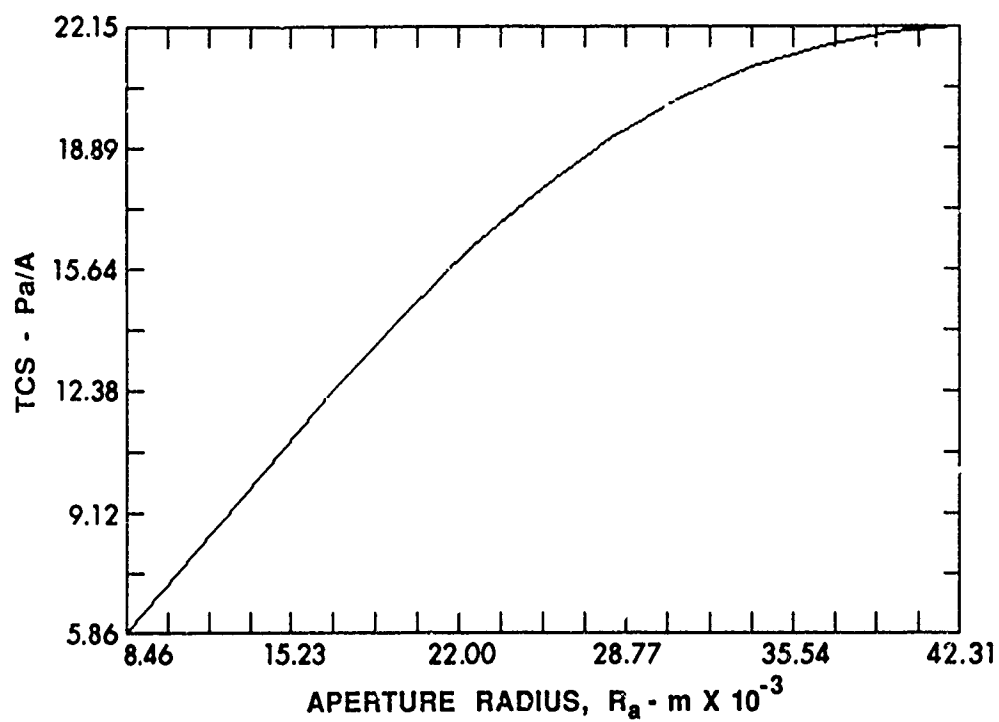


FIGURE 5.2
TRANSMITTING CURRENT SENSITIVITY AS A
FUNCTION OF APERTURE RADIUS, FOR
 $c_0 = 1550$ m/s, $R = 0.05$ m, $B = 1$ T, $f = 1000$ Hz

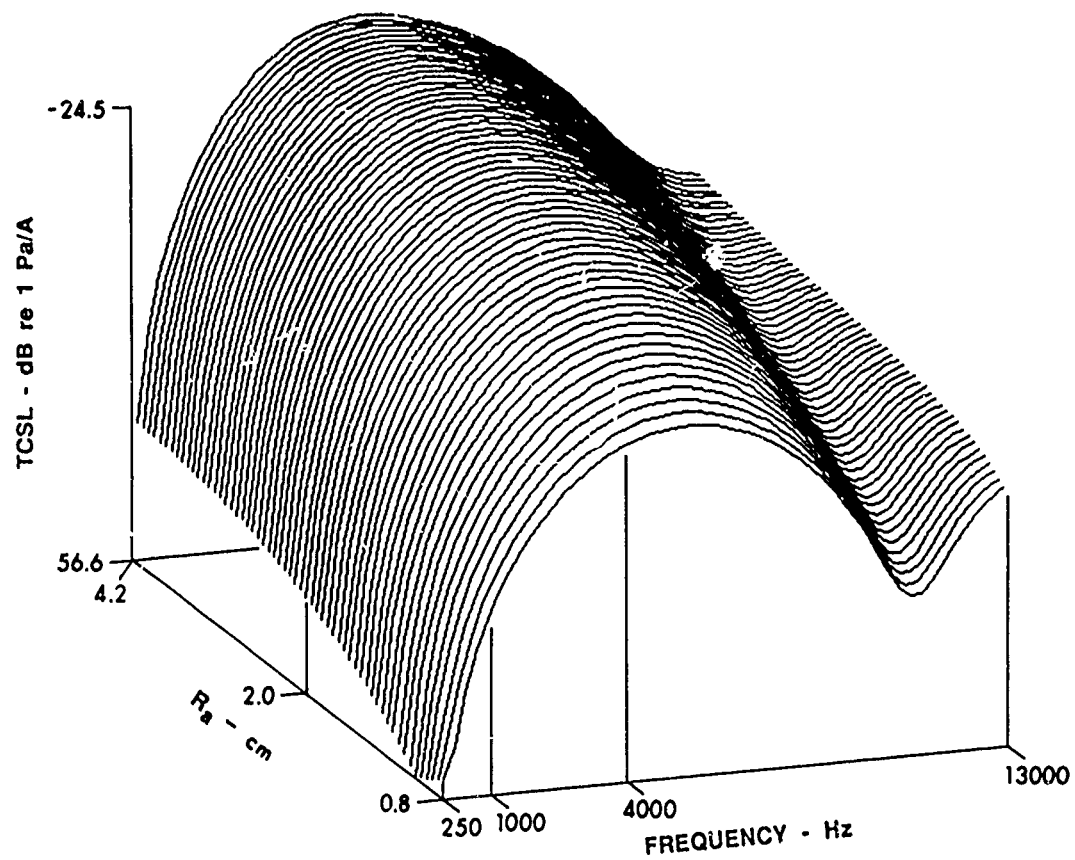


FIGURE 5.3
TRANSMITTING CURRENT SENSITIVITY LEVEL (TCSL)
AS A FUNCTION OF APERTURE RADIUS AND FREQUENCY, FOR
 $c_0 = 1550$ m/s, $R = 0.05$ m, $B = 1$ T

ARL:UT
AS-86-442
SCS - GA
8-6-86

the magnetic circuit follows from Cousins and Nash²⁵ (they constructed a cloud chamber using permanent magnets). The important technical aspect of their work is the development of an empirical relation for the magnetic flux leakage (fringing losses) associated with square or rectangular magnetic pole faces with various geometric restrictions. Due to the manufactured shape of the permanent magnets a limited number of practical geometric configurations were possible. Since the research budget allowed the purchase of 40 magnets of dimensions 2" x 2" x 0.5" an arrangement of four stacks of five magnetics above and below the field gap was intuitively obvious. This was not, however, an ad hoc choice; the circuit model predicted that larger but fewer stacks would result in large fringing losses. Therefore, given the four-stack arrangement, the relationship between the magnetic induction and aperture radius was found to be

$$B = -15350 R_a + 8250, \quad (5.2)$$

where the units of B are tesla. The computer generated curve is shown in Fig. 5.4.

Stated previously, the sensitivity is directly proportional to B, so Eq. (5.1) and Eq. (5.2) can be combined to yield an empirical relation for the TCS as a function of R_a ,

$$TCS \propto (-15.35 R_a + 0.8250) 1.106 R_a. \quad (5.3)$$

To maximize the relationship in Eq. (5.3) the expression is differentiated with respect to R_a and the result set equal to zero. The value for R_a is found to be 0.027 m, which is a field gap, l_z , of 0.0479 m. Due to an error in the

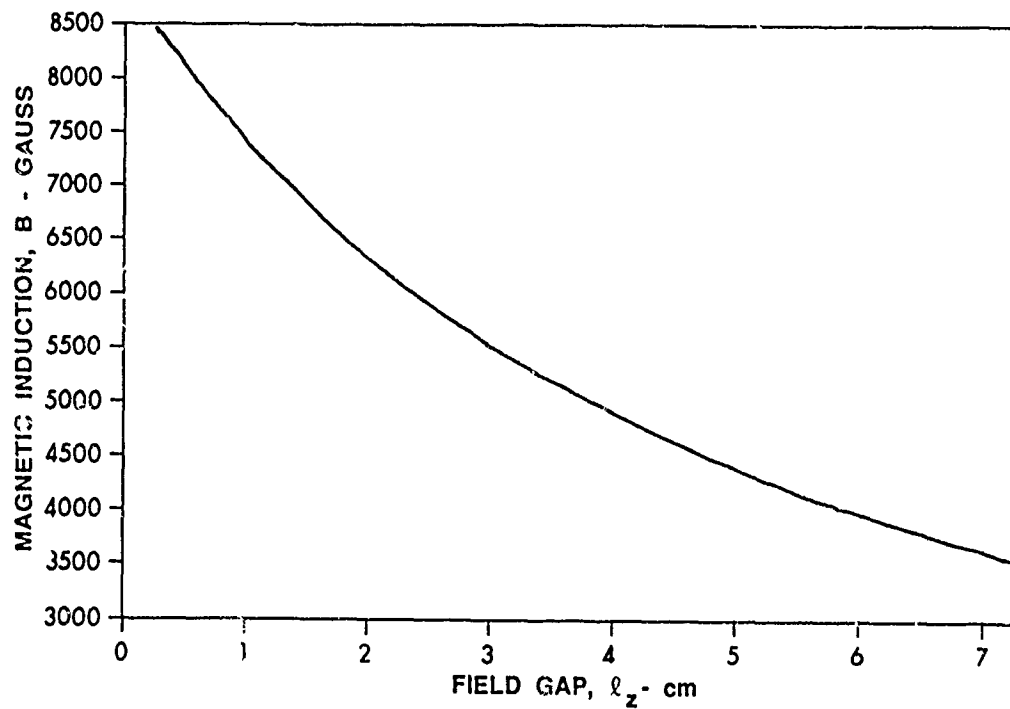


FIGURE 5.4
MAGNETIC INDUCTION AS A FUNCTION OF THE
TRANSVERSE WAVEGUIDE DIMENSION l_z (FIELD GAP)

ARL:UT
AS-86-435
SCS - GA
8-6-86

calculations made at the time the MHD transducer was designed a value of 0.0381 was used for the field gap. The construction details of the waveguide are shown in Fig. 5.5.

The estimate of the magnetic induction for the 0.0479 m field gap is 4500 G and maximum measured value for the 0.0381 m gap, displayed in the distribution shown in Fig. 5.6, is 4327 G. It was concluded that either the assumptions concerning the geometrical restrictions on the validity of the fringing theory are in slight violation, or small gaps in the transducer magnet stack raised the circuit reluctance higher than expected. However, the magnetic induction is very uniform as shown in Fig 5.6 for the distribution measured at the midpoint plane of the waveguide.

B. ACOUSTIC SPEED MEASUREMENT OF THE WAVEGUIDE

The phase or plane wave acoustic speed for the 6% NaCl-water solution in the MHD waveguide was measured to confirm the boundary condition assumption that the waveguide walls were acoustically rigid. Two methods were used to measure the wave speed, (1) a pulse and (2) a resonance technique.

The pulse technique used a transmit frequency of 150 kHz and a time duration of three cycles or 10 μ s. This method yielded a wave speed of 1550 m/s.

The resonance method employed a continuous wave white noise signal transmitted into the waveguide with the apertures terminated by "rigid" brass blocks. The boundary conditions were thus taken to be rigid walled

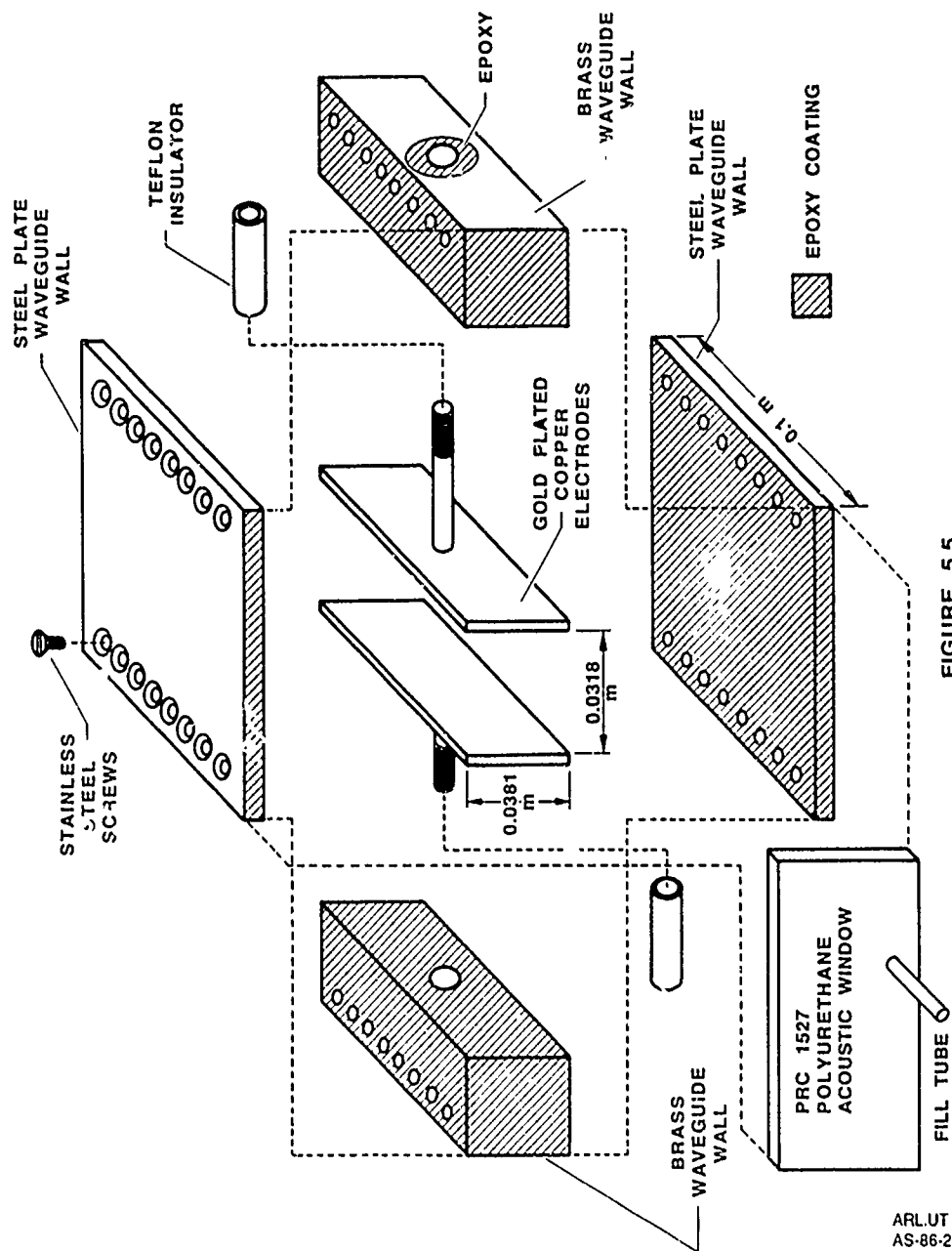


FIGURE 5.5
MAGNETOHYDRODYNAMIC TRANSDUCER
WAVEGUIDE CONSTRUCTION DETAILS

ARL:UT
AS-86-267
SCS-GA
5-27-86

4327	4327	4327
3571	3571	3571
4152	4152	4152

APERTURE DISTRIBUTION

4082	4082	4082
4082	4082	4123
4082	4082	4082

MIDPOINT OF WAVEGUIDE
DISTRIBUTION

FIGURE 5.6
MEASURED MAGNETIC INDUCTION LEVELS (GAUSS)
IN THE MHD TRANSDUCER WAVEGUIDE

cavity (see Fig. 5.7). By measuring the amplitude spectrum of the cavity response to the white noise signal the frequencies of the standing wave modes were determined and used to calculate the wave speed. From the 1,0,0 pressure mode of the cavity the wave speed was calculated to be 1600 m/s. For most of the theoretical calculations 1600 m/s was used because the sound speed was determined by the resonance method at 7500 Hz, which is within the frequency band of the experiment. The theoretical sound speed for the 6% NaCl-water solution at 20° C was calculated to be 1536 m/s by using of the equation given by Coppens²⁶ for the speed of sound in seawater as a function of salinity and temperature.

C. MEASUREMENT OF THE ELECTRICAL IMPEDANCE OF THE TRANSDUCER

The input impedance of the MHD transducer was measured using the system of Fig. 5.8 with the transducer in the water. The input signal to the transducer was white noise at an rms amplitude of 20 V and the current was sensed using a Pearson current transformer. The transfer function mode of the signal analyzer was used to determine the impedance using the voltage as the response signal to the input current signal. The transfer function is calculated as the crosscorrelation between the input and output complex signal spectra divided by the autocorrelation of the complex input signal spectrum. A plot of the magnitude and phase of the impedance measurement is shown in Fig. 5.9.

The measured impedance indicates, by the lagging phase, a significant capacitive impedance at frequencies less than 4000 Hz. This capacitive effect is due to the polarization impedance of the electrodes,

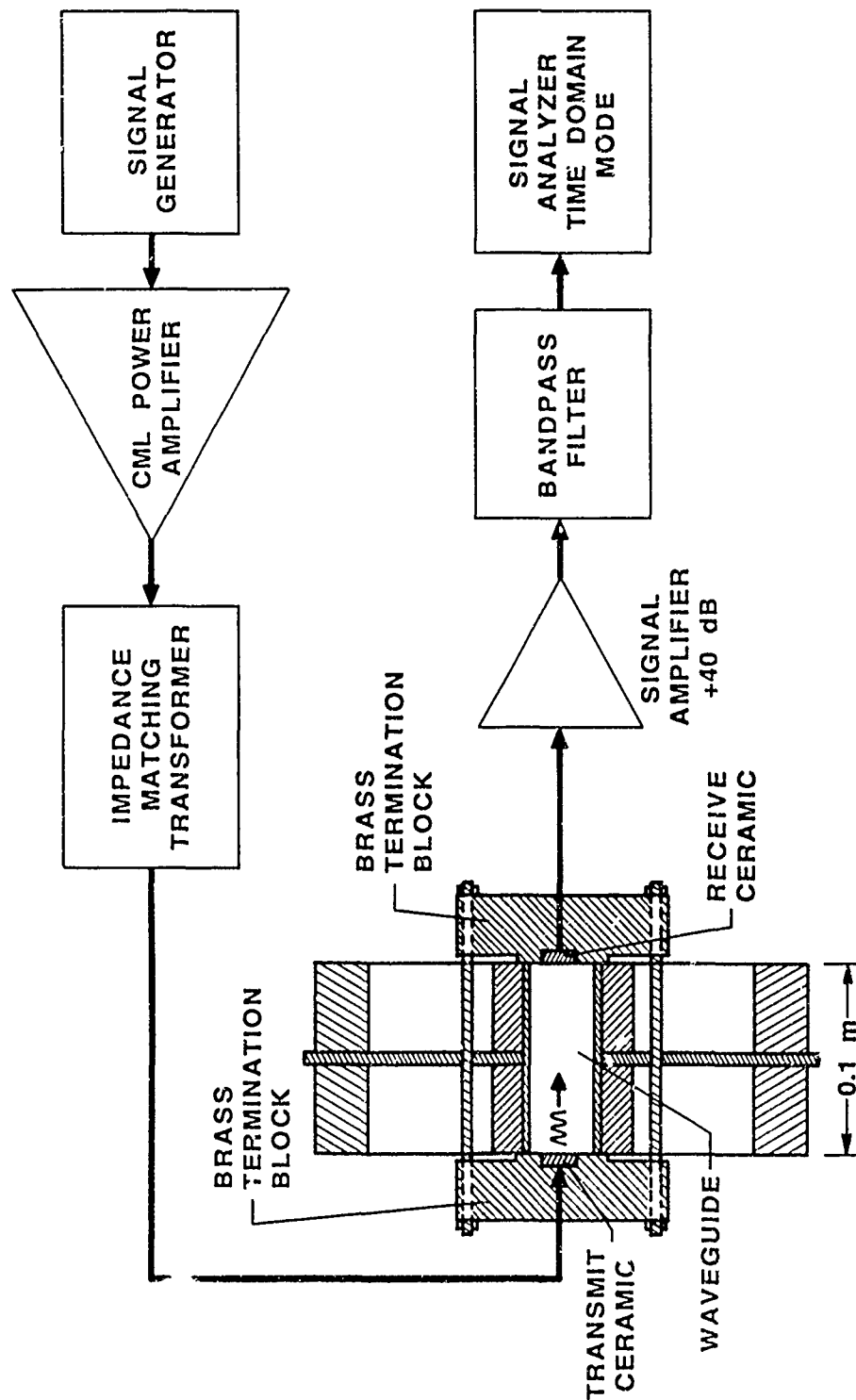


FIGURE 5.7
PHASE SPEED MEASUREMENT SYSTEM

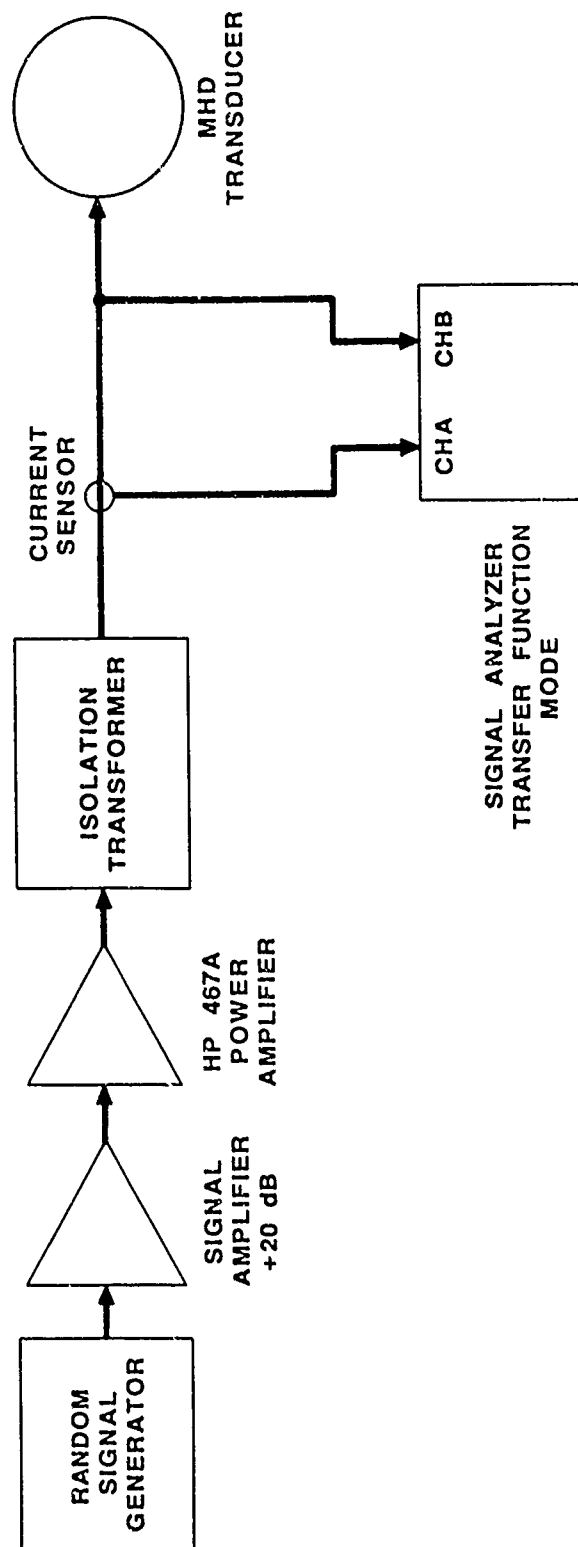


FIGURE 5.8
BLOCK DIAGRAM OF TRANSDUCER ELECTRICAL
IMPEDANCE MEASUREMENT SYSTEM

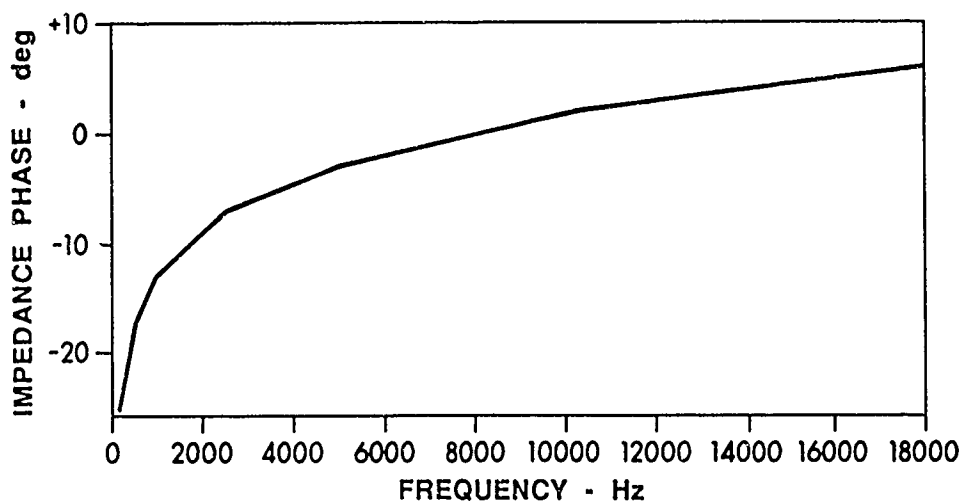
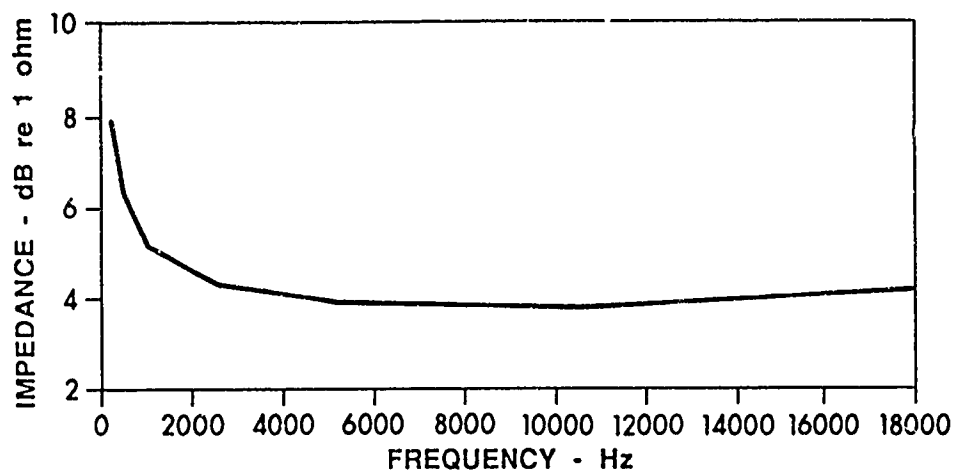


FIGURE 5.9
MEASURED INPUT ELECTRICAL IMPEDANCE OF THE MHD
TRANSDUCER CONTAINING A 6% NaCl-H₂O SOLUTION

which was investigated theoretically in Section A of Chapter 4. Plotted in Fig. 5.10 are the real and imaginary components of the theoretical impedance represented by the network shown in Fig 4.1 with data points taken from Figs. 5.9. Notice the ordinate axis is the reciprocal of the square root of the angular frequency so that the linear dependence of the diffusional impedance on $1/\sqrt{\omega}$ can be exhibited (see Eqs. (4.11) and (4.12)). One can clearly see the linear trend in the data at low frequencies. It is also noted that the best fit of the theoretical curves occurred for a double layer capacitance value of $762 \mu\text{s}$ which is 200 mF/m^2 , and an electrolyte conductivity of 5.56 1/ohm m , which is a dc resistance of 1.5 ohms , was included in the calculation of Z (Eq. (4.17)). The imaginary component of the MHD impedance was found to have a negligible effect on the input impedance model and can therefore be discarded in most preliminary calculations using a low conductivity fluid.

It is concluded that the polarization impedance model fits the data well; however, the model would become extremely difficult to apply if electrolytes other than 1,1 valent salts are used. This might be the case with seawater. Vetter gives a very complete discussion on the impedance properties of other common electrolyte chemistries² and some of the difficulties of complex chemistries.

D. TRANSMITTING CIRCUIT AND ACOUSTIC SIGNAL MEASUREMENT SYSTEM

The efficiency of both the MHD and thermoacoustic mechanism is extremely low in the case of low conductivity fluids as evidenced by Fig. 4.3b. As stated previously the efficiency is better at low frequency

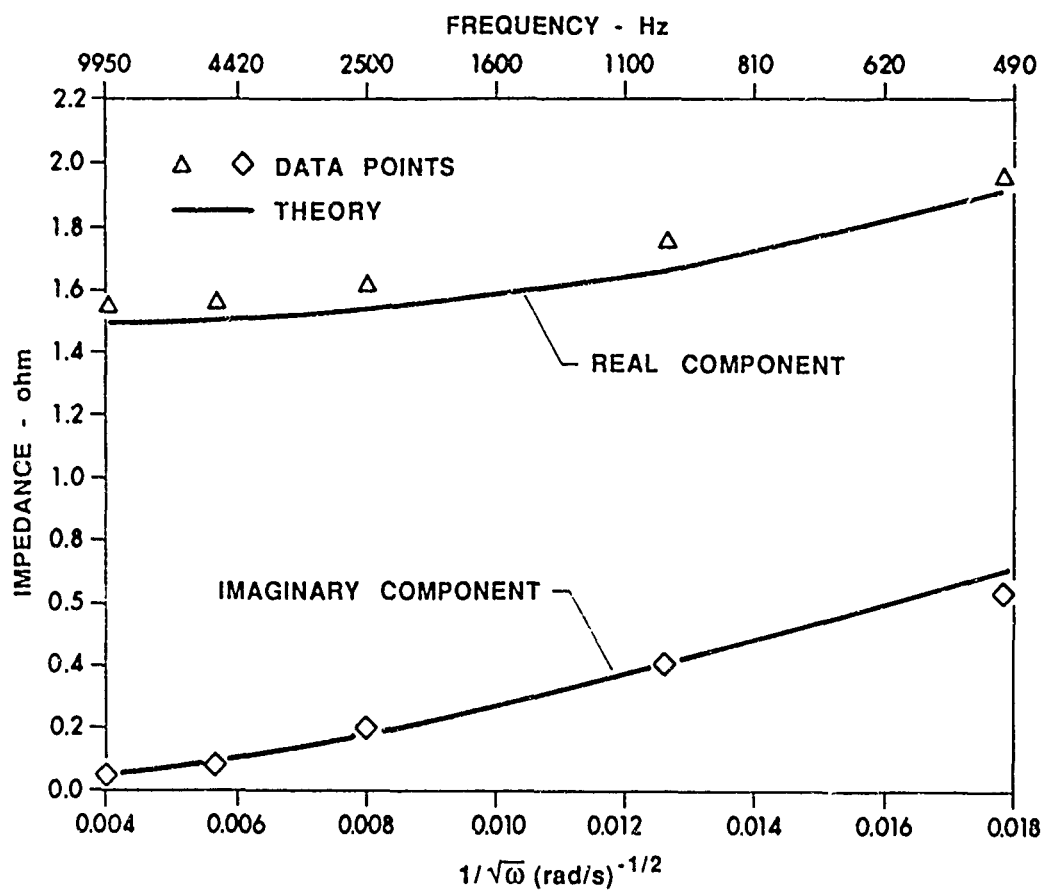


FIGURE 5.10
THEORETICAL AND MEASURED ELECTRICAL INPUT
IMPEDANCE OF THE MHD TRANSDUCER

since the particle velocity is larger. However an efficiency of -108 dB implies that an input of 5 kW of electrical power will produce only 20 mW of radiated acoustic power. The problem of performing the experiment is whether the signal-to-noise ratio (S/N) is sufficient to produce meaningful data.

The power amplifier used to power the transducer was a CML Corp. model B5K which can deliver 5000 V-A loaded with power factors between 1 and 0.1 over the band from 100 to 10000 Hz, ± 0.5 dB. Since the maximum lag in the phase of the impedance is -25° (Fig. 5.11), which corresponds to a power factor of 0.91, the compensation of the transducer was not deemed necessary. The block diagram of the transducer circuit is shown in Fig. 5.11.

An impedance matching transformer was therefore designed to match the dc resistance of 1.5 ohms of the transducer to the amplifier. The transformer turns ratio is 1.43, with 38.6 turns on the primary and 30.6 turns on the secondary. The matching transformer has a 2 mil silicon steel laminate core capable of broadband power transfer with a maximum hysteresis loss of 10 W at 400 Hz. The total loss of the transmission lines and transformer was measured at 300 W. For all the transmitting experiments the transducer current was typically 60 A peak with a terminal voltage of 75 V peak.

The experiment was performed at the large outdoor wooden tank facility, as depicted in Fig. 5.11. A broadband noise survey was performed to access an S/N for the experiment. Both the rms level and the coherency

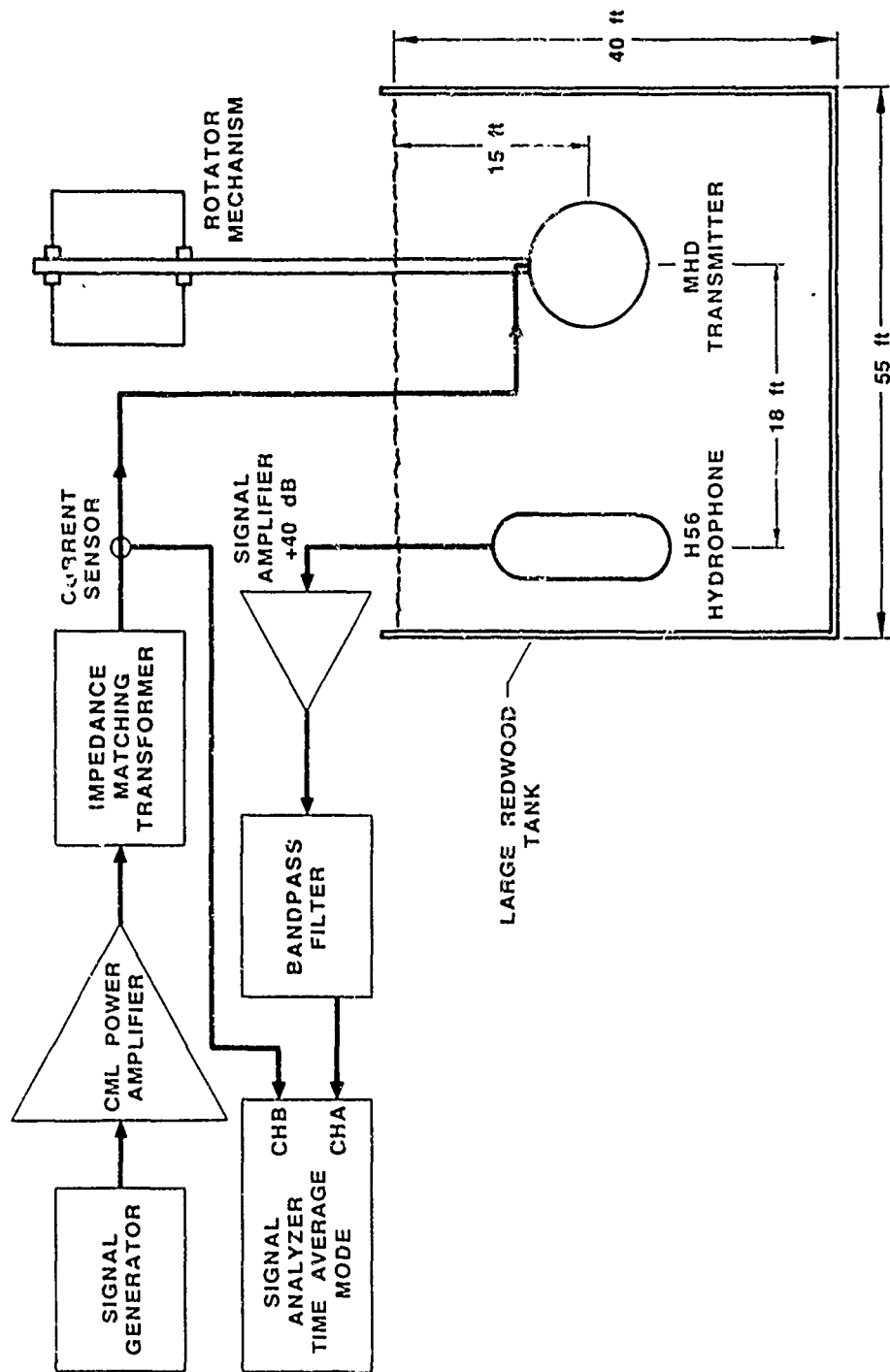


FIGURE 5.11
BLOCK DIAGRAM OF MHD ACOUSTIC SIGNAL
MEASUREMENT SYSTEM

ARL UT
AS-86-268
SCS - GA
5 - 27 86

between two hydrophones 1 m apart were measured and averaged over a period of 500 ms. Over the band from 500 to 3500 Hz the rms noise SPL was approximately 97 dB (re 1 μ s) and then proceeded to drop off at 20 dB/decade. The coherency was measured to be less than 0.4 over much of the band from 500 to 10000 Hz, which suggests that coherent ping to ping averaging of the received acoustic signal should be a successful method for eliminating the narrowband noise after filtering.

The calculated SPL, on axis, at 15 ft range for 5000 W of input power at 500 Hz is 89 dB which gives an S/N of -8 dB, this represents the worst S/N figure. At 5000 Hz the SPL is 123 dB and the S/N is 12 dB. Signal averaging thus became a mandatory process. Typically ten signal averages were required to reduce the noise by 20 dB. And typically a center frequency to filter band ratio of 10 was maintained with the bandpass filter to eliminate broadband signal noise.

The acoustic signal measurement system consists of a broadband hydrophone (NRL USRD H56 reference standard hydrophone), signal amplifier, bandpass filter, and a Nicolet 4094 digital oscilloscope (the Nicolet has a signal averaging mode). The signal amplifier provided 40 dB of gain necessary for lifting the signal above the electrical noise produced by the transmission cable's 150 ft run from the tank to the building.

The MHD transducer was mounted on a rotator column, depicted in Fig. 5.12, and lowered to a depth of 15 ft. The MHD transducer and hydrophone were separated by a distance of 18 ft, which placed the

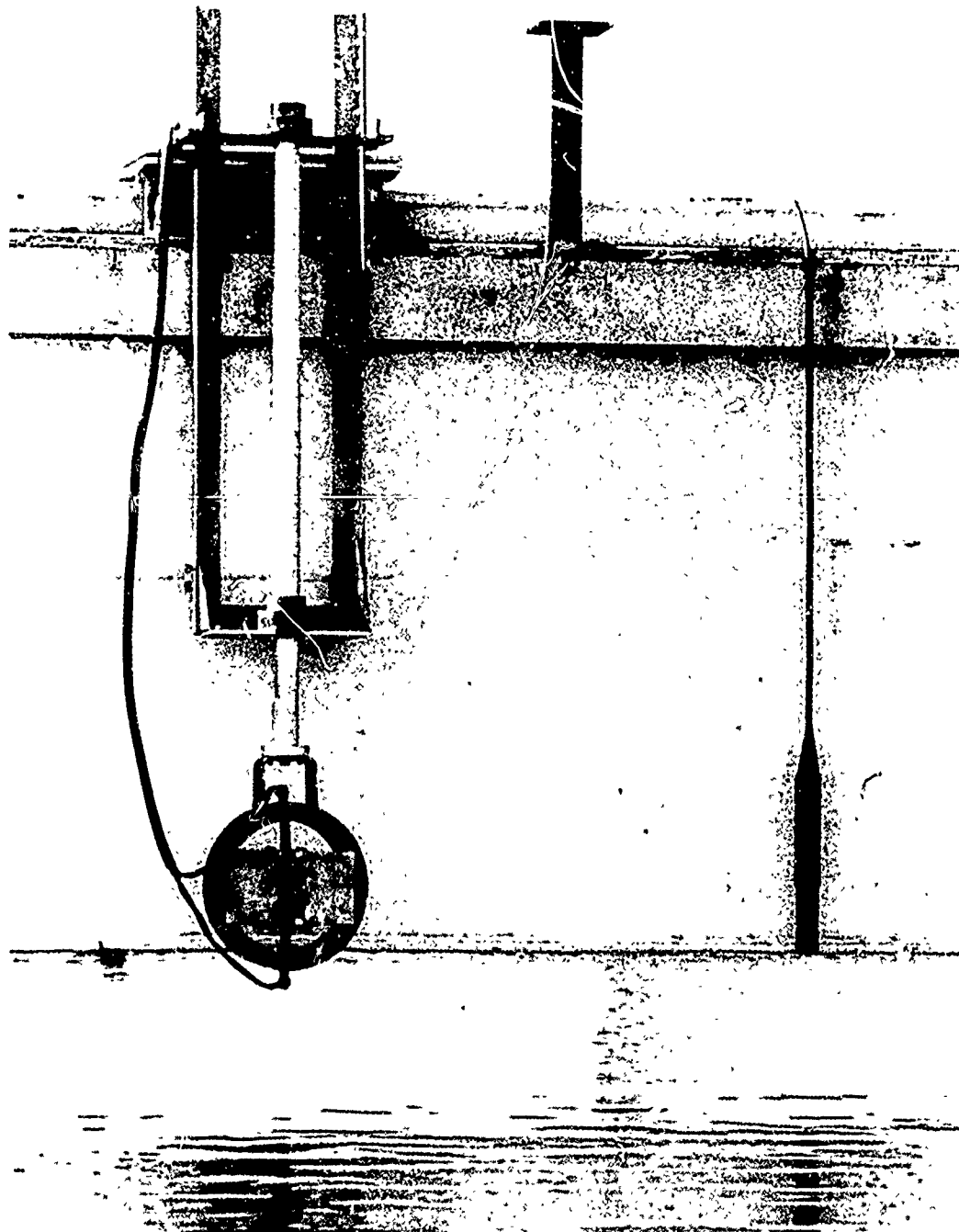


FIGURE 5.12
MHD TRANSDUCER MOUNTED ON THE ROTATOR
COLUMN WITH THE H56 HYDROPHONE

hydrophone well into the farfield over the entire frequency band, and allowed a maximum gated transmit signal of 5 ms; the gate time was limited by the surface reflection path length of the transmitted acoustic signal. The 5 ms gate time set a lower limit on the frequency band of the transmitted signal to 500 Hz, which is 2.5 cycles.

E. MEASUREMENT OF THE MHD TRANSMITTING SENSITIVITY AND DIRECTIVITY

The TCS on the waveguide axis was measured for the frequency band from 500 Hz to 13000 Hz. A typical time domain pressure signal received while making the sensitivity measurement, along with the current waveform, are shown in Fig. 5.13. The acoustic signal shown is the result of ten ping-to-ping averages and bandpass filtering.

The transmitting current sensitivity is defined in this thesis as $20 \log_{10}$ of the peak pressure divided by the peak current. Figure 5.14 shows the comparison of measured current sensitivity and the theoretical prediction from Eq. (4.22b). Good agreement was found between theory and experiment for the 500 Hz to 4000 Hz band with most measured values within 2 dB of the theory. Erratic behavior of the measured data for frequencies greater than 4000 Hz can probably be attributed to two causes. First, two restrictions were placed on the theory on Chapter 3, $R_a/R_s \ll 1$ and $kR_a \ll 1$. The first constraint is set by the geometry to be effectively 0.392, which therefore might raise some doubt about the transducer design. However, the good fit of the data at less than 4000 Hz seems to relax the importance of this constraint. At 4000 Hz, $kR_a = 0.33$ (which again is not much

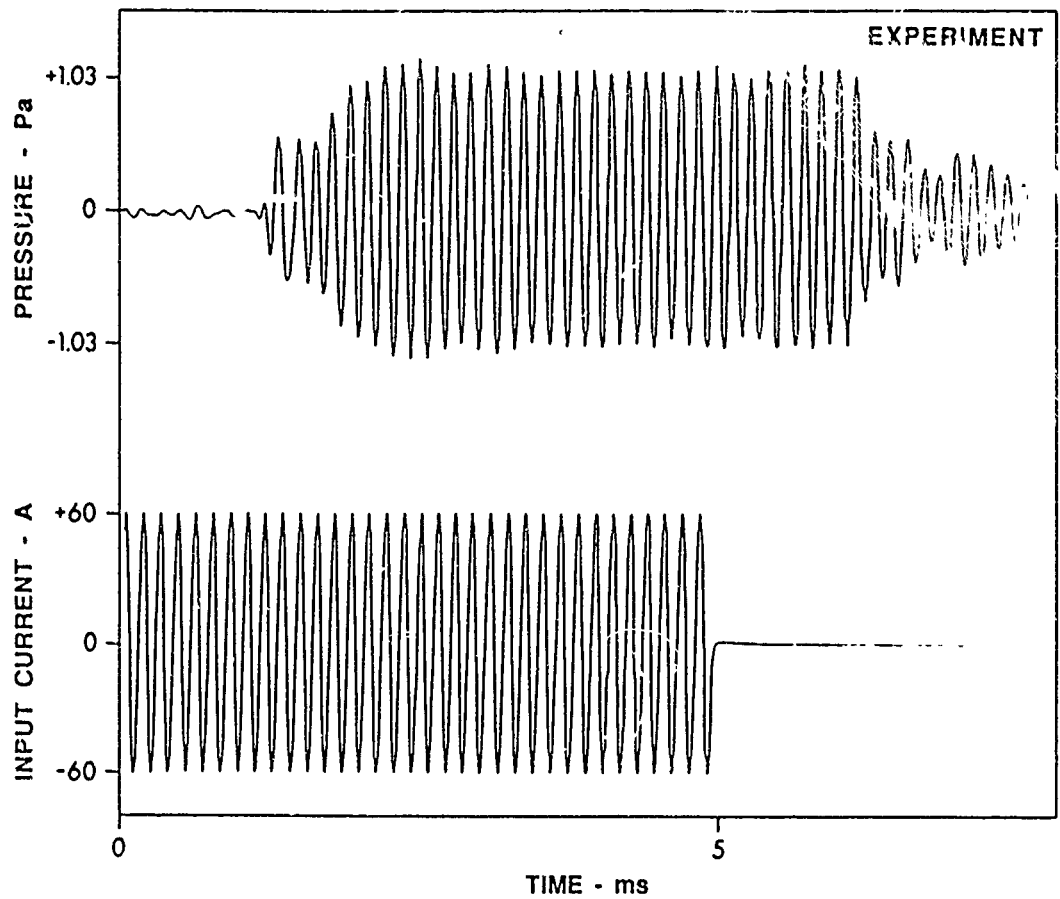


FIGURE 5.13
CONSTRUCTIVE INTERFERENCE OF THE MHD PRESSURE
SIGNAL ON THE WAVEGUIDE AXIS, $\psi = 0^\circ$, AT 6900 Hz

ARL:UT
AS-86-437
SCS - GA
8 - 6 - 86

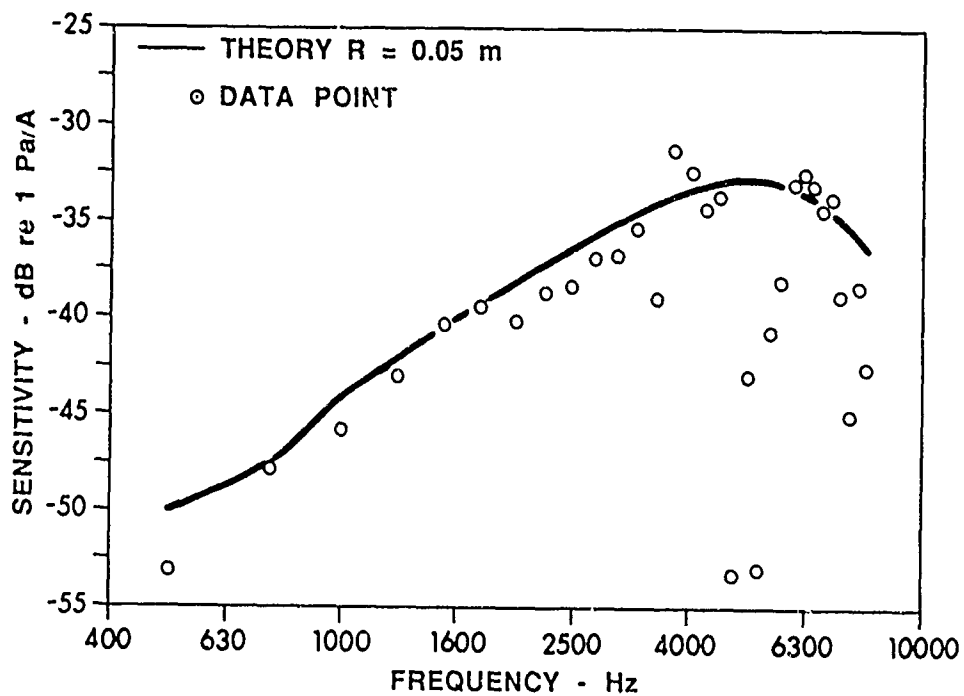


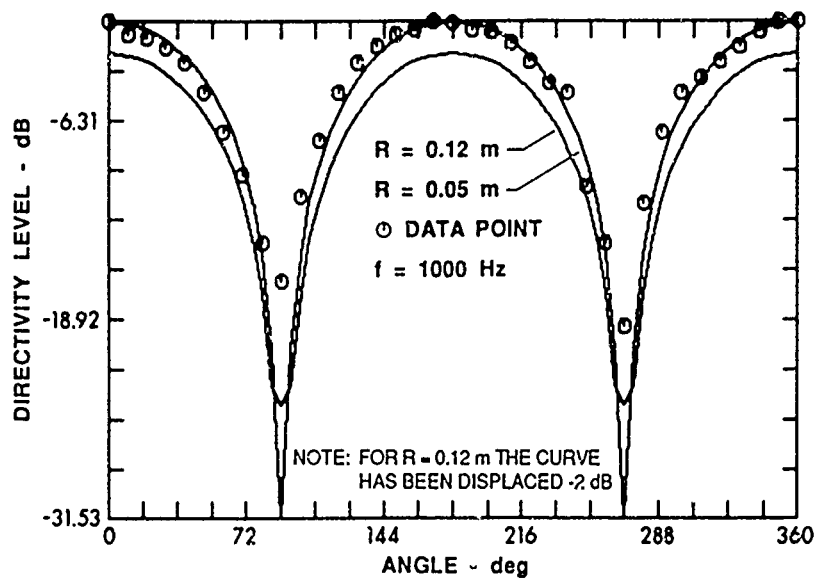
FIGURE 5.14
 MAGNETOHYDRODYNAMIC TRANSMITTING
 SENSITIVITY EXPERIMENT AND THEORY
 6% NaCl-H₂O SOLUTION
 MEASUREMENTS MADE ON WAVEGUIDE X AXIS

less than 1), may indicate that the aperture radius to wavelength restriction is more severe than the constraint of planar motion of the particle velocity at the aperture.

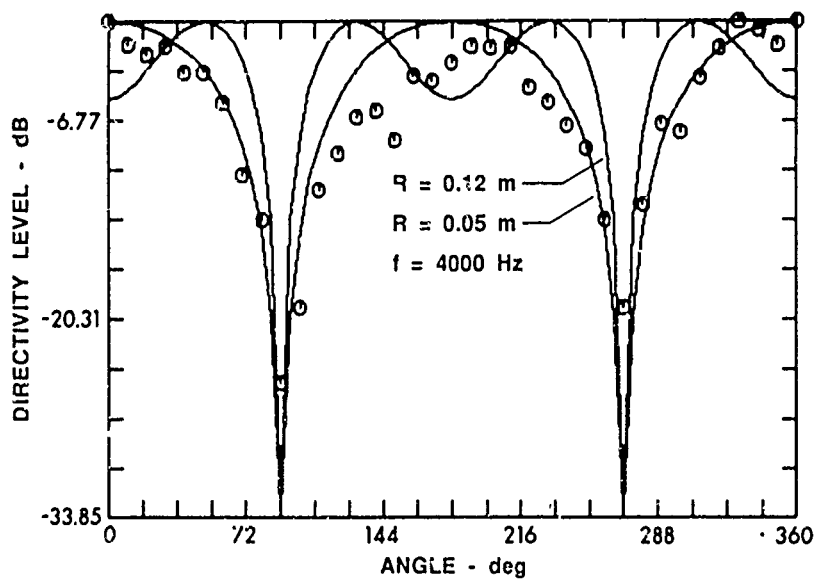
The second cause is the non-spherical construction of the transducer (see Fig 5.1). Since the measured data do not diverge smoothly from the theory one would expect that diffraction caused by the irregular geometry of the magnetic circuit structure is at fault. At 4000 Hz the wavelength is 37.5 cm and the diameter of the ring structure is 29.2 cm, so diffraction should be expected. Given the geometrical restrictions of the theory and good fit of data well beyond those restrictions one can conclude that the theoretical approach is appropriate.

Shown in Figs. 5.15(a), (b), (c), and (d) are the measured and predicted directivity patterns for 1000, 4000, 6000, and 10000 Hz (the theoretical directivity patterns were computed by the FORTRAN program MHD). The theoretical directivities are shown for two different baffle radii to emphasize the importance of the baffle size in determining the directivity pattern. In Fig. 5.16 the equivalent baffle radius is compared to the actual transducer geometry.

The directivity patterns were measured at 10° intervals for a complete 360° rotation of the MHD transducer. At 1000 Hz there is excellent data agreement with theory. At 4000 Hz there is some significant divergence, and at 6000 and 10000 Hz the data and theory do not correlate, except near the 90° and 270° null. The directivity pattern at 4000 Hz, and higher frequencies, indicates that diffraction by other parts of the transducer is



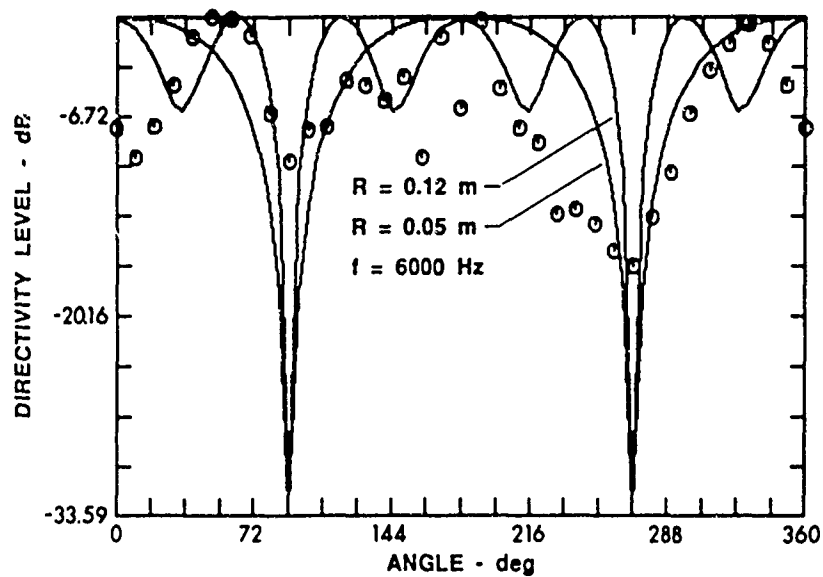
(a)



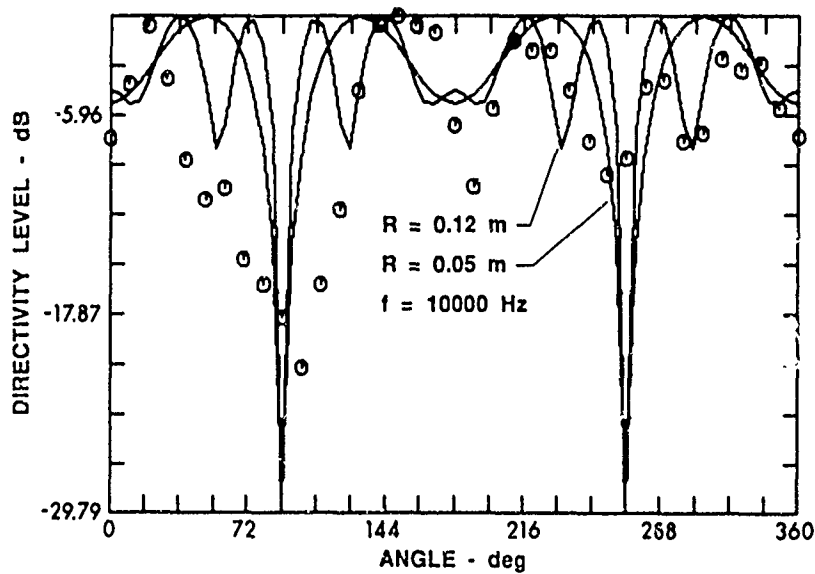
(b)

FIGURE 5.15
MAGNETOHYDRODYNAMIC SOURCE DIRECTIVITY
FARFIELD THEORY AND EXPERIMENT

ARL:UT
AS-86-452
SCS - GA
8-6-86



(c)



(d)

FIGURE 5.15 (cont'd)
MAGNETOHYDRODYNAMIC SOURCE DIRECTIVITY
FARFIELD THEORY AND EXPERIMENT

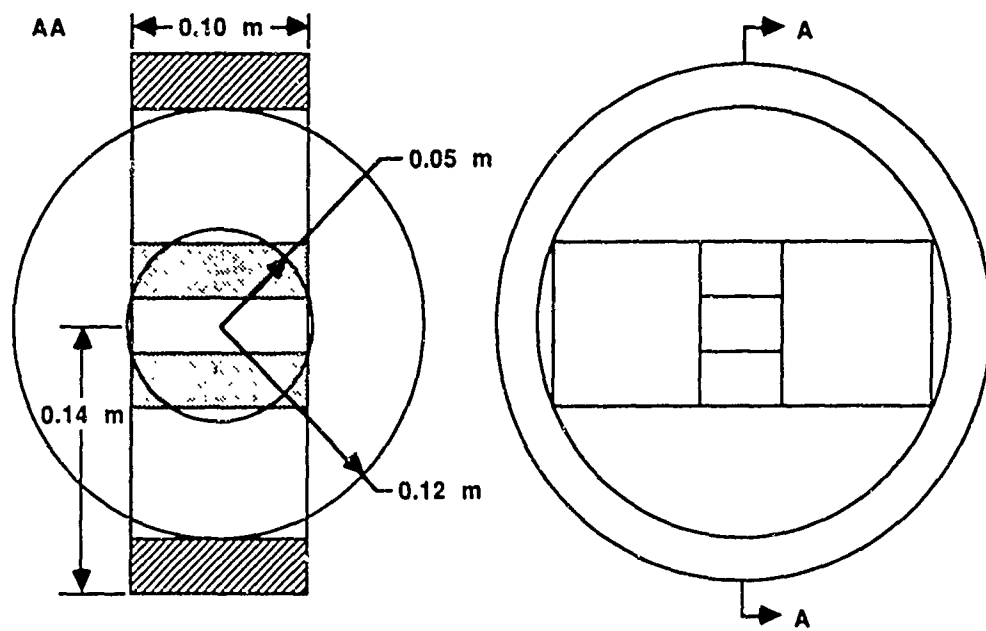


FIGURE 5.16
EFFECTIVE BAFFLE RADII OF THE MHD TRANSDUCER

ARL:UT
AS-86-450
SCS - GA
8 - 6 - 86

significant and is thus the cause of the divergence of the on-axis sensitivity data above 4000 Hz.

F. MEASUREMENT OF THE THERMOACOUSTIC TRANSMITTING SENSITIVITY

Measurement of the QVTS was made on the waveguide axis for the single input frequency, in the band between 500 and 4000 Hz, which corresponds to the transmitted acoustic frequency doubled band of 1000 to 8000 Hz. In order to measure the thermoacoustic signal it was necessary to remove the waveguide from the magnetic ring structure, thus eliminating the MHD signal. Accurate measurement of the thermoacoustic signal in the presence of the MHD signal proved to be difficult because of MHD signal interference. Even though the bandpass filter rejected 40 dB of the MHD signal amplitude, spectral leakage was a problem.

A typical thermoacoustic time waveform is shown in Fig. 5.17. Notice the frequency doubled pressure signal relative to the input current signal. Noise was much more of a problem in measuring the thermoacoustic signal since the pressure signal is typically 10 dB below the levels measured for the MHD process.

The measured QVTS data and the theory are plotted in Fig. 5.18 as a function of the input signal frequency. The QVTS in this plot is defined as the peak pressure divided by the square of the peak terminal voltage. In this case the quadratic current transmitting sensitivity is related to the QVTS by subtracting 7 dB from the latter.

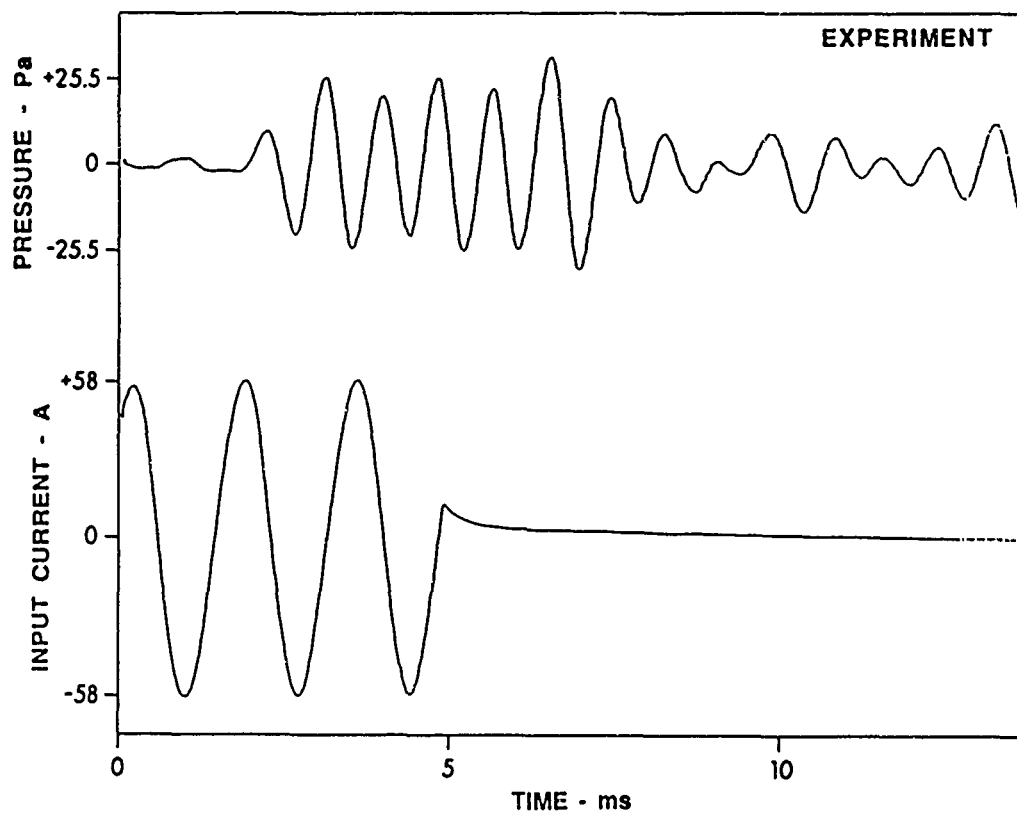


FIGURE 5.17
SECOND HARMONIC THERMOACOUSTIC PRESSURE SIGNAL
 $f_{\text{INPUT}} = 500 \text{ Hz}$ $f_{\text{SIGNAL}} = 1000 \text{ Hz}$

ARL:UT
AS-86-436
SCS - GA
8 - 6 - 86

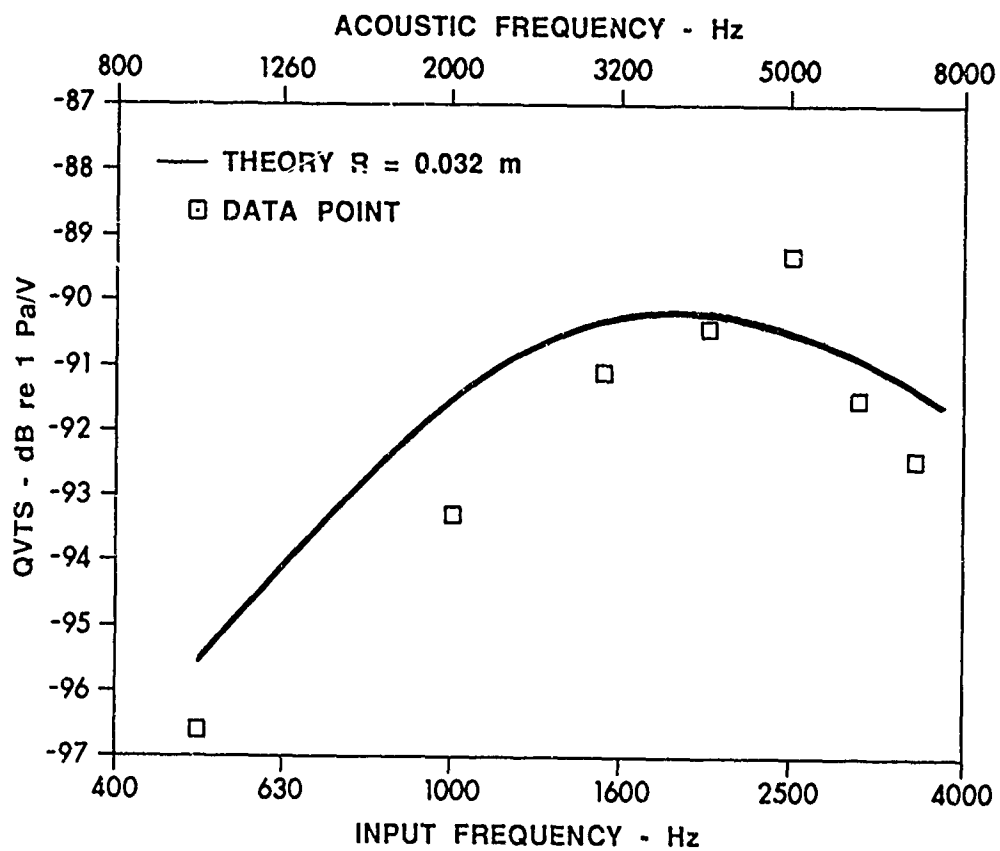


FIGURE 5.18
THERMOACOUSTIC QUADRATIC VOLTAGE TRANSMITTING
SENSITIVITY (QVTS)
THEORETICAL AND EXPERIMENTAL DATA COMPARISON

The number of data points shown in Fig. 5.18 are limited due to difficulties with the transducer fluid chemistry. The thermoacoustic data were gathered several months after the experiment was set up, and during this time the electrode surfaces had begun to corrode. The electrodes are copper with nickel and gold electroplated on the surface. At the time of the thermoacoustic experiment the copper had apparently reacted with the nickel and blistered the gold plate off the surface, exposing the now oxidized copper surface. As a result large quantities of undissolved gases were generated due to a copper oxide-chlorine reaction. After virtually each ping the transducer had to be raised from the tank and checked for visible gas bubbles, and the sodium chloride and water solution changed. Thus few reliable data points were generated. However, the few points that were obtained generally fit within 2 dB.

As a note to the problem of hydrogen and chlorine gas evolution within the transducer, the gases seemed to stay dissolved until the saturation concentration was reached for Cl_2 , which is 0.0004 moles/liter. In order to produce this concentration in the waveguide a total charge transfer of 93°C is required. At 60 A-peak current the average current is 38.2 A; thus 1.54 s of current is required to produce the saturation concentration of chlorine gas. This is equivalent to 309 5 ms pings, which is enough data to generate the data in Fig. 5.14. However, the transducer must be periodically shaken to dissolve small nucleated gas bubbles which can sometimes form on the surface of the electrode. The curious inconsistency in the production of hydrogen and chlorine is that it does not seem to react to form hydrochloric

acid according to Eq. (4.6) and thus neutralize the buildup of sodium hydroxide that results according to the overall electrode reaction, Eq. (4.5). The dissolved chlorine gas seems to reach saturation when bubbles are noticed in the waveguide after approximately 250 pings.

CHAPTER 6

CONCLUSIONS

This thesis has examined the behavior of an underwater acoustic transmitter based on the magnetohydrodynamic principle. The transducer consists of a waveguide filled with salt water and exposed to orthogonal magnetic and electric fields. The magnetic field was generated by permanent magnets, and the electric field was time harmonic in order to produce oscillatory force on the salt water causing an acoustic signal. This electric field results in electric current flow which causes heating and thermoacoustic radiation of sound as well as producing sound through the MHD mechanism. Both sound generating mechanisms were examined.

The linear inhomogeneous pressure wave equation which characterizes the MHD and thermoacoustic sound mechanisms was derived. The inhomogeneous equation was solved assuming a plane wave pressure field within the waveguide. The plane wave field was matched at the waveguide apertures to a spherical wave pressure field in the free medium through impedance conditions at the waveguide apertures. From the wave field solutions the MHD and thermoacoustic mechanism transmitting sensitivities were derived to predict the farfield radiation from an "hypothetical" spherically baffled MHD transducer.

There were three phases of the experimental investigation: measurement of the electrical input impedance, measurement of the on-axis transmitting sensitivities, and measurement of the acoustic radiation

directivity. Due to the weight limitations the transducer which was built did not resemble a sphere with a channel through the center, as was assumed in the theoretical development, but the measurements made correlated very well with the theoretical predictions.

A model of the electrode polarization impedance was used, which produced accurate theoretical predictions. The polarization impedance took into account the chemical diffusional impedance and included a relatively simple model for the double layer impedance. It can be concluded from the impedance measurements that a model of the transducer which places the polarization impedance in series with the electrolyte impedance is appropriate for NaCl-water electrolytes and noble metal planar electrodes.

Measurements of the MHD transmitting sensitivity were, in general, in good qualitative and quantitative agreement with the theory. The data comparison shows that up to 4000 Hz the agreement is within 2.5 dB. Above this frequency the predicted and measured MHD directivities diverge significantly, due to the difference between the assumed and actual transducer geometries.

The measured MHD directivity pattern at 1000 Hz showed excellent agreement with the computed directivity. At 4000 Hz the directivity, while corrupted due to the non-spherical nature of the transducer does agree fairly well with predictions assuming a spherical baffle of 5 cm radius. In general, at low frequencies, the transducer makes an excellent dipole radiation transducer.

The measurements of the thermoacoustic radiation were very difficult to make, but given the limited amount of data one can see a reasonably good theoretical agreement. Since time was not available to measure reliable directivity patterns for the thermoacoustic source mechanism, absolute validity of the sensitivity data is lacking. The directivity of the thermoacoustic source is predicted by the computer code to be omnidirectional within 0.05 dB for 1000 Hz. Measurements on axis and 90° off axis were made and the values were within 2 dB; however, this is not proof that there was actually a monopole directivity.

Considering the geometrical and wave number constraints of the theory, all of the measurements are in good agreement and use of the theory for even a "moderately" exceeded operating frequency range seems justifiable.

The experiments reported here were limited to a frequency band 500 to 13000 Hz. At the low end of this regime, the size of the testing tank was the limiting factor. Frequencies lower than 500 Hz would have been interesting to examine since the lower frequencies necessarily imply larger particle velocity amplitudes. Studies at higher velocity amplitudes might have given some indication of the range of validity of both the aperture acoustic impedance model and electrical impedance model. However, facilities for a larger free field environment and a means to increase the source level were not available.

With regard to the input power available for the experiment, sufficient current was not available to test the limit of the approximation

imposed on the use of the linearized Nernst equation for derivation of the diffusional impedance. Thus, nonlinear behavior of the polarization impedance at large current densities would be an interesting phenomenon to study more closely since any source using the MHD mechanism to produce "practical" pressure levels (using an electrolyte) would be operating in this nonlinear impedance regime.

Since the constraint on the small temperature rise assumption of the thermoacoustic assumption allows (effectively) for a very large current density, testing the effects of exceeding this limit might require the use of a pulsed power generator or capacitor bank.

APPENDIX A.1

DERIVATION OF THE MAGNETIC DISPERSION RELATION

The derivation of the magnetic dispersion relation to follow is included to supplement the discussion of Chapter 2. The small signal momentum, continuity, and state equations of Chapter 2 are restated below with the exclusion of the thermoacoustic term present in the continuity equation, Eq. (2.24), because the term simply generates terms of second order compared with the dispersion term of the MHD source.

The equations derived in Chapter 2 are:

the small signal momentum equation,

$$\rho_0 \mathbf{u}_t + \nabla p = \mathbf{J} \times \mathbf{B}, \quad (2.25)$$

small signal continuity equation,

$$\rho_t + \rho_0 \nabla \cdot \mathbf{u} = 0, \quad (\text{A.1.1})$$

and small signal state equation,

$$p = c_0^2 \delta \rho. \quad (2.23)$$

The expression for the current density \mathbf{J} from Chapter 2 is (neglecting the displacement current),

$$\mathbf{J} = \sigma (\mathbf{E} + \mathbf{u} \times \mathbf{B}). \quad (2.1)$$

Inserting the expression for \mathbf{J} into Eq. (2.31),

$$\rho_0 \mathbf{u}_t + \nabla p = \sigma (\mathbf{E} + \mathbf{u} \times \mathbf{B}) \times \mathbf{B} \quad (\text{A.1.2})$$

a momentum equation in terms of the new source field \mathbf{E} and the damping term $\sigma \mathbf{u} \times \mathbf{B} \times \mathbf{B}$ is found. The divergence of Eq. (A.1.2) is now taken,

$$\nabla^2 p + \rho_0 \nabla \cdot \mathbf{u}_t = \sigma \nabla \cdot (\mathbf{E} + \mathbf{u} \times \mathbf{B}) \times \mathbf{B}, \quad (\text{A.1.3})$$

and the continuity equation, Eq. (A.1.1), is differentiated with respect to time with the state equation substituted for p ,

$$\nabla \cdot \mathbf{u}_t = \frac{-p_{tt}}{\rho_o c_o^2} . \quad (\text{A.1.4})$$

Substituting Eq. (A.1.4) into Eq. (A.1.3) results in the inhomogeneous wave equation,

$$\nabla^2 p - 1/c_o^2 p_{tt} = \sigma \nabla \cdot (\mathbf{E} + \mathbf{u} \times \mathbf{B}) \times \mathbf{B} . \quad (\text{A.1.5})$$

Since the goal here is the derivation of the plane wave dispersion relation, the inhomogeneous term, $\sigma \nabla \cdot \mathbf{E}$, can be dropped and the homogeneous wave equation can be written in one-dimensional form,

$$p_{xx} - 1/c_o^2 p_{tt} - \sigma B_o^2 u_x = 0 . \quad (\text{A.1.6})$$

From the continuity equation, Eq. (A.1.1) and Eq. (2.29), u_x is related to p as

$$u_x = -p_t / \rho_o c_o^2 . \quad (\text{A.1.7})$$

Substituting Eq. (A.1.7) into Eq. (A.1.6) yields the final form of the homogeneous wave equation,

$$p_{xx} - 1/c_o^2 p_{tt} + \sigma B_o^2 / \rho_o c_o^2 p_t = 0 . \quad (\text{A.1.8})$$

The dispersion relation is found by substitution of the assumed harmonic progressive form of the plane wave solution into Eq. (A.1.8),

$$p(x,t) = p_o e^{j(kx - \omega t)} , \quad (\text{A.1.9})$$

which produces

$$(-k^2 + (1/c_o^2) \omega^2 - j(\sigma B_o^2 / \rho_o c_o^2) \omega) p_o e^{j(kx - \omega t)} = 0 . \quad (\text{A.1.10})$$

Hence, the magnetic field dispersion relationship is

$$k = \left(\left(\frac{\omega}{c_o} \right)^2 - \frac{j \omega \sigma B_o^2}{\rho_o c_o^2} \right)^{1/2} . \quad (A.1.11)$$

APPENDIX A.2

THERMOVISCOUS PROCESSES WITHIN THE WAVEGUIDE

This appendix will threat the justification for neglecting the thermoviscous processes in the theoretical analysis of Chapters 2, 3, and 4. Primarily the effects of viscosity are being neglected so as to simplify the analysis and allow an unobcured treatment of the magnetohydrodynamic and thermoacoustic acoustic source mechanism. The assumptions made in the modeling process of the MHD transducer are justifiable in the framework of the theory applied to the experimental transducer study and are not in general always applicable.

Losses in a thermoviscous medium occur due to two primary mechanisms, heat conduction and viscous molecular interaction. The losses from these two mechanisms will be considered in terms of the acoustic resonance quality factor, Q_n , of the nth resonance mode. The quality factor will be used to compute the half power bandwidth of the nth harmonic and compared to estimates from the theory of Chapter 3, which take into account only radiation losses.

For plane wave propagation in seawater the attenuation due to thermoviscous absorption at 10000 Hz is α_{TV} of 8.1×10^{-5} Nep/m.²⁷ From Kinsler and Frey²⁸ the expression for the Q is

$$Q_n = \frac{k_n}{2\alpha} \quad (\text{A.2.i})$$

The first resonance mode is approximately the full wavelength pressure mode; for a waveguide 0.10 m long the frequency is

approximately 15000 Hz. Taking the wave speed to be 1500 m/s, Q_1 is 260000. The half power bandwidth is therefore 0.06 Hz, a very "sharp" resonance.

The attenuation coefficient due to the boundary layer losses for an isothermal waveguide wall is given as²⁹

$$\alpha_{BL} = \frac{1}{R_a} \left(\frac{\omega\mu}{2\rho_o c_o^2} \right)^{1/2} \left(1 + \frac{\mu - 1}{Pr} \right) \quad (A.2.2)$$

with the constraint on Eq. (A.1.1) that

$$k \delta_{visc} \Big|_{10000 \text{ Hz}} \ll k R_a \Big|_{500 \text{ Hz}} \ll \frac{1}{k \delta_{visc}} \Big|_{500 \text{ Hz}} \quad (A.2.3)$$

where $\delta_{visc} = 2\mu/\omega\rho_o$ is the viscous boundary layer thickness. For seawater the following fluid property values are used for computing α_{TV} .³⁰

$\mu = 0.001 \text{ N s/m}^2$	coefficient of viscosity
$\gamma = 1.01$	ratio of specific heats
$\rho_o = 1026 \text{ kg/m}^3$	mass density
$c_o = 1500 \text{ m/s}$	adiabatic sound speed

For an aperture radius R_a of 0.02 m the theory is valid for the entire frequency spectrum from 500 to 10000 Hz, with bounds of $0.000234 \ll 0.0419 \ll 955.0$. The α_{BL} is 0.0035 Nep/m which yields a Q_1 of 5984 and a half power bandwidth of 2.5 Hz.

Figure A.2.1 shows a graph of the maximum acoustic pressure predicted by the theory presented in Chapter 3, which takes account of radiation losses only. It is seen from this graph that the half power bandwidth of 9400 Hz is very large compared to either of the numbers calculated

above. Also plotted in the graph is the maximum pressure for a sound speed of 650 m/s; again a large bandwidth is noted. The conclusion to be drawn is that thermoviscous mechanisms play an insignificant role in the dynamics of the acoustic processes occurring within the waveguide of the specified geometry and frequencies of interest noted here.

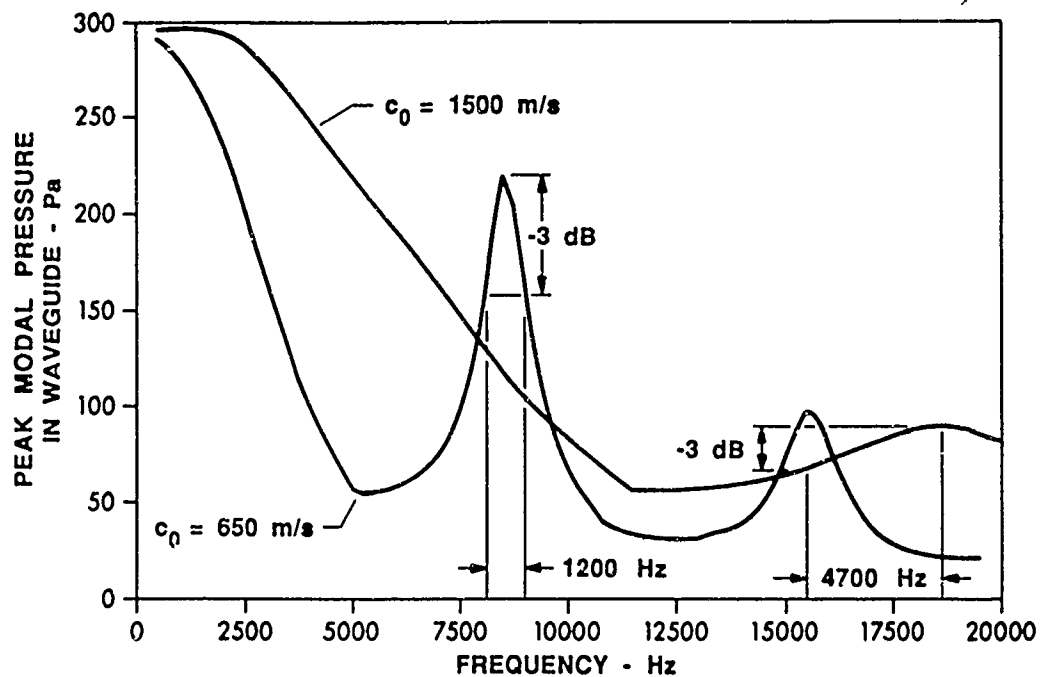


FIGURE A.2.1
 PEAK MODAL PRESSURE IN THE MHD WAVEGUIDE AS
 A FUNCTION OF FREQUENCY Q DETERMINATION PLOT
 6% NaCl-H₂O SOLUTION
 $\ell_s = 0.10$ m, $\ell = 0.10$ m, $R = 0.09$ m

ARL:UT
 AS-86-439
 SCS - GA
 8-6-86

APPENDIX B

PRESSURE FIELD SPHERICAL HARMONIC FUNCTION EXPANSION, RADIATION IMPEDANCES, AND FARFIELD PRESSURE

The calculation of the mutual radiation impedance requires that the acoustic field be specified. Therefore the first task is to specify the source and boundary conditions. In this case the sources are two circular pistons on the surface of a rigid spherical baffle radiating into an acoustic free space. The pistons are positioned 180° apart on the sphere which gives the radiation an axis of symmetry through the piston centers. Thus there is only one angle ψ , on which the field will be dependent (see Fig. B.1). The results that are presented follow directly from Sherman's³¹ results with the above conditions.

The pressure at any point in free space outside the sphere can be expressed as the sum of the pressure fields generated by the individual pistons,

$$p_{fm}(r, \psi) = p_{\ell fm}(r, \psi) + p_{- \ell fm}(r, \psi) . \quad (B.1)$$

The spherical harmonic function expansion is stated below for the pressure field resulting from one piston on the sphere.

$$p_{\ell fm}(r, \psi) = \pm j \rho_{fm} c_{fm} u(\pm \ell) \sum_{n=0}^{\infty} \frac{(P_{n-1}(\cos \Theta) - P_{n+1}(\cos \Theta)) P_n(\cos \psi) h_n^1(kr)}{\left. \frac{d}{dx} h_n^1(x) \right|_{x=kR}} \quad (B.2)$$

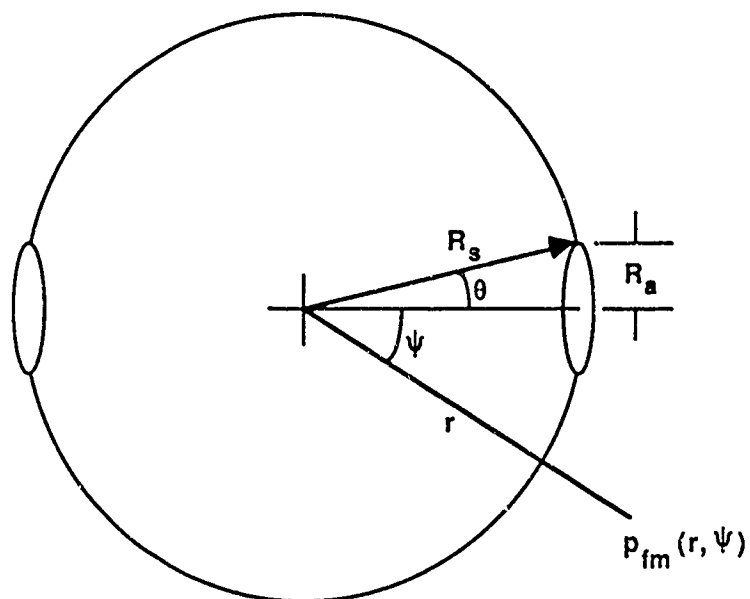


FIGURE B.1
APERTURE GEOMETRY

In Eq. (B.2), $P_{n\pm 1}$ and P_n are the ordinary Legendre polynomials of order $n\pm 1$ and n , $\cos\Theta$, and $\cos\psi$ are the arguments of the Legendre polynomials where Θ is the half angle of the source radius, and ψ is the coordinate angle referenced to the source symmetry axis. $h_n^1(kr)$ is the Hankel function of the first kind of order n and is a function of kr , where r is the radial distance to a point in free space and R is the sphere radius.

The calculation of the mutual radiation impedance follows directly from Eq. (B.2). The pressure is evaluated on the surface of the sphere, $r = R$, substituted into Eqs. (3.4a,b) and integrated over the angular sector of the source aperture from $\psi = 0$ to $\psi = \Theta$. For the case of the waveguide geometry used in the experiment the mutual impedance is as follows

$$Z_{z\ell fm}(r, \psi) = \pm j p_{fm} c_{fm} e^{j\mu_{\pm\ell}} \sum_{n=0}^{\infty} \frac{1}{2n+1} \frac{(P_{n-1}(\cos\Theta) - P_{n+1}(\cos\Theta))^2 h_n^1(kR)}{\left. \frac{d}{dx} h_n^1(x) \right|_{x=kR}} \quad (B.3)$$

where μ is the relative temporal phase between the sources.

Equation (B.3) is valid for both apertures provided they are of equal radius or as stated above, angular sector Θ . The expression is independent of the magnitude of the particle velocity since the aperture velocity distribution was assumed to be purely planar motion.

Calculation of the farfield pressure is accomplished using the farfield approximation to Eq. (B.1), which is to say the approximations are made in Eq. (B.2). Note that Eq. (B.2) is an exact solution to the pressure

field for the stated boundary conditions. However, when in the farfield, the large argument form of the Hankel functions save much computational overhead. Without proof the farfield analog of Eq. (B.2) is stated below. See, again, Sherman for a more complete discussion.

$$p_{ff}(r, \psi) = \frac{j p_{fm} c_{fm} e^{jkr}}{2kr}$$

$$\left\{ -u(-\ell) \sum_{n=0}^{\infty} \frac{(P_{n-1}(\cos\Theta) - P_{n+1}(\cos\Theta)) P_n(-\cos\psi) e^{-j\pi(n+1)/2}}{\left. \frac{d}{dx} h_n^1(x) \right|_{x=kR}} \right.$$

$$\left. + u(\ell) \sum_{n=0}^{\infty} \frac{(P_{n-1}(\cos\Theta) - P_{n+1}(\cos\Theta)) P_n(\cos\psi) e^{-j\pi(n+1)/2}}{\left. \frac{d}{dx} h_n^1(x) \right|_{x=kR}} \right\} \quad (B.4)$$

APPENDIX C

REFLECTION COEFFICIENT EQUATIONS

Due to the complexity of the coefficients a hierarchy of dummy variables are defined below to construct more simplistic forms.

$$A = e^{-jk\ell} \quad (C.1a)$$

$$B = e^{jk\ell} \quad (C.1b)$$

$$C = e^{jka} - e^{jkb} \quad (C.1c)$$

$$D = e^{-jka} - e^{-jkb} \quad (C.1d)$$

The dummy variables for the MHD reflection coefficient equations are as follows.

$$\underline{A} = BD(1 - Z_s/\rho_o c_o) - BC Z_m/\rho_o c_o \quad (C.2a)$$

$$\underline{B} = AD(1 + Z_s/\rho_o c_o) - BD Z_m/\rho_o c_o \quad (C.2b)$$

$$\underline{C} = BC(1 - Z_s/\rho_o c_o) + AC Z_m/\rho_o c_o \quad (C.2c)$$

$$\underline{D} = AC(1 + Z_s/\rho_o c_o) + AD Z_m/\rho_o c_o \quad (C.2d)$$

$$\underline{E} = BC(1 - Z_s/\rho_o c_o) - BD Z_m/\rho_o c_o \quad (C.2e)$$

$$\underline{F} = BD(1 - Z_s/\rho_o c_o) + AD Z_m/\rho_o c_o \quad (C.2f)$$

$$\underline{G} = AC(1 + Z_s/\rho_o c_o) - BC Z_m/\rho_o c_o \quad (C.2g)$$

$$\underline{H} = AD(1 + Z_s/\rho_o c_o) + AC Z_m/\rho_o c_o \quad (C.2h)$$

The coefficients for the MHD reflection coefficient equations, Eqs. (3.18a,b), are as follows in term of the above underlined dummy variables.

$$C_1 = \underline{A} \underline{F} - \underline{B} \underline{E} \quad (C.3a)$$

$$C_2 = \underline{A} \underline{H} - \underline{B} \underline{G} + \underline{C} \underline{F} - \underline{D} \underline{E} \quad (C.3b)$$

$$C_3 = \underline{Q} \underline{H} - \underline{D} \underline{G} \quad (C.3c)$$

$$C_4 = \underline{Q} \underline{E} - \underline{A} \underline{G} \quad (C.3d)$$

$$C_5 = \underline{D} \underline{E} + \underline{Q} \underline{F} - \underline{B} \underline{G} - \underline{A} \underline{H} \quad (C.3e)$$

$$C_6 = \underline{D} \underline{F} - \underline{B} \underline{H} \quad (C.3f)$$

The dummy variables for the thermoacoustic reflection coefficient equations are as follows.

$$\underline{A} = BD(1 - Z_s/\rho_o c_o) + BC Z_m/\rho_o c_o \quad (C.4a)$$

$$\underline{B} = AD(1 + Z_s/\rho_o c_o) - BD Z_m/\rho_o c_o \quad (C.4b)$$

$$\underline{C} = BC(-1 + Z_s/\rho_o c_o) - AC Z_m/\rho_o c_o \quad (C.4c)$$

$$\underline{D} = -AC(1 + Z_s/\rho_o c_o) + AD Z_m/\rho_o c_o \quad (C.4d)$$

$$\underline{E} = BC(1 - Z_s/\rho_o c_o) + BD Z_m/\rho_o c_o \quad (C.4e)$$

$$\underline{F} = BD(-1 + Z_s/\rho_o c_o) - AD Z_m/\rho_o c_o \quad (C.4f)$$

$$\underline{G} = AC(1 + Z_s/\rho_o c_o) - BC Z_m/\rho_o c_o \quad (C.4g)$$

$$\underline{H} = -AD(1 + Z_s/\rho_o c_o) + AC Z_m/\rho_o c_o \quad (C.4h)$$

The coefficients for the thermoacoustic reflection coefficient equations, Eqs. (3.30a,b), are as follows in term of the above underlined dummy variables.

$$C_1 = \underline{A} \underline{F} - \underline{B} \underline{E} \quad (C.5a)$$

$$C_2 = \underline{A} \underline{H} - \underline{B} \underline{G} + \underline{Q} \underline{F} - \underline{D} \underline{E} \quad (C.5b)$$

$$C_3 = \underline{Q} \underline{H} - \underline{D} \underline{G} \quad (C.5c)$$

$$C_4 = \underline{Q} \underline{E} - \underline{A} \underline{G} \quad (C.5d)$$

$$C_5 = \underline{D} \underline{E} + \underline{Q} \underline{F} - \underline{B} \underline{G} - \underline{A} \underline{H} \quad (C.5e)$$

$$C_6 = \underline{D} \underline{F} - \underline{B} \underline{H} \quad (C.5f)$$

APPENDIX D

COMPUTER PROGRAMS

The numerical computation of the theoretical relations presented in the text of this thesis were computed by the FORTRAN programs MHD and THERMO. MHD is the analysis code for the magnetohydrodynamic source mechanism and is capable of computing the following relations as a function of frequency.

- 1) Aperture Reflection Coefficient
- 2) Complex Aperture Pressure and Particle Velocity
- 3) Complex Aperture Real and Self-Impedance
- 4) Complex Electrical Terminal Impedance
- 5) MHD Transduction Process Power Efficiency
- 6) Transmitting Current and Voltage Sensitivity
- 7) Farfield Pressure Directivity (single frequency)

The input parameters for "MHD" are

- 1) Frequency Band and Frequency Step Size
- 2) Waveguide Dimensions
- 3) Electrode Dimensions and Position within the Waveguide
- 4) Spherical Baffle Radius
- 5) Fluid Properties Inside and Outside the Waveguide
- 6) Conductivity of the Fluid Inside the Waveguide
- 7) Magnetic Induction and Current Density Amplitude in the Waveguide

THERMO is the analysis code for the thermoacoustic source mechanism. The following relations, as a function of frequency, are computed by THERMO.

- 1) Aperture Reflection Coefficient
- 2) Complex Aperture Pressure and Particle Velocity
- 3) Complex Aperture Real and Self-Impedance
- 4) Quadratic Current Transfer Function (QCTF)
- 5) Thermoacoustic Transduction Process Power Efficiency
- 6) Quadratic Voltage Transmitting Sensitivity (QVTS)
- 7) Farfield Pressure Directivity (single frequency)

THERMO has the same input parameter list that is given above for MHD except the following properties for the fluid within the waveguide are needed: specific heat capacity at constant pressure and coefficient of thermal expansion.

```

      PROGRAM MHD(INPUT,OUTPUT,DATA,TAPE2=INPUT,TAPE4=DATA
1,PLOT,TAPE5=PLOT)
C
C*****
C
C PROGRAM MHD PERFORMS A FREQUENCY DOMAIN ANALYSIS OF THE ELECTROACOUSTIC
C TRANSMITTING CHARACTERISTICS OF A PLANE WAVE MODE MHD TRANSDUCER
C MHD GENERATES GRAPHIC OUTPUT FOR THE FOLLOWING TRANSDUCER
C CHARACTERISTICS
C
C 1) MAGNITUDE OF THE REFLECTION COEFF (MRNL) VERSUS FREQUENCY (FREQ)
C 2) MAGNITUDE OF APERTURE PRESSURE (RPNL) VERSUS FREQ
C 3) DB LEVEL OF THE APERTURE PRESSURE (RPNL) VERSUS LOG10(FREQ)
C 4) " " OF APERTURE PART VEL (RVNL) VERSUS LOG10(FREQ)
C 5) IMAGINARY (IADM) VERSUS REAL (RADM) INPUT ELECTRICAL ADMITTANCE
C 6) " (ZELI) " (ZELR) " IMPEDANCE
C 7) DB LEVEL OF RADIATED ACOUSTIC POWER (PR) VERSUS LOG10(FREQ)
C 8) REAL COMPONENT OF INPUT ELECTRICAL POWER (PER) VERSUS FREQ
C 9) REACTIVE " " " (PERECT) "
C 10) DB LEVEL OF TRANSDUCTION POWER EFFICIENCY (EFFIC) VERSUS LOG10(FREQ)
C 11) DB LEVEL OF TRANSMITTING VOLTAGE SENSITIVITY (TVSL) VERSUS LOGFREQ
C 12) DB " " CURRENT (TCSL) "
C 13) APERTURE ACOUSTIC SELF IMPEDANCE REAL COMP (ZFMR) VERSUS FREQ
C 14) " " " IMAGINARY " (ZFMI) "
C 15) " " MUTUAL " REAL " (ZMR) "
C 16) " " " IMAGINARY " (ZMI) "
C 17) RATIO OF THE MAGNITUDES OF ZM / ZFM VERSUS FREQ
C 18) PRESSURE LEVEL DIRECTIVITY
C 19) ANGLE OF PRIMARY BEAM VERSUS FREQ
C
C DATA INPUT IS THROUGH THE CALL DATA STATEMENT AT THE END OF THE
C MAIN PROGRAM
C
C*****
C
COMMON /ZIP/ A,B,L,LY,LZ,SRAD,ROD,COD,ROM,COM,PI,BM
1,CD,CON,FO,FF,FD
DIMENSION FREQ(1000),FLOG(1000),PR(1000),PSPL(1000)
1,RPML(1000),RVNL(1000),RADM(1000),IADM(1000),MRNL(1000)
2,TCBL(1000),TVSL(1000),ANGMAX(1000),RA(1000)
3,ZMR(1000),ZMI(1000),ZFMR(1000),ZFMI(1000),RATIO(1000)
4,ZELR(1000),ZELI(1000),RVL(1000)
5,PER(1000),PERECT(1000),EFFIC(1000)
COMPLEX RNL(1000),RL(1000),PNL(1000),PL(1000)
1,VNL(1000),VL(1000)
2,QLNLA,QLNLB,QLRLA,QLRLB,QLBB,QLAB,GRAB,GRBA
3,QLNLA,QLNLB,QLRLA,QLRLB,QLBB,QLAB,GRAB,GRBA
4,ADMI(1000),ZEL(1000)
REAL IADM,K,L,LY,LZ,MRNL
INTEGER I,N
N = (FF-FD)/FD + 1
C
C PRIMARY CALCULATION LOOP
C
DO 1 I=1,N
C CALCULATE THE WAVE NUMBER AND FREQUENCY
K = (2 *PI*FO + FLOAT(I-1)*2 *PI*FD)/COD
FREQ(I) = K*COD/(2 *PI)
FLOG(I) = ALOG10(FREQ(I))
C REFL EVALUATES THE APERTURE REFLECTION COEFFICIENT
CALL REFL(K,RNL(I),RL(I),MRNL(I),ZMR(I),ZMI(I)
1,ZFMR(I),ZFMI(I))
C GREEN EVALUATES THE PLANE WAVE GREENS FUNCTION
CALL GREEN(K,A,B,L,RNL(I),RL(I),QLNLA,QLNLB,QLRLA,QLRLB
1,QLNLA,QLNLB,QLRLA,QLRLB,QLBB,QLAB,GRAB,GRBA)
GO TO 50
C ZM AND ZS ARE THE MAGNITUDES OF THE APERTURE SELF AND MUTUAL IMPEDANCES
ZM = (ZMR(I)**2 +ZMI(I)**2)**.5
ZS = (ZFMR(I)**2 +ZFMI(I)**2)**.5
RATIO(I) = ABS(ZM/ZS)
C PRES EVALUATES THE APERTURE PRESSURE IN THE WAVE GUIDE
CALL PRES(QLNLA,QLNLB,QLRLA,QLRLB,PNL(I),PL(I))
RPNL(I) = CABS(PNL(I))
PSPL(I) = 20 *ALOG10(RPNL(I)/.00001)
C VEL EVALUATES THE APERTURE PARTICLE VELOCITY
50 CALL VEL(K,QLNLA,QLNLB,QLRLA,QLRLB,VNL(I),VL(I),U1,U2,F1,F2)
GO TO 100
RVNL(I) = CABS(VL(I))
C ADM EVALUATES THE INPUT ELECTRICAL ADMITTANCE
CALL ADM(K,QLBB,QLAB,GRBA,GRAB,ADMI(I))
RADM(I) = REAL(CMPLX(1,0)/ADMI(I))
IADM(I) = AIMAG(CMPLX(1,0)/ADMI(I))
C ZEL IS THE COMPLEX ELECTRICAL IMPEDANCE
ZEL(I) = CMPLX(1,0)/ADMI(I)
ZELR(I) = REAL(ZEL(I))
ZELI(I) = AIMAG(ZEL(I))
C RADPR EVALUATES THE RADIATED ACOUSTIC POWER
CALL RADPR(LY,LZ,ZFMR(I),VL(I),PRR)
PR(I) = 20 *ALOG10(PRR)
C PE IS THE AVERAGE COMPLEX INPUT ELECTRICAL POWER

```

```

      PE = CMPLX(CD*CD*(B-A)*LY*LZ/(2*CON),0.0) +
      1 CMPLX(0,CD*CD*BM*BM*LY*LZ/(K*ROD*COD*2)) +
      2 (GLBB-GLAB-GRBA+GRAA)
      PER(I) = REAL(PE)
      PERECT(I) = AIMAG(PE)
C EFFIC IS THE TRANSDUCTION PROCESS EFFICIENCY
      EFFIC(I) = 20*ALOG10(PRR/PER(I))
C
      GO TO 1
C
C SEN EVALUATES THE PRESSURE RADIATION PATTERN, TRANSMITTING CURRENT AND
C VOLTAGE SENSITIVITIES AND THE ANGLE OF THE MAIN LOBE
C
C IF A DIRECTIVITY PLOT IS DESIRED SET FLAG = 1 0 (DB SCALE)
C AND / OR SET FLAG2 = 1 0 (LINEAR SCALE)
C SET FLAG AND FLAG2 = 0 0 OTHERWISE
C SET THE FLAGS IN THE IF STATEMENTS BELOW, ONLY
      100 FLAG = 0 0
          FLAG2 = 0 0
          IF(I EQ 1) FLAG=1 0
          IF(I EQ 1) FLAG2= 0
C IF THE SENSITIVITY ON THE X AXIS IS DESIRED SET FLAG3 = 0 0
C IF THE MAXIMUM SENSITIVITY IS DESIRED SET FLAG3 = 1 0
C FLAG3 MUST EQUAL 1 0 WHEN DIRECTIVITY PLOTS ARE REQUESTED
C
          FLAG3 = 1 0
C
      CALL SEN(FREQ(I),U1,U2,P1,P2,CXLNLA,CXLNLB,CXRLA,CXRLB
      1,GLBB,GLAB,GRBA,GRAA,TCSL(I),TVSL(I),ANGMAX(I),FLAG,FLAG2,FLAG3)
C
      WRITE(4,*) FREQ(I),FLOG(I),TCSL(I)
      1 CONTINUE
C
C D2PLT PRODUCES A NEUTRAL PLOT FILE FOR PLOTTING ON THE TEKTRONICS
C
      CALL D2PLT(N,FREQ,MRNL,1)
      CALL D2PLT(N,FREQ,RPNL,2)
      CALL D2PLT(N,FLOG,PSPL,3)
      CALL D2PLT(N,FREQ,RVNL,4)
      CALL D2PLT(N,FREQ,IADN,5)
      CALL D2PLT(N,FREQ,RADN,6)
      CALL D2PLT(N,FLOG,PR,7)
      CALL D2PLT(N,FREQ,PER,8)
      CALL D2PLT(N,FREQ,PERECT,9)
      CALL D2PLT(N,FLOG,EFFIC,10)
      CALL D2PLT(N,FLOG,TVSL,11)
      CALL D2PLT(N,FLOG,TCSL,12)
      CALL D2PLT(N,FREQ,ANGMAX,13)
      CALL D2PLT(N,FREQ,ZMR,14)
      CALL D2PLT(N,FREQ,ZMI,15)
      CALL D2PLT(N,FREQ,ZFMR,16)
      CALL D2PLT(N,FREQ,ZFMI,17)
      CALL D2PLT(N,FREQ,RATIO,18)
      STOP
      END
C
C.....
C
      BLOCK DATA
C
C VARIABLE INPUTS TO PROGRAM MHD
C
C A LEFT BOUNDARY OF SOURCE VOLUME (METERS)
C B RIGHT " " " "
C L TOTAL WAVEGUIDE LENGTH (METERS)
C LY TRANSVERSE WAVEGUIDE LENGTH Y-DIR (METERS)
C LZ " " " " Z-DIR "
C SRAD RADIUS OF SPHERICAL BAFFLE (METERS)
C ROD FLUID DENSITY IN WAVE GUIDE (KG/METER**3)
C COD " SOUND SPEED " (METERS/SEC)
C ROM FLUID DENSITY IN FREE MEDIUM (KG/METER**3)
C COM " SOUND SPEED " (METERS/SEC)
C BM MAGNETIC INDUCTION FIELD AMPLITUDE (WEBERS/METER**2)
C CD CURRENT DENSITY AMPLITUDE (AMPERES/METER**2)
C COM ELECTRICAL CONDUCTIVITY OF FLUID IN WAVEGUIDE (1/OHMS METER)
C FO INITIAL CALCULATION FREQUENCY (HERTZ)
C FF FINAL " "
C FD FREQUENCY STEP SIZE (HERTZ)
C
      COMMON /ZIP/A,B,L,LY,LZ,SRAD,ROD,COD,ROM,COM,P1,BM
      1,CD,CON,FO,FF,FD
      REAL L,LY,LZ
      DATA A,B,L,LY,LZ,SRAD,ROD,COD,ROM,COM,P1,BM,CD,CON,FO,FF,FD/
      1-0.05,0.05,10.0,0.318,0.0381,0.5,1041,1536,1600,998,1481
      2,3,14159,0.40,14436,5,28,250,10000,50 /
C
C PHYSICAL PROPERTIES
C
C 6X NACL-H2O SOLUTION ROD = 1041 COD = 1536 1600 (MEASURED)
C
C MERCURY ROD = 13600 COD = 1430
C

```



```

      CALL MHBSJR(X, S,N+3,J1,WK,IER)
      CALL MHBSYN(X, S,N+3,Y1,IER)
      ZRM1 = 0.0
      ZCM1 = 0.0
      ZRS1 = 0.0
      ZCS1 = 0.0
      N2 = N-1
C THE SERIES ARE SUMMED IN THE I LOOP
C TO CALCULATE THE SELF AND MUTUAL IMPEDANCES
      DO 3 I=1,N2
        S1 = FLOAT(I)
        D = (((S1-1)/X)*J1(I)-J1(I+1))*2 +
        1/((S1-1)/X)*Y1(I)-Y1(I+1))*2
        D1 = (((S1-1)/X)*J1(I)+J1(I+1)*Y1(I)+Y1(I+1) -
        1/((S1-1)/X)*J1(I+1)*Y1(I+1))
        D2 = -J1(I)*Y1(I+1)-J1(I+1)*Y1(I)
        RS = D2/D
        CPL = -D1/D
        G2M = (1/(2*(S1-1)+1))*((P(1)-P(1+2))*2)*P1(I)
        G2S = (1/(2*(S1-1)+1))*((P(1)-P(1+2))*2)
        ZRM1 = G2M*RS+ZRM1
        ZCM1 = G2M*CPL+ZCM1
        ZRS1 = G2S*RS+ZRS1
        ZCS1 = G2S*CPL+ZCS1
      3 CONTINUE
C RESULT
      RM = G*ZRM1
      CIM = G*ZCM1
      R = G*ZRS1
      CX = G*ZCS1
      RETURN
      END
C
C.....
C
      SUBROUTINE GREEN(X,A,B,L,RNL,RL,GLNLA,GLNLB,GRLA,GRLB,
      1,GXLNLA,GXLNLB,GXRLA,GXRLB,GLBB,GLAB,GRAA,GRBA)
C
C GREEN EVALUATES THE PLANE WAVE GREEN'S FUNCTION FOR THE WAVE FIELD IN
C THE WAVEGUIDE AT VARIOUS LOCATIONS
C
      COMPLEX CC,KA,KB,KL2,RNL,RL,GLNLA,GLNLB,GRLA,GRLB,GLBB,GLAB
      1,GRAA,GRBA,LA,LB,HA,HB
      2,GXLNLA,GXLNLB,GXRLA,GXRLB
      REAL X,L
      KA = CMPLX(0,K*A)
      KB = CMPLX(0,K*B)
      KL2 = CMPLX(0,K*L/2)
      CC = CMPLX(0,1)/(CMPLX(2*K,0)*(CMPLX(1,0)-RNL*RL))
      LA = CC*(CEXP(KA)+RL*CEXP(-KA))
      RA = CC*(CEXP(-KA)+RNL*CEXP(KA))
      LB = CC*(CEXP(KB)+RL*CEXP(-KB))
      RB = CC*(CEXP(-KB)+RNL*CEXP(KB))
C THE GREEN'S FUNCTIONS
      GLAB = LB*(CEXP(-KA)+RNL*CEXP(KA))
      GRAA = RA*(CEXP(KA)+RL*CEXP(-KA))
      GLBB = LB*(CEXP(-KB)+RNL*CEXP(KB))
      GRBA = RA*(CEXP(KB)+RL*CEXP(-KB))
      GLNLA = LA*(CEXP(KL2)+RNL*CEXP(-KL2))
      GLNLB = LB*(CEXP(KL2)+RNL*CEXP(-KL2))
      GRLA = RA*(CEXP(KL2)+RL*CEXP(-KL2))
      GRLB = RB*(CEXP(KL2)+RL*CEXP(-KL2))
C DERIVATIVES OF THE GREEN'S FUNCTIONS (WRT X)
      GXLNLA = CMPLX(0,0,-K)*LA*(CEXP(KL2)-RNL*CEXP(-KL2))
      GXLNLB = CMPLX(0,0,-K)*LB*(CEXP(KL2)-RNL*CEXP(-KL2))
      GXRLA = CMPLX(0,0,K)*RA*(CEXP(KL2)-RL*CEXP(-KL2))
      GXRLB = CMPLX(0,0,K)*RB*(CEXP(KL2)-RL*CEXP(-KL2))
      RETURN
      END
C
C.....
C
      SUBROUTINE PRES(GLNLA,GLNLB,GRLA,GRLB,PNL,PL)
C
C PRES EVALUATES THE APERTURE PRESURE
C PNL IS THE COMPLEX PRESSURE AT THE LEFT APERTURE
C PL " " " " " " RIGHT "
C
      COMMON /ZIP/ A,B,L,LV,LZ,SRAD,ROD,COD,ROM,COM,P1,BM,CD
      1,CON,FO,FF,FD
      COMPLEX PNL,PL,GLNLA,GLNLB,GRLA,GRLB
      PNL = CMPLX(BM*CD,0)*(GLNLA-GLNLB)
      PL = CMPLX(BM*CD,0)*(GRLA-GRLB)
      RETURN
      END
C
C.....
C
      SUBROUTINE VEL(K,GXLNLA,GXLNLB,GXRLA,GXRLB,VNL,VL,U1,U2,P1,P2)
C

```

```

C VEL EVALUATES THE PARTICLE VELOCITY AT THE APERTURE
C VNL IS THE COMPLEX PARTICLE VELOCITY AT THE LEFT APERTURE
C VL = " " " " " " " " " "
C
COMMON /ZIP/ A,B,L,LY,LZ,SRAD,ROD,COD,ROM,COM,P1,BH,CD,CON,FO,FF,FD
COMPLEX VL,VNL,GXNLMA,GXNLMB,GXRLA,GXRLB
REAL K
VNL = CMPLX(0.0,-BH*CD/(K*ROD+COD))*((GXNLMA - GXNLMB)
VL = CMPLX(0.0,-BH*CD/(K*ROD+COD))*((GXRLA - GXRLB)
U1 = CABS(VL)
U2 = CABS(VNL)
U11 = REAL(VL)
U22 = -REAL(VNL)
C THE CONDITIONALS BELOW EVALUATE THE RELATIVE PHASES OF THE APERTURE
C PARTICLE VELOCITIES REFERENCED TO THE SURFACE OF THE SPHERICAL BAFFLE
IF(U11 GE 0.0 AND U22 LT 0.0) THEN
P1 = 3.141592654
P2 = 0.0
ELSEIF(U11 GE 0.0 AND U22 GE 0.0) THEN
P1 = 0.0
P2 = 0.0
ELSEIF(U11 LT 0.0 AND U22 LT 0.0) THEN
P1 = 3.141592654
P2 = 3.141592654
ELSE
P1 = 3.141592654
P2 = 0.0
ENDIF
RETURN
END

C
C.....
C
SUBROUTINE ADM(K, GLBB, GLAB, GRBA, GRAA, ADM1)
C
C ADM EVALUATES THE ELECTRICAL INPUT ADMITTANCE OF THE TRANSDUCER
C ADM1 IS THE COMPLEX INPUT ADMITTANCE (OHMS)
C
COMMON /ZIP/ A,B,L,LY,LZ,SRAD,ROD,COD,ROM,COM,P1,BH,CD,CON,FO,FF,FD
COMPLEX ADM1, GLBB, GLAB, GRBA, GRAA
REAL L,LY,LZ,K
ADM1 = CMPLX(LZ*CON*(B-A)/LY,0.0) +
1 CMPLX(0.0,-BH*BH*LZ*CON*CON/(K+COD*ROD*LY))*((GLBB-GLAB-GRBA+GRAA)
RETURN
END

C
C.....
C
SUBROUTINE RADPR(LY,LZ,ZR,VL,PR)
C
C RADPR EVALUATES THE RADIATED ACOUSTIC POWER AT THE APERTURES
C
COMPLEX VL
REAL LY,LZ,PR
PR = (CABS(VL)**2)*ZR*LY*LZ
RETURN
END

C
C.....
C
SUBROUTINE SEN(FREQ,U1,U2,MU1,MU2,GXNLMA,GXNLMB,GXRLA,GXRLB)
C
C SEN EVALUATES 1)THE FARFIELD PRESSURE DIRECTIVITY, GIVEN THE AMPLITUDES
C OF THE APERTURE PARTICLE VELOCITIES AND PHASES
C 2)THE TRANSMITTING SENSITIVITIES AT ONE METER PER UNIT AMP AND VOLT
C THE FARFIELD PRESSURE IS CALCULATED USING C H SHERMANS RESULTS
C
1, GLBB, GLAB, GRBA, GRAA, TCSL, TVSL, ANCHAX, FLAG, FLAG2, FLAG3)
COMMON /ZIP/ A,B,L,LY,LZ,SRAD,ROD,COD,ROM,COM,P1,BH,CD,CON
1,FO,FF,FD
DIMENSION LO(105),L1(100,100),L2(100,100),J1(100)
1,Y1(100),WK(410),PS(105)
2,PSL(105),ANG(105)
3,PN(105)
COMPLEX GXNLMA,GXNLMB,GXRLA,GXRLB, GLBB, GLAB, GRBA, GRAA
1,P11(105),DH,C11,C22,C5,SUM1,SUM2,SUM11,SUM22,P1,P2,A1,A2
INTEGER N,ND,I,J
REAL LO,L1,L2,MU1,MU2,KA,KR,L,LY,LZ,J1
C
C N IS THE NUMBER OF TERMS REQUIRED FOR CONVERGENCE OF THE SERIES EXPRESSION
C FOR THE FARFIELD PRESSURE ND IS THE NUMBER OF POINTS CALCULATED ON THE
C DIRECTIVITY CIRCLE R IS THE RADIAL DISTANCE(METERS) IN THE FARFIELD AT WHICH
C PRESSURE CALCULATION IS MADE
DATA N,ND,R/55,73,1 /
NPTS = ND
RD = SQRT(LY*LZ/P1)
T = ATAN(RD/SRAD)
KR = 2 *PI*FREQ/COM*R
KA = 2 *PI*FREQ/COM*SRAD
A1 = CMPLX(0.0,(ROM*COM*U1/R)*SQRT(SRAD*SRAD/(2 *PI*KA)))

```

```

      A2 = CMPLX(0. (RDM*COM*U2/R)*SQRT(SRAD*SRAD/(2.*PI*KA)))
C INITIALIZE THE LEGENDRE POLYNOMIALS
      LO(1) = 0.0
      LO(2) = 1.0
      LO(3) = COS(1)
C CALCULATE THE POLYNOMIALS BY RECURSION
      DO 1 J=4,N*2
        RI = FLOAT(I-3)
        LO(I) = (2.*RI+1)/(RI+1)*LO(3)*LO(I-1)-RI/(RI+1)*LO(I-2)
      1 CONTINUE
C DA IS THE ANGLE STEP SIZE
      DA = 2.*PI/FLOAT(ND-1)
C CALCULATE THE ANGLE DEPENDENT LEGENDRE POLYNOMIALS
      DO 2 J=1,ND+1
        ANGLE = FLOAT(J-1)*DA
        L1(1,J) = 1.0
        L1(2,J) = COS(ANGLE)
        L2(1,J) = 1.0
        L2(2,J) = COS(PI-ANGLE)
        DO 3 K=3,N
          RK = FLOAT(K-2)
          L1(K,J) = (2.*RK+1)/(RK+1)*L1(2,J)*L1(K-1,J)-RK/(RK+1)*L1(K-2,J)
          L2(K,J) = (2.*RK+1)/(RK+1)*L2(2,J)*L2(K-1,J)-RK/(RK+1)*L2(K-2,J)
        3 CONTINUE
        IF(FLAG3 EQ 0.0) GO TO 20
      2 CONTINUE
C HMBJSR AND HMBSYN CALCULATE THE BESSEL FUNCTIONS OF THE FIRST AND SECOND
C KINDS RESPECTIVELY
      20 CALL HMBJSR(KA, 5,N*1,J1,WA,IER)
        CALL HMBSYN(KA, 5,N*1,Y1,IER)
        C11 = CEXP(CMPLX(0.0,-MU1))
        C22 = CEXP(CMPLX(0.0,-MU2))
C CALCULATE THE N DEPENDENT TERMS
      DO 4 I=3,N*2
        C3 = (FLOAT(I)-3)/KA*J1(I-2)-J1(I-1)
        C4 = (FLOAT(I)-3)/KA*Y1(I-2)-Y1(I-1)
        C5 = CEXP(CMPLX(0.0,-PI/2.*FLOAT(I-2)))
        DH = CMPLX(C3,C4)
        P11(I-2) = CMPLX(LO(I-2)-LO(I),0.0)*C5/DH
      4 CONTINUE
C SUM THE N TERMS
      DO 5 J=1,ND
        SUM11 = CMPLX(0.0,0.0)
        SUM22 = CMPLX(0.0,0.0)
        DO 6 I=1,N
          SUM1 = P11(I)*CMPLX(L1(I,J),0.0) + SUM11
          SUM2 = P11(I)*CMPLX(L2(I,J),0.0) + SUM22
          SUM11 = SUM1
          SUM22 = SUM2
        6 CONTINUE
C CALCULATE THE ANGLE
        ANG(J) = (FLOAT(J)-1.0)*DA*180./PI
        P1 = A1*C11*SUM1
        P2 = A2*C22*SUM2
C SUM THE PRESSURE FIELDS OF THE SOURCES COHERENTLY AND FIND
C THE MAGNITUDE
        PS(J) = CABS(P1 + P2)
        PSL(J) = 20.*ALOG10(PS(J)/1.0E-06)
        IF(PSL(J) LE 90.0) PSL(J) = 90.0
        WRITE(4,*)PSL(J)
        IF(FLAG3 EQ 0.0) GO TO 30
      5 CONTINUE
        IF(FLAG EQ 1.0) CALL D2PLT(NPTS,ANG,PSL,19)
C IF(FLAG2 EQ 1.0) CALL D2PLT(NPTS,ANG,PS,20)
C LOCATION OF THE MAIN BEAM AXIS
      30 YMAX1 = PS(1)
        IF(FLAG3 EQ 0.0) GO TO 10
        ANGMAX = 1.0
        DO 7 I=2,NPTS
          YMAX = AMAX1(PS(I),YMAX1)
          IF(YMAX GT YMAX1) THEN
            ANGMAX = ANG(I)
          ELSE
            ENDIF
          YMAX1 = YMAX
        7 CONTINUE
C USE THE FOLLOWING CONDITIONAL ONLY FOR THE SYMMETRIC SOURCE
        IF(ANGMAX GT 90.0) ANGMAX = 180. - ANGMAX
C CALCULATE THE SENSITIVITIES
      10 TCS = YMAX1/(CD*(B-A)*LY*1.414)
        TVS = YMAX1/(CD*L2/COM*1.414)
        TCSL = 20.*ALOG10(TCS)
        TVSL = 20.*ALOG10(TVS)
        RETURN
      END
C
C*****
C
      SUBROUTINE D2PLT(NPTS,XX,YY,FLAG)
C

```

C D2PLT IS THE TWO DIMENSIONAL PLOTTING ROUTINE USING ARLLIB
C

```

      DIMENSION XX(1000),YY(1000)
      INTEGER FLAG,NPTS
      XMIN1 = XX(1)
      XMAX1 = XX(1)
      YMIN1 = YY(1)
      YMAX1 = YY(1)
      DO 100 I=2,NPTS
      XMIN = AMIN1(XX(I),XMIN1)
      XMIN1 = XMIN
      XMAX = AMAX1(XX(I),XMAX1)
      XMAX1 = XMAX
      YMIN = AMIN1(YY(I),YMIN1)
      YMIN1 = YMIN
      YMAX = AMAX1(YY(I),YMAX1)
      YMAX1 = YMAX
100  CONTINUE
      IF(YMAX EQ YMIN) YMIN = 0.0
      DX = (XMAX - XMIN)/FLOAT(NPTS)
      XORG=1.0
      YORG=1.0
      XDEL=(XMAX-XMIN)/20.0
      YDEL=(YMAX-YMIN)/10.0
      AYLEN=3.0
      AXLEN=5.0
      XTITL=AXLEN/2.0
      YTITL=AYLEN/0.5
      DX=(XMAX-XMIN)/AXLEN
      DY=(YMAX-YMIN)/AYLEN
      CALL PLTLFNL("PLOT")
      CALL PLTDIM(11.8,5.1,4)
      CALL PLTORG(YORG,YORG)
      GO TO (1,2,3,4,5,6,7,8,9,10,11,12,13,14,15,16,17,18,
1 19,20) FLAG
1  CALL PLTAXIS(0.0,AYLEN,90,YMIN,YMAX,YDEL
1.13HMAG REFL COEF,13.2,-1,-1)
      GO TO 200
2  CALL PLTAXIS(0.0,AYLEN,90,YMIN,YMAX,YDEL
1.22HAPERATURE PRESSURE(PA),22.2,-1,-1)
      GO TO 200
3  CALL PLTAXIS(0.0,AYLEN,90,YMIN,YMAX,YDEL
1.23HAPER PRES(DB RE 1X10-6PA),23.2,-1,-1)
      GO TO 150
4  CALL PLTAXIS(0.0,AYLEN,90,YMIN,YMAX,YDEL
1.14HAPER PART VEL,14.2,-1,-1)
      GO TO 200
5  CALL PLTAXIS(0.0,AYLEN,90,YMIN,YMAX,YDEL
1.20HIMAG ELECT ADM(MHOS),20.2,-1,-1)
      GO TO 200
6  CALL PLTAXIS(0.0,AXLEN,90,YMIN,YMAX,YDEL
1.20HREAL ELECT ADM(OHMS),20.2,-1,-1)
      GO TO 200
7  CALL PLTAXIS(0.0,AYLEN,90,YMIN,YMAX,YDEL
1.23HACOUS PWR(DB RE 1 WATT),23.2,-1,-1)
      GO TO 150
8  CALL PLTAXIS(0.0,AYLEN,90,YMIN,YMAX,YDEL
1.23HREAL INPUT POWER(WATTS),23.2,-1,-1)
      GO TO 200
9  CALL PLTAXIS(0.0,AYLEN,90,YMIN,YMAX,YDEL
1.27HREACTIVE INPUT POWER(WATTS),27.2,-1,-1)
      GO TO 200
10 CALL PLTAXIS(0.0,AYLEN,90,YMIN,YMAX,YDEL
1.25HPOWER EFFICIENCY(DB RE 1),25.2,-1,-1)
      GO TO 150
11 CALL PLTAXIS(0.0,AYLEN,90,YMIN,YMAX,YDEL
1.24HP/V SEN(DB RE 1 PA,VOLT),24.2,-1,-1)
      GO TO 150
12 CALL PLTAXIS(0.0,AYLEN,90,YMIN,YMAX,YDEL
1.23H/I SEN,DB RE 1 PA/AMP),23.2,-1,-1)
      GO TO 150
13 CALL PLTAXIS(0.0,AYLEN,90,YMIN,YMAX,YDEL
1.18HANG MAX RESP (DEG),18.2,-1,-1)
      GO TO 200
14 CALL PLTAXIS(0.0,AYLEN,90,YMIN,YMAX,YDEL
1.20HREAL MUT IMP (RAYLS) 20.4,-1,-1)
      GO TO 200
15 CALL PLTAXIS(0.0,AYLEN,90,YMIN,YMAX,YDEL
1.20HIMAG MUT IMP (RAYLS),20.4,-1,-1)
      GO TO 200
16 CALL PLTAXIS(0.0,AYLEN,90,YMIN,YMAX,YDEL
1.19HREAL FM IMP (RAYLS),19.4,-1,-1)
      GO TO 200
17 CALL PLTAXIS(0.0,AYLEN,90,YMIN,YMAX,YDEL
1.19HIMAG FM IMP (RAYLS),19.4,-1,-1)
      GO TO 200
18 CALL PLTAXIS(0.0,AYLEN,90,YMIN,YMAX,YDEL
1.21HRATIO MAG(ZM)/MAG(ZS),21.4,-1,-1)
      GO TO 200
19 CALL PLTAXIS(0.0,AYLEN,90,YMIN,YMAX,YDEL

```

```

1, 14HPRES LEVEL(DB), 14, 4, - 1, - 1)
GO TO 250
20 CALL PLTAXIS(0, 0, AYLEN, 90, YMIN, YMAX, YDEL
1, 19HPRES AMPLITUDE (PA), 19, 4, - 1, - 1)
GO TO 250
150 CALL PLTAXIS(0, 0, AXLEN, 0, XMIN, XMAX, XDEL, 11HLOG10(FREQ),
1-11, 4, - 1, - 1)
C150 CALL PLTAXIS(0, 0, AXLEN, 0, XMIN, XMAX, XDEL, 4HRA/R,
C 1-4, 4, - 1, - 1)
GO TO 300
200 CALL PLTAXIS(0, 0, AXLEN, 0, XMIN, XMAX, XDEL, 14HFREQUENCY (HZ),
1-14, 4, - 1, - 1)
GO TO 300
250 CALL PLTAXIS(0, 0, AXLEN, 0, XMIN, XMAX, XDEL
1, 11HANGEL (DEG), -11, 4, - 1, - 1)
GO TO 300
300 CALL PLTAXIS(0, AYLEN, AXLEN, 0, XMIN, XMAX, XDEL, LABX, 0, 0, - 1, - 1)
CALL PLTAXIS(AXLEN, 0, AYLEN, 90, YMIN, YMAX, YDEL, LABY, 0, 0, 1, 1)
CALL PLTDATA(XX, YY, NPTS, 0, 0, XMIN, DX, YMIN, DY, 0, 0)
CALL PLTLINE(XTITL, YTITL, - 1)
CALL PLTEND(11, 0, 8, 5)
RETURN
END
PROGRAM THERMO(INPUT, OUTPUT, DATA, TAPE2=INPUT, TAPE4=DATA
1, PLOT, TAPE5=PLOT)
C
C*****
C
C PROGRAM THERMO PERFORMS A FREQUENCY DOMAIN ANALYSIS OF THE
C THERMOACOUSTIC TRANSMITTING CHARACTERISTICS OF A PLANE WAVE MODE MHD
C TRANSDUCER THERMO COMPUTES THE ACOUSTIC FIELD AS A FUNCTION OF THE
C THE TRANSMITTED ACOUSTIC FREQUENCY, WHICH IS TWICE THE ELECTRICAL DRIVE
C FREQUENCY THE POWER EFFICIENCY AND TRANSMITTING SENSITIVITIES ARE
C COMPUTED AS A FUNCTION OF THE ELECTRICAL DRIVE FREQUENCY
C
C THERMO GENERATES GRAPHIC OUTPUT FOR THE FOLLOWING TRANSDUCER
C CHARACTERISTICS
C
C 1) MAGNITUDE OF THE REFLECTION COEFF (MRNL) VERSUS ACOUSTIC FREQUENCY (AFREQ)
C 2) MAGNITUDE OF APERTURE PRESSURE (RPNL) VERSUS AFREQ
C 3) DB LEVEL OF RPNL VERSUS LOG10(AFREQ)
C 4) " " OF APERTURE PART VEL (RVNL) VERSUS LOG(AFREQ)
C 5) " " OF RADIATED ACOUSTIC POWER (PR) VERSUS LOG(AFREQ)
C 6) " " OF TRANSDUCTION POWER EFFICIENCY (EFFIC) VERSUS
C LOG10(ELECTRICAL SIGNAL FREQUENCY) (FLOG)
C 7) QUADRATIC CURRENT TRANSFER FUNCTION(GCTF) VERSUS LOGFREQ
C 8) DB LEVEL OF QUADRATIC VOLTAGE TRANSMITTING SENSITIVITY(QVTS) VERSUS LOGFREQ
C 9) PRESSURE LEVEL DIRECTIVITY
C 10) ANGLE OF PRIMARY BEAM VERSUS AFREQ
C
C DATA INPUT IS THROUGH THE BLOCK DATA STATEMENT AT THE END OF THE
C MAIN PROGRAM
C
C*****
C
COMMON /ZIP/ A, B, L, LY, LZ, SRAD, ROD, COD, ROM, COM, PI, BETA, CP, CD
1 CON, BM, FO, FF, FD
DIMENSION AFREQ(1000), EFREQ(1000), FLOG(1000), PR(1000)
1, PSPL(1000), RPNL(1000), RVNL(1000), MRNL(1000), FLOGA(1000)
2, TCSL(1000), TVSL(1000), ANGMAX(1000), EFFIC(1000)
3, GTSL(1000), GCTFR(1000), GCTFI(1000)
COMPLEX RNL(1000), RL(1000), PNL(1000), PL(1000)
1, VNL(1000), VL(1000), GCTF(1000)
2, GLNLA, GLNLB, GRLA, GRLB
3, GXLNLA, GXNLB, GXRLA, GXRLB
REAL K, L, LY, LZ, MRNL
INTEGER I, N
N = (FF-FD)/FD + 1

```

```

C
C PRIMARY CALCULATION LOOP
C
  DO 1 I=1,N
C CALCULATE THE WAVE NUMBER AND FREQUENCY
  K = (2 *PI*FD + FLOAT(I-1)*2 *PI*FD)/COD
  AFREQ(I) = K*COD/(2 *PI)
  EFREQ(I) = AFREQ(I)/2
  FLOGA(I) = ALOG10(AFREQ(I))
  FLOG(I) = ALOG10(AFREQ(I)/2)
C REFL EVALUATES THE APERTURE REFLECTION COEFFICIENT
  CALL REFL(K,RNL(I),RL(I),MRNL(I),ZFMR)
C GREEN EVALUATES SEVERAL COMPLEX COEFFICIENTS
  CALL GREEN(K,A,D,L,RNL(I),RL(I),CLNLA,CLNLB,CLRLA,CLRLB
  1,CLNLNA,CLXNLB,CXRLA,CXRLB)
C PRES EVALUATES THE APERTURE PRESSURE IN THE WAVE GUIDE
  CALL PRES(CLNLNA,CLNLB,CLRLA,CLRLB,PNL(I),PL(I))
  RPNL(I) = CABS(PNL(I))
  PSPL(I) = 20 *ALOG10(RPNL(I)/ 000001)
C VEL EVALUATES THE APERTURE PARTICLE VELOCITY
  CALL VEL(K,CLNLNA,CLXNLB,CXRLA,CXRLB,VNL(I),VL(I),U1,U2,P1,P2)
  RVNL(I) = 20 *ALOG10(U2)
C WRITE(4,*)U1 P1 U2,P2
C
C QTF IS THE QUADRATIC CURRENT TRANSFER FUNCTION ROUTINE
  CALL QTF(K,RNL(I),RL(I),QCTF(I))
  QCTFR(I) = REAL(QCTF(I))
  QCTFI(I) = AIMAG(QCTF(I))
C RADPR EVALUATES THE RADIATED ACOUSTIC POWER
  CALL RADPR(LY LZ ZFMR,VL(I),PRR)
  PR(I) = 20 *ALOG10(PRR)
C PE IS THE AVERAGE REAL INPUT ELECTRICAL POWER
  PE = CD*CD*(B-A)*LY*LZ/(2 *CON)
C EFFIC IS THE TRANSDUCTION PROCESS POWER EFFICIENCY
  EFFIC(I) = 20 *ALOG10(PRR/PE)
  IF(EFFIC(I) LE -300 )EFFIC(I) = -300
C
C QVTS EVALUATES THE PRESSURE RADIATION PATTERN, QUADRATIC TRANSMITTING
C VOLTAGE SENSITIVITY AND THE ANGLE OF THE MAIN LOBE
C
C IF A DIRECTIVITY PLOT IS DESIRED SET FLAG = 1 0 (DB SCALE)
C IN IF STATEMENTS BELOW
C AND / OR SET FLAG2 = 1 0 (LINEAR SCALE)
C SET FLAG AND FLAG2 = 0 0 OTHERWISE
C
C GO TO 1
  FLAG = 0 0
  FLAG2 = 0 0
  IF(I EQ 1) FLAG=0 0
  IF(I EQ 1) FLAG2=0 0
C
C IF THE X AXIS SENSITIVITY IS DESIRED SET FLAG3 = 0 0
C IF THE SENSITIVITY ON THE MAIN BEAM AXIS IS DESIRED SET FLAG3 = 1 0
C FLAG3 MUST BE 1 0 WHEN CALCULATING DIRECTIVITY PATTERNS
C
  FLAG3 = 0 0
C
C CALL QVTS(AFREQ(I),ABS(U1),ABS(U2),P1,P2
  1,QTSL(I),ANGMAX(I),FLAG,FLAG2,FLAG3)
  IF(QTSL(I) LE -100 )QTSL(I)=-100
  WRITE(4,*) EFREQ(I),QTSL(I)
1 CONTINUE
C
C D2PLT PRODUCES A NEUTRAL PLOT FILE FOR PLOTTING ON THE TEKTRONICS
C
  GO TO 2
  CALL D2PLT(N,AFREQ,MRNL,1)
  CALL D2PLT(N,AFREQ,RPNL,2)
  CALL D2PLT(N,FLOGA,PSPL,3)
  CALL D2PLT(N,FLOGA,RVNL,4)
  CALL D2PLT(N,FLOGA,PR,5)
  CALL D2PLT(N,FLOG,EFFIC,6)
2 CALL D2PLT(N,FLOG,QTSL,7)
  GO TO 3
  CALL D2PLT(N,EFREQ,QCTFR,8)
  CALL D2PLT(N,EFREQ,QCTFI,12)
  CALL D2PLT(N,AFREQ,ANGMAX,9)
3 STOP
  END
C
C *****
C
  BLOCK DATA
C
C VARIABLE INPUTS TO PROGRAM THE9MD
C
C A LEFT BOUNDARY OF SOURCE VOLUME (METERS)
C B RIGHT
C L TOTAL WAVEGUIDE LENGTH (METERS)
C LY TRANSVERSE WAVEGUIDE LENGTH Y-DIR (METERS)
C LZ 2-DIR

```

```

C SRAD RADIUS OF SPHERICAL DAPPLE (METERS)
C ROD FLUID DENSITY IN WAVE GUIDE (KG/METER**3)
C COD " SOUND SPEED " " (METERS/SEC)
C ROM FLUID DENSITY IN FREE MEDIUM (KG/METER**3)
C COM " SOUND SPEED " " (METERS/SEC)
C CD CURRENT DENSITY AMPLITUDE (AMPERES/METER**2)
C BETA THERMAL COEFFICIENT OF EXPANSION OF FLUID (M**3/M**3/KELVIN)
C CP SPECIFIC HEAT CAPACITY OF FLUID (JOULCS/KG/KELVIN)
C CON ELECTRICAL CONDUCTIVITY OF FLUID IN WAVEGUIDE (1/OHMS METER)
C FO INITIAL CALCULATION FREQUENCY (HERTZ)
C FF FINAL "
C FD FREQUENCY STEP SIZE (HERTZ)
C
COMMON /ZIP/A,B,L,LY,LZ,SRAD,ROD,COD,ROM,COM,PI,BETA,CP,CD
1.COM,BM,FO,FF,FD
REAL L,LY,LZ
DATA A,B,L,LY,LZ,SRAD,ROD,COD,ROM,COM,PI,BETA,CP,CD,CON
1.BM,FO,FF,FD/-0.05,0.05, 10, 0.318, 0.381,0.032,1041,1600,998
2.1481,3,14159,0.00021,3968,14426,.5,28,40
3.500,13000,250 /
C
C PHYSICAL PROPERTIES OF NACL 6% SOLUTION AT 20 C
C
C CON 3.28 (1/OHM/M) MEASURED
C ROD 1041 (KG/M**3)
C COD 1500 (M/SEC)
C CP 3968 (JOULES/KG/KELVIN)
C BETA 2.1E-04 (M**3/M**3/KELVIN)
C
C PHYSICAL PROPERTIES OF MERCURY AT 20 C
C
C CON 1020000 (1/OHM M)
C ROD 13600 (KG/M**3)
C COD 1450 (M/SEC)
C CP 140 (J/KG/K)
C BETA 1.83E-04 (1/K)
C
END
C
C*****
C
SUBROUTINE REFL(K,RSNL,RSL,RSNLM,ZSR)
C
C SUBROUTINE REFL CALCULATES THE COEFFICIENTS AND EVALUATES THE
C QUADRATIC EQUATION FOR THE REFLECTION COEFFICIENTS
C
COMMON /ZIP/A,B,L,LY,LZ,SRAD,ROD,COD,ROM,COM,PI,BETA,CP,CD
1.COM,BM,FO,FF,FD
COMPLEX KA,KB,KL2,ZS,ZM,A1,B1,C1,D1,A2,B2,C2,D2,E2,F2,G2,H2
1.C11,C22,C33,C44,C55,C66,RSNL,RSL,RLNL,RLNL
REAL L,LY,LZ,K,PC
PC = ROD*COD
KA = CMPLX(0.0,K*A)
KB = CMPLX(0.0,K*B)
KL2 = CMPLX(0.0,K*L/2)
C CALCULATE THE APERTURE IMPEDANCES
CALL MISP(K*COD,ZMR,ZMI,ZSR,ZSI)
ZS = CMPLX(ZSR,ZSI)/CMPLX(PC,0.0)
ZM = CMPLX(ZMR,ZMI)/CMPLX(PC,0.0)
C CALCULATE THE QUADRATIC EQUATION COEFFICIENTS
C1 = CEXP(KA) - CEXP(KB)
D1 = CEXP(-KA) - CEXP(-KB)
A1 = CEXP(-KL2)
B1 = CEXP(KL2)
A2 = B1*D1*(CMPLX(1.0,0.0)-ZS)+B1*C1*ZM
B2 = A1*D1*(CMPLX(1.0,0.0)+ZS)-B1*D1*ZM
C2 = D1*C1*(CMPLX(-1.0,0.0)+ZS)-A1*C1*ZM
D2 = -A1*C1*(CMPLX(1.0,0.0)+ZS)+A1*D1*ZM
E2 = B1*C1*(CMPLX(1.0,0.0)-ZS)+B1*D1*ZM
F2 = D1*D1*(CMPLX(-1.0,0.0)+ZS)-A1*D1*ZM
G2 = A1*C1*(CMPLX(1.0,0.0)+ZS)-B1*C1*ZM
H2 = -A1*D1*(CMPLX(1.0,0.0)+ZS)+A1*C1*ZM
C11 = A2*F2 - B2*E2
C22 = A2*H2 - B2*G2 + C2*F2 - D2*E2
C33 = C2*H2 - D2*G2
C44 = C2*E2 - A2*G2
C55 = D2*E2 + C2*F2 - B2*G2 - A2*H2
C66 = D2*F2 - B2*H2
C CALCULATE THE COMPLEX ROOTS USING THE FOLLOWING IMSL ROUTINES
C THE ROOT WITH THE MAGNITUDE LESS THAN ONE IS PHYSICALLY
C MEANINGFUL THE OTHER IS DISCARDED
CALL ZGADC(C33,C22,C11,RSNL,RLNL,IER)
CALL ZGADC(C66,C55,C44,RSL,RLNL,IER)
RSNLM = CABS(RSNL)
RETURN
END
C
C*****
C
SUBROUTINE MISP(W,RM,CXM,R,CX)

```

```

C
C MISP EVALUATES THE SELF AND MUTUAL ACOUSTIC IMPEDANCES AT THE
C WAVEGUIDE APERTURES. THE RESULTS ARE INPUT TO REFL TO EVALUATE THE
C REFLECTION COEFFICIENTS
C MISP USES THE EQUATIONS DEVELOPED BY C H SHERMAN TO EVALUATE THE MUTUAL
C AND SELF IMPEDANCES OF TWO CIRCULAR SOURCES 180 DEGREES APART ON THE
C SURFACE OF A SPHERICAL BAFFLE
C
      DIMENSION P(1000), WK(2000), J1(1000), Y1(1000),
      IP1(1000)
      COMMON/ZIP/A,B,L,LY,LZ,SRAD,ROD,CDD,ROM,COM,PI,BETA,CP,CD
      I,CON,BM,FO,FF,FD
      REAL J1,Y1,L,LY,LZ
      INTEGER I,M,N
C N IS THE NUMBER OF TERMS IN THE SUM REQUIRED FOR CONVERGENCE AT
C LARGE VALUES OF K*RD
      N = 50
C RD IS THE EFFECTIVE RADIUS OF THE CROSS SECTION OF A RECTANGULAR
C WAVEGUIDE
      RD = SQRT(LY*(LZ/PI))
      T = ATAN(RD/SRAD)
      G = ROM*COM*SRAD*SRAD/(RD*RD)
C INITIALIZATION OF LEGENDRE POLYNOMIALS
      P(1) = 1.0
      P(2) = 1.0
      P(3) = COS(T)
      P1(1) = 1.0
      P1(2) = -1.0
      M = N+2
C CALCULATION OF LEGENDRE POLYNOMIALS BY RECURSION
      DO 1 K=3,M
      RI = FLOAT(K)
      R2 = RI - 1.0
      P(K+1) = P(3)*P(K)*(2.0*RI+1.0)/(RI+1.0)-P(K-1)*RI/(RI+1.0)
      P1(K) = P1(2)*P1(K-1)*(2.0*R2+1.0)/(R2+1.0)-P1(K-2)*R2/(R2+1.0)
      1 CONTINUE
C THE BESSEL FUNCTION EVALUATIONS ARE PERFORMED BY
C MMBSJR AND MMBSYN (IMSL ROUTINES)
      X = W*SRAD/COM
      CALL MMBSJR(X, 5,N+3,J1,WK,IER)
      CALL MMBSYN(X, 5,N+3,Y1,IER)
      ZRM1 = 0.0
      ZCM1 = 0.0
      ZRS1 = 0.0
      ZCS1 = 0.0
      N2 = N+1
C THE SERIES ARE SUMMED IN THE I LOOP
C TO CALCULATE THE SELF AND MUTUAL IMPEDANCES
      DO 3 I=1,N2
      S1 = FLOAT(I)
      D = ((S1-1.0)/X)*J1(I)-J1(I+1))*2.0 +
      1(((S1-1.0)/X)*Y1(I)-Y1(I+1))*2.0
      D1 = ((S1-1.0)/X)*(J1(I)*J1(I+1)+Y1(I)*Y1(I+1)) -
      1(J1(I)*J1(I+1)+Y1(I)*Y1(I+1))
      D2 = -J1(I)*Y1(I+1)+J1(I+1)*Y1(I)
      RS = D2/D
      CPL = -D1/D
      G2M = (1.0/(2.0*(S1-1.0)+1.0))*((P(I)-P(I+2))*2.0)*P1(I)
      G2S = (1.0/(2.0*(S1-1.0)+1.0))*((P(I)-P(I+2))*2.0)
      ZRM1 = G2M*RS+ZRM1
      ZCM1 = G2M*CPL+ZCM1
      ZRS1 = G2S*RS+ZRS1
      ZCS1 = G2S*CPL+ZCS1
      3 CONTINUE
C RESULT
      RM = G+ZRM1
      CM = G+ZCM1
      R = G+ZRS1
      CX = G+ZCS1
      RETURN
      END
C
C.....
C
      SUBROUTINE GREEN(K,A,B,L,RNL,RL,QLNLA,QLNLD,GRLA,GRLB
      1,QLNLA,QLNLB,GXRLA,GXRLB)
      COMPLEX CC,KA,KB,KL2,RNL,RL,QLNLA,QLNLB,GRLA,GRLB
      1 LA,LB,RA,RB
      2 QXLNLA,QXLNLB,GXRLA,GXRLB
      REAL K,L
      KA = CMPLX(0.0,K*A)
      KB = CMPLX(0.0,K*B)
      KL2 = CMPLX(0.0,K*(L/2.0))
      CC = CMPLX(1.0,0.0)/(CMPLX(2.0*K,0.0)*(CMPLX(1.0,0.0)-RNL*RL))
      LA = CC*(CEXP(KA)-RL*CEXP(-KA))
      RA = CC*(CEXP(-KA)-RNL*CEXP(KA))
      LB = CC*(CEXP(KB)-RL*CEXP(-KB))
      RB = CC*(CEXP(-KB)-RNL*CEXP(KB))
      QLNLA = CMPLX(0.0,-1.0)*LA*(CEXP(KL2)+RNL*CEXP(-KL2))
      QLNLD = CMPLX(0.0,-1.0)*LB*(CEXP(KL2)+RNL*CEXP(-KL2))

```



```

C .....
C
C SUBROUTINE QVTS(FREQ,U1,U2,MU1,MU2,TVSL,ANGMAX,FLAG,FLAG2,FLAG3)
C
C QVTS EVALUATES 1)THE FARFIELD PRESSURE DIRECTIVITY, GIVEN THE AMPLITUDES
C OF THE APERTURE PARTICLE VELOCITIES AND PHASES
C 2)THE TRANSMITTING SENSITIVITIES AT ONE METER PER UNIT AMP AND VOLT
C THE FARFIELD PRESSURE IS CALCULATED USING C H SHERMANS RESULTS
C
C COMMON /ZIP/ A,B,L,LY,LZ,SRAD,ROD,COD,ROM,COM,P1,BETA,CP,CD
1.COM,BM,FO,FF,FD
DIMENSION LO(105),L1(100,100),L2(100,100),J1(100)
1.Y1(100),WK(410),PS(105)
2.PSL(105),ANG(105)
3.PN(105)
COMPLEX P11(105),C11,C22,DH,C5,SUM1,SUM2,SUM11,SUM22,P1,P2,A1,A2
INTEGER N,ND,I,J
REAL LO,L1,L2,MU1,MU2,KA,KR,L,LY,LZ,J1
C
C N IS THE NUMBER OF TERMS REQUIRED FOR CONVERGENCE OF THE SERIES EXPRESSION
C FOR THE FARFIELD PRESSURE ND IS THE NUMBER OF POINTS CALCULATED ON THE
C DIRECTIVITY CIRCLE R IS THE RADIAL DISTANCE (METERS) IN THE FARFIELD AT WHICH
C PRESSURE CALCULATION IS MADE
C
DATA N,ND,R/55,73,1 /
NPTS = ND
RD = SQRT(LY*LZ/P1)
T = ATAN(RD/SRAD)
KR = 2 *PI*FREQ/COM*R
KA = 2 *PI*FREQ/COM*SRAD
A1 = CMPLX(0.0,(ROM*COM*U1/R)*SQRT(SRAD*SRAD/(2 *PI*KA)))
A2 = CMPLX(0.0,(ROM*COM*U2/R)*SQRT(SRAD*SRAD/(2 *PI*KA)))
C INITIALIZE THE LEGENDRE POLYNOMIALS
LO(1) = 0.0
LO(2) = 1.0
LO(3) = COS(T)
C CALCULATE THE POLYNOMIALS BY RECURSION
DO 1 I=4,N+2
RI = FLOAT(I-3)
LO(I) = (2 *RI+1)/(RI+1)*LO(3)+LO(I-1)-RI/(RI+1)*LO(I-2)
1 CONTINUE
C DA IS THE ANGLE STEP SIZE
DA = 2 *PI/FLOAT(ND+1)
C CALCULATE THE ANGLE DEPENDENT LEGENDRE POLYNOMIALS
DO 2 J=1,ND+1
ANGLE = FLOAT(J-1)*DA
C
L1(1,J) = 1.0
L1(2,J) = COS(ANGLE)
L2(1,J) = 1.0
L2(2,J) = COS(PI-ANGLE)
DO 3 K=3,N
RK = FLOAT(K-2)
L1(K,J) = (2 *RK+1)/(RK+1)*L1(2,J)+L1(K-1,J)-RK/(RK+1)*L1(K-2,J)
L2(K,J) = (2 *RK+1)/(RK+1)*L2(2,J)+L2(K-1,J)-RK/(RK+1)*L2(K-2,J)
3 CONTINUE
IF(FLAG3 EQ 0.0) GO TO 20
2 CONTINUE
C MMBSJR AND MMBSYN CALCULATE THE BESSEL FUNCTIONS OF THE FIRST AND SECOND
C KINDS RESPECTIVELY
20 CALL MMBSJR(KA,5,N+1,J1,WK,IER)
CALL MMBSYN(KA,5,N+1,Y1,IER)
C11 = CEXP(CMPLX(0.0,-MU1))
C22 = CEXP(CMPLX(0.0,-MU2))
C CALCULATE THE N DEPENDENT TERMS
DO 4 I=3,N+2
C3 = (FLOAT(I)-3)/(KA*J1(I-2)-J1(I-1))
C4 = (FLOAT(I)-3)/(KA*Y1(I-2)-Y1(I-1))
DH = CMPLX(C3,C4)
C5 = CEXP(CMPLX(0.0,-PI/2 *FLOAT(I-2)))
P11(I-2) = CMPLX((LO(I-2)-LO(I)),0.0)*C5/DH
4 CONTINUE
C SUMMATION LOOPS
DO 5 J=1,ND
SUM11 = CMPLX(0.0,0.0)
SUM22 = CMPLX(0.0,0.0)
DO 6 I=1,N
SUM1 = P11(I)*CMPLX(L1(I,J),0.0) + SUM11
SUM2 = P11(I)*CMPLX(L2(I,J),0.0) + SUM22
SUM11 = SUM1
SUM22 = SUM2
6 CONTINUE
C CALCULATE THE FARFIELD ANGLE
ANG(J) = (FLOAT(J)-1.0)*DA*180/PI
P1 = A1*SUM1+C11
P2 = A2*SUM2+C22
C SUM THE PRESSURE FIELDS OF THE SOURCES COHERENTLY TO FIND
C THE MAGNITUDE
PS(J) = CABS(P1 + P2)

```

```

      PSL(J) = 20 *ALOG10(PS(J)/1 0E-06)
C      WRITE(4,*) ANG(J) PSL(J)
      IF(FLAG3 EQ 0 0) GO TO 30
3     CONTINUE
      IF(FLAG EQ 1 0) CALL D2PLT(NPTS,ANG,PSL,10)
C      IF(FLAG2 EQ 1 0) CALL D2PLT(NPTS+1,ANG,PS,11)
C LOCATE OF THE MAIN BEAM AXIS
30    YMAX1 = PS(1)
      IF(FLAG3 EQ 0 0) GO TO 10
      ANGMAX = 0 0
      DO 7 1=2,NPTS
        YMAX = AMAX1(PS(1),YMAX1)
        IF(YMAX GT YMAX1) ANGMAX = ANG(1)
        YMAX1 = YMAX
7     CONTINUE
C CALCULATE THE SENSITIVITIES
10    TVS = YMAX1/(CD*CD*LY*LY/(CON*CON))
      TVSL = 20 *ALOG10(TVS)
      RETURN
      END
C
C*****
C
      SUBROUTINE D2PLT(NPTS,XX,YY,FLAGB)
C D2PLT IS THE TWO DIMENSIONAL PLOTTING ROUTINE USING ARLLIB
C
      DIMENSION XX(1000),YY(1000)
      INTEGER FLAGB,NPTS
      XMIN1 = XX(1)
      XMAX1 = XX(1)
      YMIN1 = YY(1)
      YMAX1 = YY(1)
      DO 100 1=2,NPTS
        XMIN = AMIN1(XX(1),XMIN1)
        XMIN1 = XMIN
        XMAX = AMAX1(XX(1),XMAX1)
        XMAX1 = XMAX
        YMIN = AMIN1(YY(1),YMIN1)
        YMIN1 = YMIN
        YMAX = AMAX1(YY(1),YMAX1)
        YMAX1 = YMAX
100   CONTINUE
      IF(YMAX EQ YMIN) YMIN = 0 0
      DX = (XMAX - XMIN)/FLOAT(NPTS)
      XORG=1 0
      YORG=1 0
      XDEL=(XMAX-XMIN)/20 0
      YDEL=(YMAX-YMIN)/10 0
      AXLEN=3 0
      AYLEN=5 0
      XTITL=AXLEN/2 0
      YTITL=AYLEN/0 5
      DX=(XMAX-XMIN)/AXLEN
      DY=(YMAX-YMIN)/AYLEN
      CALL PLTLFN('L'PLOT')
      CALL PLTDIM(11,5,3,1,4)
      CALL PLTORG(XORG,YORG)
      GO TO (1,2,3,4,5,6,7,8,9,10,11,12) FLAGB
1     CALL PLTAXIS(0,0,AYLEN,90,YMIN,YMAX,YDEL
1,13HMAG REFL COEF,13,2,-1,-1)
      GO TO 200
2     CALL PLTAXIS(0,0,AYLEN,90,YMIN,YMAX,YDEL
1,22HAPERATURE PRESSURE(IPA),22,2,-1,-1)
      GO TO 200
3     CALL PLTAXIS(0,0,AYLEN,90,YMIN,YMAX,YDEL
1,25HAPER PRES(DB RE 1X10-6PA),25,2,-1,-1)
      GO TO 175
4     CALL PLTAXIS(0,0,AYLEN,90,YMIN,YMAX,YDEL
1,26HAPER PART VEL(DB RE 1 M/S),26,2,-1,-1)
      GO TO 175
5     CALL PLTAXIS(0,0,AYLEN,90,YMIN,YMAX,YDEL
1,23HACOUS PWF(DB RE 1 WATT),23,2,-1,-1)
      GO TO 175
6     CALL PLTAXIS(0,0,AYLEN,90,YMIN,YMAX,YDEL
1,25HPOWER EFFICIENCY(DB RE 1),25,2,-1,-1)
      GO TO 175
7     CALL PLTAXIS(0,0,AYLEN,90,YMIN,YMAX,YDEL
1,28HQVTS (DB RE 1PA/(VOLT*VOLT)),28,2,-1,-1)
      GO TO 175
8     CALL PLTAXIS(0,0,AYLEN,90,YMIN,YMAX,YDEL
1,24HOCFTR (AMPS (VOLT*VOLT)),24,2,-1,-1)
      GO TO 150
9     CALL PLTAXIS(0,0,AYLEN,90,YMIN,YMAX,YDEL
1,18HANG MAX RESP (DEG),18,2,-1,-1)
      GO TO 200
10    CALL PLTAXIS(0,0,AYLEN,90,YMIN,YMAX,YDEL
1,14HPRES LEVEL(DB),14,4,-1,-1)
      GO TO 250
11    CALL PLTAXIS(0,0,AYLEN,90,YMIN,YMAX,YDEL

```

```

1.19HPRES AMPLITUDE (PA),19,4,- 1,- 1)
GO TO 250
12 CALL PLTAXIS(0,0,AYLEN,90,YMIN,YMAX,YDEL
1.24HQCIFI (AMPS/(VOLT*VOLT)),24,4,- 1,- 1)
150 CALL PLTAXIS(0,0,AXLEN,0,XMIN,XMAX,XDEL,10HINPUT FREQ,
1-10,4,- 1,- 1)
GO TO 300
175 CALL PLTAXIS(0,0,AXLEN,0,XMIN,XMAX,XDEL,14HLOG INPUT FREQ,
1-14,4,- 1,- 1)
GO TO 300
200 CALL PLTAXIS(0,0,AXLEN,0,XMIN,XMAX,XDEL,17HACOUSTIC FREQ(HZ),
1-17,4,- 1,- 1)
GO TO 300
250 CALL PLTAXIS(0,0,AXLEN,0,XMIN,XMAX,XDEL
1.11HANGEL (DEG),-11,4,- 1,- 1)
GO TO 300
300 CALL PLTAXIS(0,AYLEN,AXLEN,0,XMIN,XMAX,XDEL,LABX,0,0,- 1,- 1)
CALL PLTAXIS(AXLEN,0,AYLEN,90,YMIN,YMAX,YDEL,LABY,0,0,1,1)
CALL PLTDATA(X,Y,NPTS,0,0,XMIN,DX,YMIN,DY,0,08)
CALL PLTLIN(XTITL,YTITL,- 1)
CALL PLTEND(11 0.8 5)
RETURN
END

```

REFERENCES

1. A. Kolin, "An alternating field induction flow meter of high sensitivity," *Rev. Sci. Instr.* 16, 109-116 (1945).
2. A. J. Campanella, "Generation and detection of acoustic waves by the Hall effect in electrolytes," Ph.D. Dissertation, The Pennsylvania State University, June 1955.
3. H. Adjisaka and E. L. Hixson, "Liquid state electromagnetic transducer," Acoustic Research Laboratory, Technical Report No.172, Department of Electrical Engineering, The University of Texas at Austin, June 1975.
4. H. Adjisaka and E. L. Hixson, "Transduction principles of a liquid state electromagnetic transducer," *J. Acoust. Soc. Am.* 77, 1933-1938 (1987).
5. I. N. Didenkulov, "Sound generation by an electric current in a fluid," *Acoustic Letters* 6, 168 (1983).
6. P. M. Morse and K. U. Ingard, Theoretical Acoustics (McGraw-Hill, Inc., New York, 1968), p. 323.
7. P. J. Westervelt and R. S. Larson, "Laser excited broadside array," *J. Acoust. Soc. Am.* 54, 121-122 (1973).
8. J. D. Jackson, Classical Electrodynamics, 2nd. ed. (John Wiley and Sons, Inc., New York, 1975).
9. P. M. Morse and K. U. Ingard, Eq. (6.2.11), p. 24.
10. D. T. Blackstock, Notes for Graduate Acoustics II, I.A.2 (The University of Texas at Austin, spring 1984).
11. D. T. Blackstock, Notes for Graduate Acoustics I, I.C.44 (The University of Texas at Austin, fall 1984).
12. A. D. Pierce, Acoustics (McGraw-Hill, Inc., New York, 1981), p. 170.
13. C. H. Sherman, "Mutual radiation impedance of sources on a sphere," *J. Acoust. Soc. Am.* 31, 947-952 (1959).
14. C. H. Sherman, "Mutual radiation impedance between pistons on spheres and cylinders," URL Report No. 405, U. S. Navy Underwater Sound Laboratory, Fort Trumbull, New London, Connecticut (1958).
15. P. Debye and E. Huckel, *Physik. Z.* 24 (1933) (in German).
16. P. Debye and H. Falkenhagen, *Physik. Z.* 29 121 (1928) (in German).

17. K. J. Vetter, Electrochemical Kinetics (Academic Press, New York, 1967), translated from Electrochemische Kinetik (Springer-Verlag, Berlin, 1961), p. 73.
18. D. L. Chapman, Phil. Mag. 25, 475 (1913).
19. K. J. Vetter, Eq. (1.117), p. 75.
20. K. J. Vetter, p. 79.
21. R. E. Dickerson, H. B. Gray, and G. P. Haight, Chemical Principles, 2nd ed. (W. A. Benjamin, Inc., Menlo Park, California, 1974).
22. K. J. Vetter, Eq. (1.117), p. 75.
23. K. J. Vetter, p. 79.
24. Y. C. Kim and E. J. Powers, Digital Time Series Analysis (Electronics Research Center, The University of Texas at Austin, 1980), Ch. 7.
25. J. E. Cousins and W. F. Nash, "Some aspects of the design of large permanent magnets," Brit. J. App. Phys. 10, 471 (1959).
26. A. B. Coppens, "Simple equations for the speed of sound in Neptunian waters," J. Acoust. Soc. Am. 69, 862 (1981).
27. R. E. Francois and G. R. Garrison, "Sound absorption," J. Acoust. Soc. Am. 72, 1886 (1982).
28. L. E. Kinsler et al., Fundamentals of Acoustics, 3rd. ed. (John Wiley and Sons, Inc., New York, 1982), p. 208.
29. D. T. Blackstock, Notes for Graduate Acoustics I, Ch. 9.
30. L. E. Kinsler, p. 502.
31. C. H. Sherman, URL Repo 1 No. 405.

1 December 1986

DISTRIBUTION LIST FOR
ARL-TR-86-30
UNDER CONTRACT N00014-80-C-0490

Copy No.

1	Office of Naval Research 495 Summer Street Boston, MA 02210 Attn: R. L. Sternberg
2	Chief of Naval Research Department of the Navy Arlington, VA 22217 Attn: M. McKisic (Code 425-OA)
3	R. Obrochta (Code 425-AR)
4	F. E. Saalfeld (Code 400)
5	L. Peebles
6	Director Naval Research Laboratory Department of the Navy Washington, D.C. 20375 Attn: O. Diachok (Code 5128)
7	R. Dicus (Code 5128)
8	R. Gragg
9	S. Hanish (Code 5104)
10	B. Hurdle (Code 5101)
11	E. Williams (Code 5133)
12	Officer in Charge Naval Surface Weapons Center White Oak Laboratory Silver Spring, MD 20910 Attn: W. Madigosky

Distribution List for ARL-TR-86-30 under Contract N00014-80-C-0490
(cont'd)

Copy No.

13	Division Superintendent Naval Research Laboratory Underwater Sound Reference Detachment P.O. Box 8337 Orlando, FL 32856
	David W. Taylor Naval Ship Research and Development Center Bethesda, MD 20084
14	Attn: L. J. Maga
15	J. Niemic
16	W. T. Reader
	Naval Postgraduate School Monterey, CA 93940
17	Attn: S. L. Garrett
18	P. H. Moos
	U. S. Department of Commerce National Bureau of Standards Division 737 Building B106-Sound Washington, D.C. 20234
19	Attn: D. R. Flynn
	Acculab 3201 Ridgewood Drive Columbus, OH 43220
20	Attn: A. J. Campanella
	Department of Computer Science and Control Engineering Nagasaki Institute of Applied Science 536 Aba Nagasaki 851-01 JAPAN
21	Attn: H. Ajisaka

Distribution List for ARL-TR-86-30 under Contract N00014-80-C-0490
(cont'd)

Copy No.

	Department of Mechanical Engineering Georgia Institute of Technology Atlanta, GA 30332
22	Attn: Y. H. Berthelot
23	A. Pierce
24	P. H. Rogers
	Department of Physics University of Mississippi University, MS 38677
25	Attn: H. E. Bass
	Applied Research Laboratory The Pennsylvania State University University Park, PA 16802
26	Attn: J. Maynard
	Institute of Sound and Vibration Research The University of Southampton S09 5NH UNITED KINGDOM
27	Attn: C. L. Morfey
	Department of Mechanical Engineering Yale University P. O. Box 2159 Yale Station Campus Address: Mason Laboratory 9 Hillhouse Avenue New Haven, CT 06520-2159
28	Attn: R. E. Apfel

Distribution List for ARL-TR-86-30 under Contract N00014-80-C-049C
(cont'd)

Copy No.

Department of Mechanical Engineering
The University of Texas at Austin
Austin, TX 78712

29	Attn: J. Beaman
30	I. Busch-Vishniac
31	C. Darvennes
32	M. Hamilton
33	T. Hart
34	Yang-Sub Lee
35	H. Paynter
36	A. Traver

Department of Electrical Engineering
The University of Texas at Austin
Austin, TX 78712

37	Attn: E. Hixson
38	H. Woodson

39	David T. Blackstock, ARL:UT
40	Rao Chandrasekhar, ARL:UT
41	Nicholas P. Chotiros, ARL:UT
42	Frederick D. Cotaras, ARL:UT
43	C. Robert Culbertson, ARL:UT
44	James E. Estes, ARL:UT
45	Luis J. Gonzalez, ARL:UT
46	Thomas A. Griffy, ARL:UT
47	James A. Hawkins Jr., ARL:UT

Distribution List for ARL-TR-86-30 under Contract N00014-80-C-0490
(cont'd)

Copy No.

48	Terry L. Henderson, ARL:UT
49	John M. Huckabay, ARL:UT
50	Andrew J. Kimbrough, ARL:UT
51	Steven J. Linde, ARL:UT
52	John W. Maxwell, ARL:UT
53	James A. TenCate, ARL:UT
54	Library, ARL:UT
55 - 61	Reserve, ARL:UT